Polymeric micelles for multi-drug delivery and optical imaging in surgical oncology

By

Hyunah Cho

A dissertation submitted in partial fulfillment of

the requirements for the degree of

Doctor of Philosophy

(Pharmaceutical Sciences)

at the University of Wisconsin-Madison

2013

Date of final oral examination: 12/4/2013
The dissertation is approved by the following members of the Final Oral Committee:

Glen S. Kwon, Professor, Pharmaceutical Sciences, UW-Madison
Clifford S. Cho, Associate Professor, Surgical Oncology, UW-Madison
Melgardt M. De Villiers, Professor, Pharmaceutical Sciences, UW-Madison
Guilherme L. Indig, Associate Professor, Chemistry and Biochemistry, UW-Milwaukee
Sandro Mecozzi, Associate Professor, Pharmaceutical Sciences and Chemistry, UW-Madison
Jamey P. Weichert, Associate Professor, Pharmaceutical Sciences and Radiology, UW-Madison

Polymeric micelles for multi-drug delivery and

optical imaging in surgical oncology

Hyunah Cho

under the supervision of Professor Glen S. Kwon

at the University of Wisconsin-Madison

Abstract

To date, surgery is the most effective cancer treatment. However, traditional surgery under visual observation and by palpation limits detection of small metastatic tumor nodules. Optical near-infrared (NIR) fluorescence imaging has the clinical potential to improve cancer surgery by providing real-time guidance in the operation room. This technology would allow surgeons to conduct traditional white-light surgery with the intention of maximal macroscopic tumor resection and then reinvestigate suspicious regions and microscopic tumor nodules using intraoperative NIR fluorescence imaging.

Polymeric micelles are a promising class of nanocarriers for delivering NIR fluorescence imaging agents to tumors and providing real-time surgical guidance by the enhanced permeability and retention (EPR), tumor priming, and active targeting effects.

Poly(ethylene glycol)-*block*-poly(ε-caprolactone) (PEG-*b*-PCL) micelles carrying 1,1'-dioctadecyltetramethyl indotricarbocyanine iodide (DiR) passively targeted (by the EPR effect) and delineated LS180 solid colon tumors with a high tumor-to-muscle ratio in fluorescent images.

Solid tumor visualization in LS180 colon cancer-bearing animals was enhanced by the tumor priming effect, which was achieved by a 2-step strategy. (1) A single IV injection of poly(ethylene glycol)-*block*-poly($_{D,L}$-lactic acid) (PEG-*b*-PLA) micelles carrying paclitaxel, 17-

allylamino-17-demethoxygeldanamycin, and rapamycin debulked LS180 solid tumors and induced apoptosis exclusively in tumors (2) Penetration of IV administered PEG-*b*-PCL micelles carrying DiR into the primed LS180 solid tumors was facilitated and resulted in a heightened NIR optical signal for the enhanced tumor delineation.

Lastly, actively targeted apoptosis NIR imaging was obtained by a 2-step strategy in an ES-2-luc metastatic intraperitoneal (IP) ovarian cancer model: (1) A single IP injection of PEG-*b*-PCL micelles carrying paclitaxel, cyclopamine, and gossypol debulked IP metastatic tumors and induced significant apoptosis in tumors. (2) IV injected apoptosis-targeting GFNFRLKAGAKIRFGS-PEG-*b*-PCL micelles carrying DiR actively targeted apoptotic tumors, visualized highly metastatic tumors with improved tumor specificity, and provided intraoperative optical imaging for surgical guidance. Intraoperative optical imaging surprisingly permitted identification of tumor nodules as small as 1 mm, enabled more detailed surgical performance, increased surgical accuracy, and decreased residual tumor tissues left undissected in animals.

These results suggest that the polymeric micelle system may be seamlessly integrated into surgical oncology, enhancing visualization of tumors and providing valuable guidance using intraoperative NIR fluorescence imaging.

Acknowledgements

General

I would like to express my deepest gratitude to my advisor, **Professor Glen S. Kwon**, for the continuous support of my graduate study, his encouragement, enthusiasm, and immerse knowledge. There are not enough words to describe how thankful and grateful I am for having him as my advisor. Without his guidance and persistent help, this dissertation would not have been possible.

I am thankful that I could work with **Professor Adam G. Alani**, **Dr. Howard Chen**, **Dr. Thomas Diezi**, **Dr. Hochul Shin**, **Dr. Tsz Chug Lai**, and **Juliana Palacio,** and I appreciate their guidance and continued friendship. Thank you to present Kwon lab members, especially **Carol Chiang**, **Dr. Amy Kang**, and **Dr. Keishiro Tomoda** for their friendship and support.

A special thank you to **Bonnie Fingerhut** and **Professor Melgardt M. De Villiers** for their sense of humor, motivation, and inspiration as great teachers. I had a valuable and enjoyable teaching experience in Drug Delivery Labs I and II with them.

I thank to **Dr. Mark Sacchetti** and all members of **Zeeh Pharmaceutical Experiment Station** for allowing me to intern for a summer and to experience industrial research. Thank you also to **Gary Girdaukas**, **Ken Niemeyer** and **Joni Mitchell** for all their support.

I owe my gratitude to **Professor Jin-Seok Kim**, a M.S. thesis advisor in South Korea, for his support and motivation.

Lastly, I would like to appreciate to **Dr. Tsz Chung Lai** from the bottom of my heart for his help, encouragement, support, and companionship as a lab mate and a lifelong friend.

Committee members

I would like to thank my thesis committee members for their constructive criticism, helpful advice, and encouragement: **Associate Professor Cliff S. Cho** (Surgical Oncology, UW-Madison), **Professor Melgardt M. De Villiers** (Pharmaceutical Sciences, UW-Madison), **Associate Professor Guilherme L. Indig** (Chemistry and Biochemistry, UW-Milwaukee), **Associate Professor Sandro Mecozzi** (Pharmaceutical Sciences and Chemistry), **Associate Professor Jamey P. Weichert** (Pharmaceutical Sciences and Radiology).

Financial support

I would like to thank **Professor Glen Kwon** and the **NIH** (NCI 1R21-CA161537) for supporting me as a research assistant. Thank you to **Dean Jeanette Roberts** and **the University of Wisconsin-Madison, School of pharmacy** for allowing me to have opportunity to work as a teaching assistant. I would also like to thank the **Oscar Rennebohm Foundation** for the Teaching Assistant Award and honorarium, and **Dr. Leon Lachman** for financial support for my visit to the AAPS Annual Meeting and Exposition 2013 in San Antonio, TX. Thank you to **John-Bruce Green** (Baxter Young Investigators Program, Baxter International Inc.) for the Baxter Young Investigators Award.

This dissertation is dedicated to my parents, ***Hyesook Lee*** *and* ***Younghyun Cho****, whose endless love, encouragement, devotion, and support always help me overcome barriers and follow my dream.*

Table of Contents

List of Tables

Chapter 1.

Chapter 2.

Chapter 4.

Chapter 5.

List of Figures

Chapter 1.

Chapter 2.

Chapter 3.

Chapter 4.

List of Abbreviations

^{1}H NMR	Proton nuclear magnetic resonance
17-AAG	17-Allylamino-17-demethoxygeldanamycin
^{18}F-FDG	^{18}F-fluorodeoxyglucose
5-ALA	5-Aminolevulinic acid
^{99m}Tc	Technetium-99m
ABCs	Amphiphilic block copolymers
ANOVA	Analysis of variance
Asp	Aspartate
ATP	Adenosine triphosphate
Bcl-1	B-cell lymphoma-2
Bcl-xL	B-cell lymphoma-extra large
BLI	Bioluminescence intensity
CA125	Cancer antigen 125
CCD	Charged couple device
$CDCl_3$	Deuterated chloroform
CMC	Critical micelle concentration
CT	Computed tomography
CYP	Cyclopamine
DAPI	4',6-Diamidino-2-phenylindole
DiR	1,1'-Dioctadecyltetramethyl indotricarbocyanine iodide
DLS	Dynamic light scattering

DMSO	Dimethyl sulfoxide
dUTP	Deoxyuridine 5'-triphosphate
EGFR	Epidermal growth factor receptor
EPR	Enhanced permeability and retention
ERK	Extracellular signal-regulated kinase
FITC	Fluorescein isothiocyanate
FLARE™	Fluorescence-assisted resection and exploration™
FLI	Fluorescence intensity
FR	Folate receptor
GSP	Gossypol
HCl	Hydrochloride
HEPES	4-(2-Hydroxyethyl)piperazin-1-ethanesulfonic acid
Hh pathway	Hedgehog pathway
HSA	Human serum albumin
Hsp90	Heat shock protein 90
ICG	Indocyanine green
IO	Intraocular
IFP	Interstitial fluid pressure
IP	Intraperitoneal
IV	Intravenous
LS	Lesion size
mAbs	Monoclonal antibodies

MAPK	Mitogen-activated protein kinase
Mcl-1	Myeloid cell leukemia sequence 1
MDR1	Multidrug resistance protein1
MEM	Minimum essential medium
MMP	Matrix metalloproteinase
M_n	Number average molecular weight
mTOR	Mammalian target of rapamycin
MPS	Mononuclear phagocytic system
MRI	Magnetic resonance imaging
MTD	Maximum tolerated dose
MTT	3-(4,5-Dimethylthiazol-2-yl)-2,5-diphenyltetrazolium bromide
M_w	Weight average molecular weight
MWCO	Molecular weight cut-off
NACT	Neoadjuvant chemotherapy
$NaBH_3CN$	Sodium cyanoborohydride
NaOH	Sodium hydroxide
NIR	Near-infrared
NSCLC	Non-small cell lung cancer
P	P-value
PTX	Paclitaxel
PBS	Phosphate buffer saline
PC	Phosphatidylcholine

PCI	Peritoneal cancer index
PDI	Polydispersity index
PEG	Poly(ethylene glycol)
PEG-*b*-PCL	poly(ethylene glycol)-*block*-poly(ε-caprolactone)
PEG-*b*-PLA	poly(ethylene glycol)-*block*-poly($_{D,L}$-lactic acid)
PEI	polyethylenimine
PET	Positron emission tomography
PI3K	Phosphoinositide-3-kinase
PLL	Poly-$_{L}$-lysine
PS	Phosphatidylserine
RAFT	Regioselective addressable functionalized template
RAPA	Rapamycin
Q7d x 3	Every 7 days for 3 weeks
Q4d x 3	Every 4 days for 3 weeks
RC	Regenerated cellulose
RES	Reticuloendothelial system
RGD	Arginine-glycine-aspartic acid
ROI	Region of interest
RP-HPLC	Reverse-phase high performance liquid chromatography
RPMI medium	Roswell park memorial institute medium
SBR	Signal-to-background ratio
SD	Standard deviation

SLN	Sentinel lymph node
SPECT	Single photon emission computed tomography
SPION	Superparamagnetic iron oxide nanoparticle
SUV	Standard uptake value
T_g	Glass transition temperature
TdT	Terminal deoxynucleotidyl transferase
T_m	Melting temperature
TUNEL	Tdt-mediated dUTP nick end labeling
UK	United Kingdom
UV	Ultraviolet
VEGFR	Vascular endothelial growth factor
VIS	Visible
Wgt	Weight

1 Introduction

1.1. Polymeric micelles for drug delivery

Polymeric micelles, in general, are spherically shaped nanoparticles generated by synthetic amphiphilic block copolymers (ABCs) consisting of hydrophobic and hydrophilic blocks in aqueous medium.[1-4] Amphiphilic di- or tri-block copolymers spontaneously self-assemble into a hydrophobic core/hydrophilic shell structure above their critical micelle concentration (CMC) driven by hydrophobic interaction along with the dehydration of hydrophobic blocks. The hydrophobic core serves as a reservoir for solubilization of hydrophobic components while the hydrophilic shell interfaces the aqueous environment. The most widely used hydrophilic blocks are composed of poly(ethylene glycol) (PEG). A dense brush of PEG ensures micelle solubility in an aqueous medium. There is flexibility in selecting hydrophobic blocks, such as poly(ester)s and poly($_{L}$-amino acid)s, and this flexibility provides versatile and predictive features of polymeric micelles. For example, poly(ε-caprolactone) (PCL) is a semicrystalline polymer with a melting temperature (T_m) of 55 °C, whereas poly($_{D,L}$-lactic acid) (PLA) is fully amorphous with a glass transition temperature (T_g) of 50 °C.[5] Therefore, it is anticipated that poly(ethylene glycol)-*block*-poly(ε-caprolactone) (PEG-*b*-PCL) micelles hold a "solid-like" core, expand less in particle size after the payload incorporation, and provide slower drug release kinetics in comparison to poly(ethylene glycol)-*block*-poly($_{D,L}$-lactic acid) (PEG-*b*-PLA).

The most important basis of polymeric micelles as a drug delivery system is their ability to increase the aqueous solubility of numerous hydrophobic drugs or drug candidates, noting that Lipinski reported in 2000 that a large number of drug candidates have very poor solubility in water and fail to reach the required solubility level offering therapeutic potency in clinical trials.[6]

Other important physicochemical aspects of polymeric micelles for drug delivery include their controlled particle size, sustained release kinetics of payloads, drug loading capacity, and physical stability, which are achieved by manipulating the mass ratio of hydrophilic and hydrophobic blocks, substituting hydrophobic blocks to others, or applying a crosslinking strategy.[3, 7] In addition to physicochemical benefits, polymeric micelles can prolong drug circulation time in the blood stream, favorably deliver drugs to targets such as cancerous and inflamed tissues, and support the enhanced biomedical activity of drugs at the therapeutic site of action, based on the manner of passive targeting or active targeting with further modifications.[2, 3]

1.1.1. Passive (angiogenesis-associated) targeting through the enhanced permeability and retention (EPR) effect

A dense brush of PEG on intravenously injected polymeric micelles masks incorporated drugs from the mononuclear phagocytic system (MPS), also known as the reticuloendothelial system (RES), and prevents the process of opsonization followed by phagocytosis, leading to the extended plasma residence time.[8] The typical particle size of polymeric micelles ranges from 20 to 100 nm.[9] On the basis of physiological parameters, particles > 100 nm in size tend to experience higher hepatic uptake and particles < 10 nm in size are easily cleared by renal excretion.[10] This implies that substantial amounts of polymeric micelles in the size range from 20 to 100 nm can reside in the blood stream long enough to carry more drugs to tumors. These features partially contribute to the passive targeting of polymeric micelles to cancerous or inflamed tissues.

Importantly, intravenously introduced polymeric micelles can passively target solid tumor tissues by the enhanced permeability and retention (EPR) effect based on the unique physiological properties of tumors: interstitial compartments of organs and tumors are separated from the intravascular compartment by the endothelium (Figure 1.1).[3] This creates a barrier for the extravasation of drugs into tumor tissues. Normal tissues are less leaky due to the tight junctions of endothelial cells with a small window of < 2 nm in pore size, whereas endothelial cells in tumors are widely discontinuous and enlarged up to 1.2-2 μm of functional pore size.[11] As a result, enlarged gaps between endothelial cells make blood vessels unusually leaky. Additionally, as cancerous cells highly proliferate at an increased rate of 30-40 fold relative to normal cells, they require greater amounts of blood capillaries (which are leaky) for the supply of extra oxygen and nutrients, as well as for gas exchange and waste removal, known as angiogenesis.[3] Angiogenesis during rapid tumor growth also results in an abnormally deficient lymphatic drainage, causing extended resident time of drugs in tumors[12] These physiological properties of tumors have given rise to a key rationale of passive targeting of polymeric micelles to tumors through the EPR effect as these induce extravasation of polymeric micelles from blood vessels to the interstitial space.

Several polymeric micelle systems passively targeting cancers have been evaluated in clinical trials.[9] For example, a phase II clinical trial of Genexol-PM, a Cremophor EL-free PEG-*b*-PLA polymeric micelle formulation carrying paclitaxel (PTX), showed favorable efficacy in patients with metastatic breast cancer (45.3-72.3% response rate) compared with the conventional Cremophor EL-based PTX (21-54% response rate).[13] A phase I clinical trial of NC-6004, a PEG-poly(aspartate) polymeric micelle formulation containing cisplatin, showed that

NC-6004 did not induce significant nephrotoxicity at the high dose of 120 mg/m^2, noting that nephrotoxicity is commonly caused by medium-high dose of cisplatin.[9]

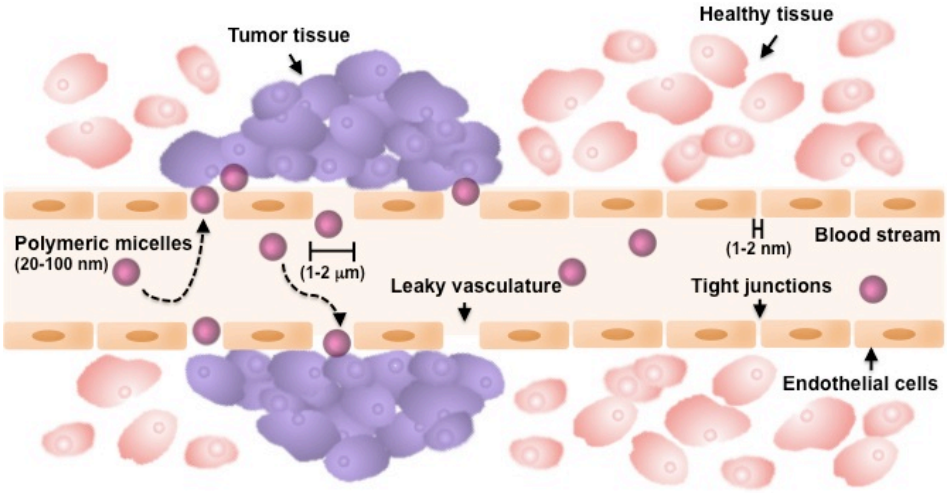

Figure 1.1. Passively targeted polymeric micelles to tumor tissues through the EPR effect.

1.1.2. Physiological barriers and tumor priming effect

Although drug delivery using polymeric micelles can benefit from the EPR effect, it does not guarantee uniform distribution of polymeric micelles in tumor tissues due to the tumor heterogeneity.[14, 15] The delivery of drugs into tumor cells is a 3-step process: polymeric micelles gather in blood vessels near tumor tissues, cross the vasculature endothelium, and penetrate through the interstitial space to enter tumor cells.[16]

As aforementioned, it has been proven that abundant blood vessels are recruited around the tumor tissues (angiogenesis) and that polymeric micelles can preferentially locate near tumor tissues; however, distribution of blood vessels in tumors is highly irregular in the architectural aspect: tumor vessels are heterogenous in their spatial distribution, dilated, and tortuous.[3, 14, 15] In some tumor tissues, highly proliferating tumor cells compress blood vessels with solid stress and result in collapsed vessels in tumors. This implies that not all tumors bear permeable and leaky

blood vasculature weaving around tumor tissues to support the EPR effect. For the same reason, crossing the endothelium through expanded fenestrations is irregular as the size/distribution of window is also heterogeneous.

The deficient lymphatic drainage can ideally allow polymeric micelles to extensively reside in tumors; however, the abnormally deficient lymphatic drainage system contributes tumor heterogeneity as well: the normally functioning lymphatic network exists near the margin of solid tumor tissues, but the abnormally deficient lymphatic drainage mainly exists in the center of tumor tissues.[17] This dysfunctional lymphatic system in the center of tumors, which does not impair tumor cell survival, fails to remove excess fluid from tumor tissues, stores it in the center of tumor tissues, and contributes to interstitial hypertension in the center of solid tumor tissues, is called interstitial fluid pressure (IFP).[16, 17] The interstitial hypertension is also largely induced by the density of the tumor tissues from the large tumor cell population in the center of tumors. The consequence of the gradient in interstitial pressure across the tumor tissues hinders delivery of drugs deeper into the tumor tissues. Several approaches have been reported to alter the physiological properties of tumor tissues and enhance delivery of nanomedicine. Jain *et al* proposed a strategy named "normalization" of tumor vasculature in 2010.[16] Blocking proangiogenic molecules, such as vascular endothelial growth factor (VEGF), decreased in vessel density and diameter in tumor tissue, removed immature vessels, and restructured the vasculature into that resembling normal vessels. This normalization of tumor vasculature reduced IFP and in turn, induced deeper penetration of drug molecules into tumors. Au *et al* showcased a strategy of "tumor priming" effect on solid tumors that intravenous pretreatment of a potent drug inducing apoptosis, such as PTX, could reduce tumor cell density, expand interstitial space,

enhance the uptake rate of the following drugs to tumors, and eliminate drug concentration gradient of drugs between periphery and the center of solid tumors (Figure 1.2).[17, 18] For example, in the FaDu human hypopharyngeal carcinoma xenograft model, Au *et al* achieved a higher fraction of apoptotic cells, lower tumor cell density, rapid drug penetration, higher drug accumulation, and more uniform drug distribution in tumor tissues with the treatment schedule of the pulse of a high dose of PTX, followed by the remainder of the dose given 24 hr later, as compared to continuous infusion of the same total dose of PTX over 24 hr. Another example was that intravenously pre-administrated 40 mg/kg of Taxol (PTX in Cremophor EL formulation) improved the tumor-selective delivery and efficacy of following 20 mg/kg of Doxil (doxorubicin HCl liposomes) due to the tumor priming effect on FaDu xenograft model.

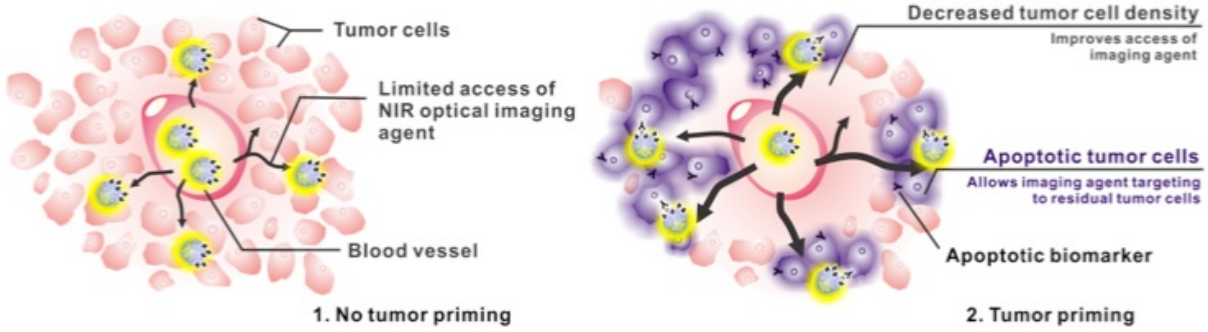

Figure 1.2. Examples of the delivery of near-infrared (NIR) imaging agent to solid tumors without and with tumor priming.

1.1.3. The hallmarks of cancer and active targeting

Recent advances in nanotechnology have explored active targeting of cancer by decorating polymeric micelles with targeting moieties.[19] Targeting moieties, in general, have been chosen based on the characteristics and hallmarks of target cancer. In 2000, Weinberg *et al* made an effort to simplify hallmarks of cancer into six categories: self-sufficiency in growth

signals, insensitivity to anti-growth signals, tissue invasion and metastasis, limitless replicative potential, sustained angiogenesis, and evading apoptosis (Figure 1.3).[20] The hallmarks of cancer have provided good resources for selecting targeting moieties in drug delivery.[19, 20] Vascular endothelial growth factor receptor-2 (VEGFR-2), the most relevant inducer of tumor angiogenesis, and $\alpha_v\beta_3$, a receptor overexpressed in neovascular endothelial cells, have been actively targeted by nanoparticles conjugated with VEGF monoclonal antibodies (mAbs) and Arginine-Glycine-Aspartic Acid (RGD) peptides, respectively, aiming for anti-angiogenesis therapy for cancers. The matrix metalloproteinases (MMPs), endopeptidases playing an important role in tumor invasion and metastases, have been widely aimed to target and treat metastatic cancers. The folate receptor (FR) is one of the most investigated targets for chemotherapy in a broad range of cancers, such as ovarian, lung, brain, head and neck, and breast cancers. FR is overexpressed in many cancer cells as folic acid is essential for functioning in rapidly growing cells. Folate-conjugated nanoparticles have been successfully shown to have efficacy in acute myelogenous leukemia. The epidermal growth factor receptor (EGFR), a receptor mediating cell growth and proliferation, is also highly expressed in over one-third of solid tumors at their advanced stages; therefore, the tumor targeting strategies using mAbs have been investigated in various types of cancers, such as colorectal and head and neck cancers.

The careful consideration of general hallmarks of cancers has encouraged the development of effective drug delivery systems utilizing targeted polymeric micelles.[19] Cancer is too variable to simplify because the physiological changes of cancers are variable across the spectra of cancer types.[14] There are large variations depending on the host (sex, age and genetics) and evidence of multiple tumor subpopulations within the single cancer. Additionally, identical

cancer type can have various physiological and biomolecular differences depending on the origin site and stages of cancer. Most importantly, most target molecules or receptors are not exclusively present in cancer cells but are also found on normal cells. The expression rate of target molecules or receptors also varies in different patient individuals.

Apart from the hallmarks of cancer, there are stimuli-based (or stimuli-responsive) active targeting approaches, such as the use of apoptosis as a biomarker of a tumor response to the chemotherapy.[21] One of the most studied apoptosis targeting strategies is to develop carriers for drugs or imaging agents that recognize phosphatidylserine (PS) on the surface of cell membranes under the apoptotic conditions. In quiescent cells, adenosine triphosphate (ATP)-dependent translocation (flippase: inward transport, floppase: outward transport) controls PS to locate predominantly in the inner leaflet of plasma membrane.[22, 23] Upon apoptosis induction, the mitrochondrial apoptogenic factor activates phospholipid scramblase (bi-directional lipid scrambling), destroying phospholipid migration and PS asymmetric structure. As a result, PS is exposed on the outer leaflet of plasma membrane of apoptotic cells. PS has been considered as an attractive target for apoptosis imaging in oncology mainly because PS is a unique feature of apoptotic cells, regardless of how apoptosis was induced before the imaging. In oncology, as chemotherapy is one of the most widely used treatments, information on tumor response to chemotherapy, predicting chemosensitivity, and tracking apoptotic evidence after chemotherapy in patients is a key step to making a decision for the future chemotherapy regimen. Weissleder and colleagues developed active Cy5.5-annexin V to image apoptotic cells in both cyclophosphamide chemosensitive and cyclophosphamide chemoresistant Lewis lung carcinomas. The results proved that the active Cy5.5-annexin V preferentially accumulated in

cyclophosphamide-pretreated chemosensitive cancer.[21] The use of annexin V is one of the most common methods of detecting PS in apoptotic cells. However, because of the weaknesses of annexin V-based apoptosis targeting, such as high molecular weight and requirements of high extracellular Ca^{2+} level for complete annexin V binding to PS, several alternatives based on peptide conjugation have been proposed to substitute annexin V. Recently, Li and colleagues showed that SAAC(^{99m}Tc)-PSBP-6, a small molecular weight peptide binding PS, could be used to assess early response to chemotherapy (PTX)-induced apoptosis in B16/F10 melanoma and 38C14 lymphoma tumor models with increased uptakes of *ca.* 112% and *ca.* 142%, respectively, whereas tumor uptakes of non-targeted ^{18}F-FDG were *ca.* 63% and *ca.* 67%, respectively.[24, 25]

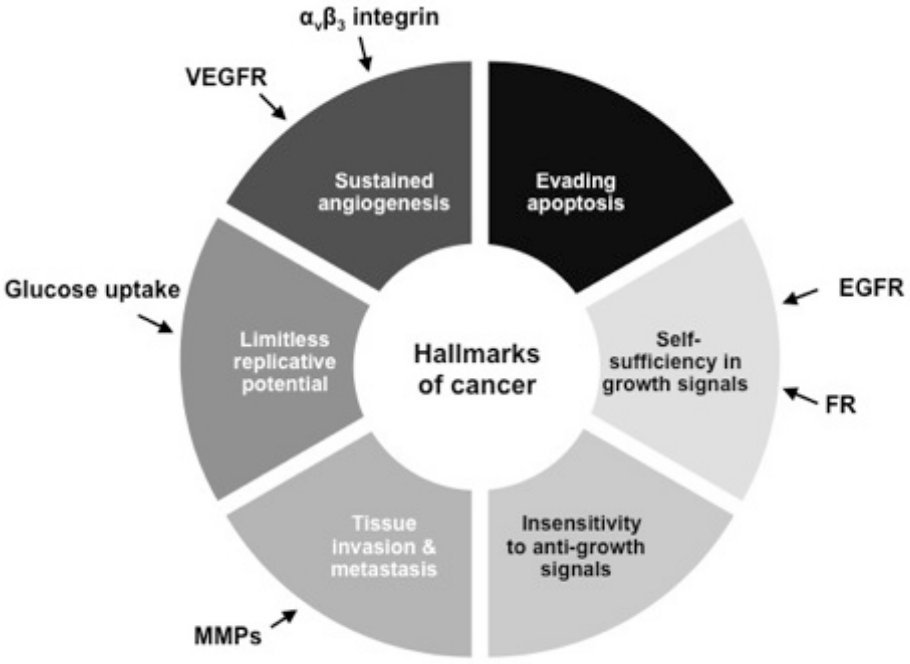

Figure 1.3. The hallmarks of cancer (reproduced from reference 20: Weinberg *et al*., 2000).

1.2. Combination drug delivery in oncology

As cancer research has progressed, combination chemotherapy has become a standard regimen over single drug-based monotherapy. The primary idea of combination chemotherapy is to reduce chemoresistance and achieve synergistic anticancer effects. In 1965, Frei *et al* initiated a strategy of combination chemotherapy in children with acute leukemia: Methotrexate/6-mercaptopurine, prednisone/6-mercaptopurine, and prednisone/vincristine improved complete remission rate over individual treatments.[26, 27] Frei *et al* also demonstrated that alternating methotrexate and 6-mercaptopurine at 28-day intervals did not prolong the duration of remission whereas the concurrently administrated combination of methotrexate and 6-mercaptopurine did. Since then, efforts to find effective drug combinations have been made to improve anticancer efficacy in oncology. For example, one of the most effective chemotherapy regimens for adult Hodgkin's lymphoma is known as ABVC, which consists of adriamycin, bleomycin, vinblastine, and dacarbazine. For non-small cell lung cancer (NSCLC) and ovarian cancer treatments, the combination of carboplatin and PTX is widely used in clinics.[28] Successful drug combinations are required to have distinctive mechanism of action, intervene in multiple biological pathways, prevent cross-talk between different membrane receptors, and minimize additive toxicity. Yet concurrent combination drug delivery is challenging due to the difficulty of managing a regimen of multiple drug components, multi-drug-associated side effects, and the risk of additive toxicity caused by two or more vehicles used for drug solubilization.

Recently there have been efforts to develop polymeric micelle-based drug delivery platforms to concurrently deliver multi-drugs and overcome the aforementioned issues. One of the co-encapsulation approaches for concurrent multi-drug delivery is to physically incorporate drugs into the hydrophobic core of polymeric micelles.[29] This approach is versatile, easy to

implement, and requires no chemical modification of drugs or polymers. The polymeric micelles physically carrying multi-drugs tend to increase water solubility of drugs, delay drug release kinetics, and nullify surfactants or cosolvents-related toxicity concerns (by using biocompatible or biodegradable polymers). For example, previously, Shin *et al* could co-incorporate PTX (microtubule stabilizer), rapamycin (RAPA, mammalian target of rapamycin (mTOR) inhibitor), and 17-allylamino-17-demethoxygeldanamycin (17-AAG, heat shock protein 90 (Hsp90) inhibitor) in PEG-*b*-PLA micelles (Triolimus, Figure 1.4) using a simple solvent evaporation method in various drug(s)-in-micelle combinations, such as 1-in-1, 2-in-2, and 3-in-1, but PTX failed to be incorporated in PEG-*b*-PLA micelles alone as a 1-in-1 formulation.[30] Presumably, due to the intermolecular interaction among three hydrophobic drug components, 3-in-1 micelles remarkably increased solubility of drug components, PTX, RAPA, and 17-AAG, in water, and delayed *in vitro* release of three drugs from 3-in-1 micelles compared to those from 1-in-1 micelles. Most importantly, intravenously injected 3-in-1 PEG-*b*-PLA micelles carrying 60, 30, and 60 mg/kg of PTX, RAPA, and 17-AAG, respectively (q4d x 3), synergistically delayed tumor growth in A549 NSCLC and MDA-MB-231 human breast cancer xenograft models with no notable toxicity, presumably by simultaneously inhibiting both PI3K/Akt/mTOR and Ras/Raf/MEK/ERK signaling pathways, noting that these two pathways are known to be interconnected with complicated feedback mechanisms.[31] The pharmacokinetic profiles of PTX, RAPA, and 17-AAG at 10, 5, and 10 mg/kg, respectively, from 3-in-1 PEG-*b*-PLA micelles showed identical pharmacokinetics as those from 1-in-1 micelles.[32] The well-designed polymeric micelles-based combination drug delivery not only brings multi-drugs together but also offers benefits on favorable pharmacological effect without additive toxicity.

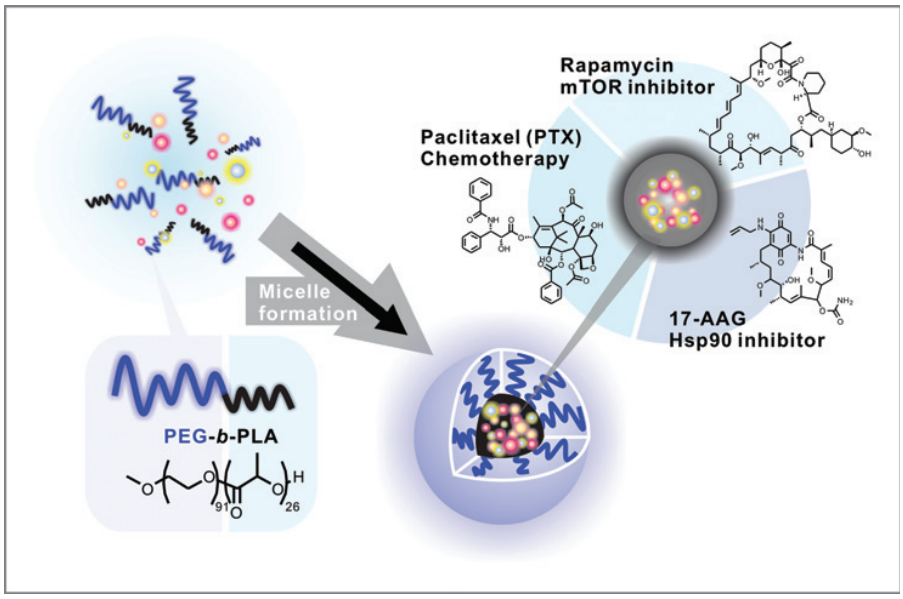

Figure 1.4. Composition of Triolimus, PEG-*b*-PLA micelles carrying PTX, 17-AAG, and RAPA (from reference 31: Hasenstein *et al*., 2012).

1.3. Human cancer imaging

Recent technological advances have accelerated the development of screening, staging, and treatment of human cancers. Currently, there are five imaging modalities available in clinics to diagnose, stage, and plan follow-up care after treatments in oncology, such as ultrasound, computed tomography (CT), magnetic resonance imaging (MRI), single photon emission computed tomography (SPECT), and positron emission tomography (PET).[33] Both macroscopic imaging systems (CT, MRI), which provide anatomical and physiological information and microscopic imaging systems (PET, SPECT), which provide physiological and molecular information, are useful for routine clinical practice in radiation oncology.[34] Because each modality has its own strengths and weaknesses, new technologies have been developed based on the combination of formats such as PET/CT and PET/MRI. These imaging modalities, alone or

in combinations of two, have improved diagnostic accuracy, staging, and physiological response of cancer after treatments as pre- and post-operative imaging technologies. However, during surgery, the eyes and hands (visual inspection and palpation) of surgeons are still the dominant decision-making factors in surgical process. Although fluorescence imaging (microscopic imaging system) has been mainly used for research purposes, it is rapidly emerging due to the clear translational potential into clinics, particularly in surgical oncology. The most attractive property of fluorescence imaging is a capability to generate intraoperative optical fluorescence images to guide surgeons in a real-time manner in the operation room by providing valuable information on the monitor/goggle that naked eyes cannot detect. Fluorescence imaging and its application in surgical oncology will be briefly overviewed in sections 1.3.1-1.3.3.

As shown in Table 1.1, the nanotechnology accompanied with radio- and optical-pharmaceuticals for imaging has been extensively investigated because exogenous contrast agents can be well-associated with nanoparticles in a variety of ways to obtain desirable advantages such as enhancing selectivity to the disease site and improving the stability of incorporated contrast agents, as aforementioned in section 1.1.[35, 36]

Modality	Resolution (voxel/pixel dimensions)	Depth	Clinically available exogenous contrast agent	Strength	Weakness	Cost	Nano-technology under development
Ultrasound	1μL (1x1x1 mm)	cm	Microbubbles	Good vascular imaging High resolution	Poor bone imaging Air interfaces	$$	Polymeric nanoparticle
Computed tomography (CT)	1μL (1x1x1 mm)	No limit	Iodine	Excellent bone contrast	Molar concentrations of contrast agents required	$$	Gold nanoparticle
Magnetic resonance imaging (MRI)	1μL (1x1x1 mm)	No limit	Chelated Gd^{3+}	Excellent soft tissue contrast	Long imaging acquisition time required Poor bone imaging	$$$	Superparamag-netic iron oxide nanoparticle (SPION)
Single photon emission computed tomography (SPECT)	1.7 cm^3 (12x12x12 mm)	No limit	^{99m}Tc ^{111}In ^{67}Ga	Versatile Quantatitive	Low sensitivity and resolution	$$	Liposome
Positron emission tomography (PET)	0.5 cm^3 (8x8x8 mm)	No limit	^{18}F	Versatile Excellent solid tumor contrast	Cyclotron required	$$$	Carbon nanotube
Optical fluorescence imaging	0.01 mm^2 (0.1x0.1 mm) (2-D)	< 1cm	Indocyanine green (ICG)	Good surface-based disease contrast Intra-operative use	Limited detection depth	$	Quantum dot Polymeric nanoparticle

Table 1.1. Overview of cancer imaging modalities (modified from references 33 and 34: Frangioni *et al.,* 2008 and Weissleder *et al., 2008*).

1.3.1. Optical fluorescence imaging

The basic principle of optical fluorescence imaging is illustrated in Figure 1.5. A light source emits a bundle of lights and lights in a specific wavelength reach the object through the filter selected by investigators.[37] Light is attenuated and enters the tissue as a result of multiple effects such as absorption, scattering (randomization of the direction of light), and reflection. The first propagation of light is to be absorbed into tissue. When light reaches the skin under large angles, a large portion of the light reflects on the surface, and the rest of the non-reflected light travels into the tissue. As tissue contains various components such as water, lipids, oxyhemoglobin, and deoxyhemoglobin, avoiding absorption of light in such unnecessary components is a key rule to maximizing the amount of light approaching the fluorophore. Unlike the visible (400-650 nm) and the infrared (> 900 nm) light spectra, in the near-infrared (NIR) region (700-900 nm), light absorption by water (~ 900 nm), oxyhemoglobin (~ 600 nm), and deoxyhemoglobin (~ 600 nm) diminishes, leading to the deeper tissue penetration of photons. Tissues and cells contain endogenous fluorophores that become fluorescent when excited by mainly UV or visible radiation (known as autofluorescence).[38] Consequently, NIR light can travel from the millimeter to the centimeter scale through blood and tissues with minimal light scattering and autofluorescence, whereas visible light penetrates tissue on the micrometer scale. As a result, the use of probes in the NIR range can offer a high signal-to-background ratio (SBR), reducing negative influence by intrinsic factors.

Scattered and absorbed photons in tissue meet extrinsic fluorophore, and this fluorophore gains in energy entering an excited state. The energy in the excited state rapidly decay to that of the lowest vibration level (vibrational relaxation) and, in turn, return to the ground state, emitting

photons in all directions, including refraction and reflection. Eventually, the part of the photons emitted from extrinsic fluorophore (the desired fluorescence), reflected from the surface of the skin and emitted from intrinsic fluorophore in tissue (autofluorescence) are all detected by the camera system. In order to distinguish the desired photons emitted from extrinsic fluorophore, excited photons with a specific wavelength can be separately collected after passing through an appropriate filter.

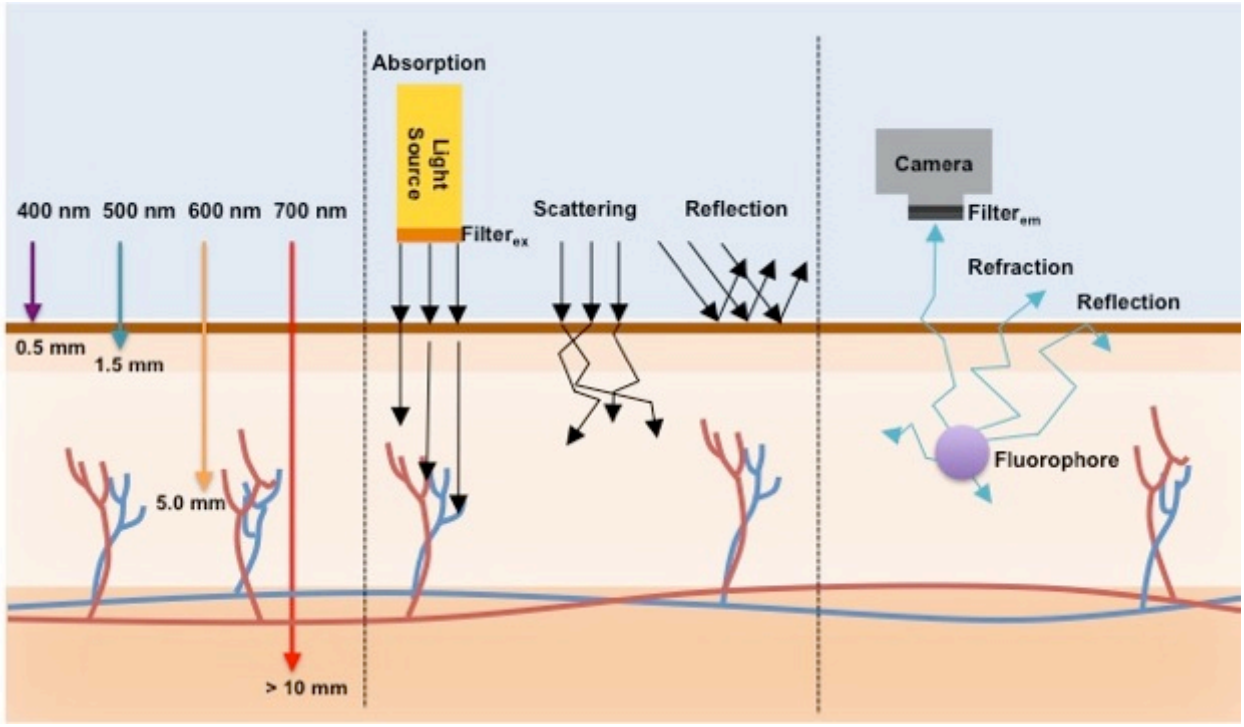

Figure 1.5. Light penetration through tissue in different wavelength spectra (left) and light traveling into tissues originated from light source (middle) or light traveling onto camera from fluorophore (right) (modified from reference 37: Keereweer *et al*., 2013).

The intrinsic autofluorescence of cancerous tissues correlated with the increased hemoglobin concentration due to the angiogenesis can be useful to detect tumor tissues. For

example, Softscan® (Figure 1.7, Advanced Research Technologies, Montreal, Canada) is a time-domain optical mammography that measures photon migration through the breast to distinguish benign tumors.[39] However, "tumor-specific autofluorescence" is not reliable because the autofluorescence signal varies over time and other factors (inflammation, scar formation, and chemotherapy) can cause strong artifacts of signals. Most importantly, autofluorescence is not sufficient to define small tumor tissues and tumor margins.

Figure 1.6. Softscan® (Advanced Research Technologies, Montreal, Canada).

A few exogenous NIR fluorophores, for example, indocyanine green (ICG) and 5-aminolevulinic acid (5-ALA), are in clinical use. More NIR fluorophores (small molecule organic dyes and quantum dots) and fluorophore-conjugated or -carrying nanoparticles have been in development. Figure 1.7 briefly summarizes types of optical imaging agents that have been developed and reported in the last decades. Fluorophores (ICG, cyanine derivatives, or Alexa dyes) are chemically linked to targeting ligands such as small molecules, antibodies and peptides to offer active targeting effects with high SBR (Figure 1.7, top left).[40] In a further development, "activable probes" have been found to increase SBR. One of examples of activable

probes is shown in Figure 1.7 (top right): fluorophores-peptide conjugates are attached on a poly-$_L$-lysine (PLL) backbone and are quiescent in fluorescence intensity (at the self-quenched state) because of their close proximity. Then peptide spacer is cleaved by MMP-2 when activable probes are delivered to invasive tumor tissues/cells, triggering the release of fluorophores from the PLL backbone which become brightly fluorescent.[40, 41]

The same approach can be made using nanoparticles. Instead of conjugating fluorophores to targeting moieties, fluorophores can be incorporated in tumor-targeting nanoparticles surface-decorated with targeting moieties (known as fluorophore-doped or -containing nanoparticles), as shown in Figure 1.7 (bottom left). Fluorophore-doped nanoparticles can incorporate a large amount of lipophilic fluophores and produce high fluorescence intensity when those break apart and release fluorophores at the target site. In particular, polymer-coated nanoparticles carrying fluorophores increase photostability of fluorophores owing to the polymer coating, which prevents penetration of oxygen and reduces photobleaching.[40, 42] Nanoparticles also permit incorporation of multi-components; for example, loading both chemotherapeutic and imaging agents in nanoparticles enables the "theranostics" (therapy + diagnostics) strategy to "see and treat" tumors.[43] Another type of optical imaging agents is "activable fluorophore-incorporated nanoparticles." For example, the conjugates of fluorophore and caspase-specific peptides are linked to the branched-polyethylenimine (PEI) and form nanoparticles in aqueous solution (Figure 1.6, bottom right). Under the apoptotic condition, caspase-3 and -7 cleave peptides, destroy the structure of nanoparticles and paint apoptotic tissues/cells with a strong fluorescence intensity due to the release of fluorophores.[44]

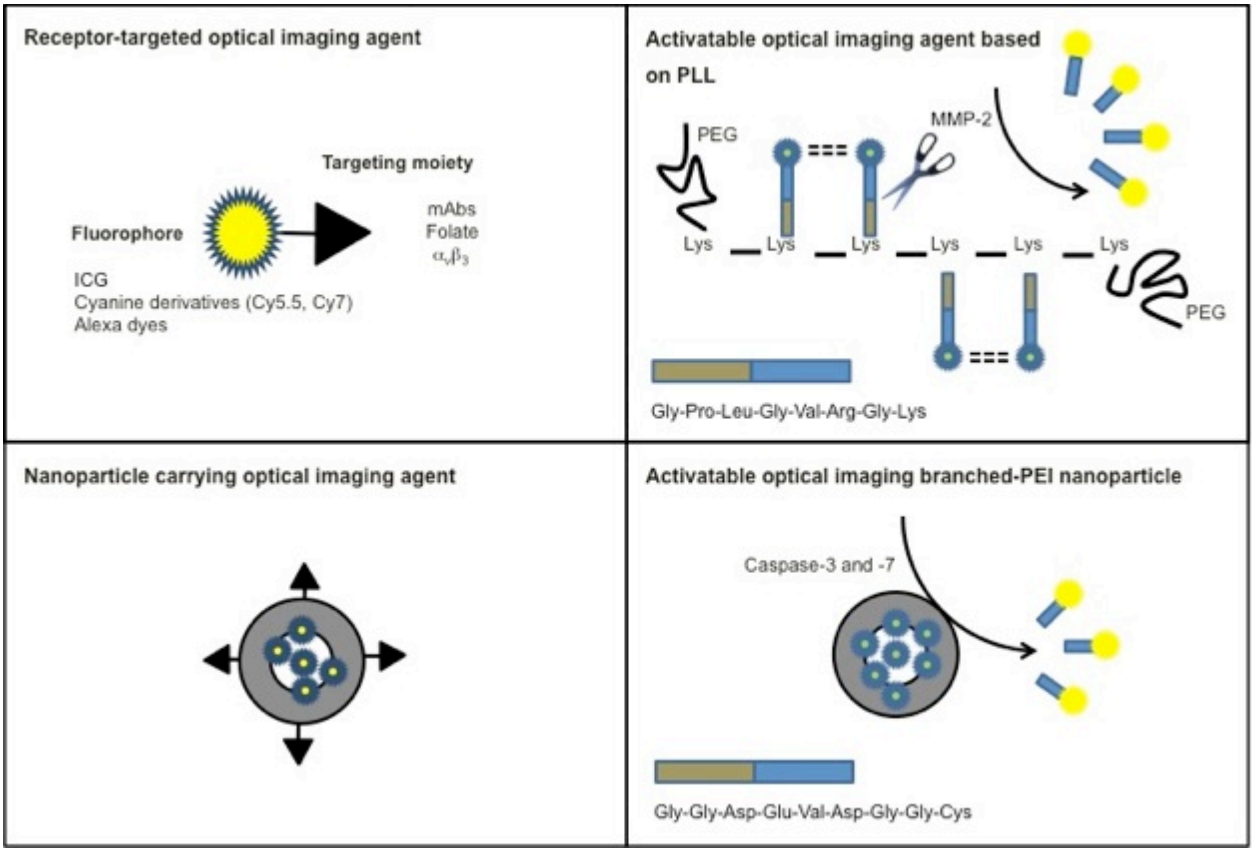

Figure 1.7. Summary of types of optical imaging agents in development (adapted and modified from references 40-44).

1.3.2. Intraoperative NIR optical imaging and surgical guidance

Investigators have reported successful preclinical and clinical applications of fluorescence optical imaging for sentinel lymph node (SLN) mapping, diagnostic tumor imaging, and intraoperative surgical guidance. SLN mapping using optical imaging systems by now has been most extensively studied in various diseases such as breast, colorectal, cervical, and head-and-neck cancers, and melanoma. Tanaka *et al* used NIR fluorophore HSA800 (human serum albumin (HSA) covalently conjugated to the CW800) to map SLN and further utilize SLN images for surgical guidance in a melanoma swine xenograft model.[45] The same group of

investigators successfully made a transition from the NIR fluorescence imaging system to the image-guided oncologic surgery in a clinical trial.[46, 47] A mixture of ICG:HSA as an imaging agent and Fluorescence-Assisted Resection and Exploration (FLARE^{TM}) as a real-time optical imaging system were used for intraoperative SLN mapping of breast cancer patients and as a result, in 4 out of 6 patients, the identical SLNs were identified by both ^{99m}Tc-sulfur colloidal lymphoscintigraphy and intraoperative optical imaging.

Van Dam *et al* reported that intraoperative tumor-specific fluorescence imaging with a folate-FITC (fluorescein isothiocyanate) could showcase the potential application of improved intraoperative staging and radical cytoreductive surgery in ovarian cancer patients. The number of tumor deposits detected by surgeons with the fluorescence imaging guidance (median 34) was significantly higher than the number detected with visual observation alone (median 7).[48]

To date, surgical removal of tumor nodules is the most effective cancer treatment. However, the outcome of surgical tumor resection varies, as illustrated in Figure 1.8.[49] Tumor debulking by the traditional surgical process is efficient in removing primary tumor tissues and can leave a clean margin around the primary tumor tissue. However, traditional surgery limits detection of small metastatic tumor nodules, and consequently, invasive procedures may be necessary to get rid of suspicious tumor nodules as small nodules are barely detectable under normal light or by palpation. The ideal tumor resection can be expected when the optical fluorescence imaging system is paired with surgical oncology. Advances in optical fluorescence imaging technology provide intraoperative images that can guide oncologic surgeons with useful extra information to refine surgical performance. In its clinical application, intraoperative optical image-guided surgery also allows surgeons to find small and suspicious tumor nodules that

traditional surgery with visual observation and exploration cannot detect, leading to improved surgical accuracy. Lastly, as a consequence of enhanced surgical performance and accuracy, a decrease of residual tumor tissues and a prolonged survival can be ultimately achieved.

Figure 1.8. Various outcomes in the identical surgical object (modified from reference 49: Thurber *et al*., 2010).

1.3.3. Clinical application of intraoperative optical imaging in ovarian cancer, limits, and challenges

Optical imaging has the practical potential to improve cancer surgery by providing real-time intraoperative guidance. For example, surgeons can conduct traditional white-light surgery on the object and reinvestigate suspicious regions with intraoperative fluorescence imaging.[37] In particular, intraoperative optical imaging for ovarian cancer can make significant differences in cancer remission and survival rates. Of all gynecological malignancies, ovarian cancer is the most frequent cause of death, due to the lack of screening tools and clear clinical presentation in the early stage of ovarian cancer, and as a result, ovarian cancer is mostly diagnosed at the advanced stage.[48] Ovarian cancer at advanced stages tends to spread by continuous interaction with the adjacent organs and rapid growth in the peritoneum. Ovarian cancer is routinely treated by combination strategy of surgery and chemotherapy with platinum and taxane analogues. However, over 70% of ovarian cancer patients experience recurrence within a year, and the main

reasons for cancer recurrence is insufficient surgical removal of tumor nodules and small metastatic tumor deposits in the peritoneum.[50] Although it is challenging to image and diagnose ovarian cancer with conventional imaging techniques, optical imaging can be well suited for providing surgical guidance to permit improved image-guided debulking surgery of peritoneal metastases. Depth limitations of optical imaging might not be relevant during the surgical process because surgeons will bring the object of interest closer to the surface from the opened peritoneum. The image acquisition is fast and simultaneous. Regarding the imaging agents, intraoperative optical imaging that exploits NIR fluorescence offers high sensitivity and specificity with low inherent autofluorescence background.[33] Van Dam *et al* conducted the first human proof-of-principle study in ovarian cancer patients and showcased a potential benefit of intraoperative fluorescence imaging in staging and debulking surgery for ovarian cancer using intravenously injected folate-FITC.[48]

However, there are limits and challenges for the clinical translation of intraoperative optical imaging. This technology requires the development of both tumor-specific contrast agents and dedicated intraoperative camera system.[37] The contrast agents require high binding affinity to tumor tissues with adequate retaining time, while non-bound agents are rapidly cleared from the circulation. It is also crucial to have the appropriate camera and display system that can sensitively select fluorescence signals and display those in both macroscopic and microscopic images. From a financial point of view, development of diagnostic or intraoperative imaging agents is less favorable in pharmaceutical industries because such agents in the diagnostic field are not administrated over periods of time as long as other pharmaceuticals or as frequently as other pharmaceuticals. Although there are still limitations and challenges of intraoperative

imaging to overcome, the intraoperative optical imaging technique can be a powerful tool for improving surgical outcomes in combination with further developments in the field of surgical oncology.

1.4. Research proposal

1.4.1. Rationale

Although the majority of cancers are heavily treated by extensive surgery in combination with chemotherapy, incomplete surgical tumor resection still causes fatal recurrence. Intraoperative NIR optical image-guided cancer surgery has been investigated as a promising technique to detect tumor margins and small metastatic tumor nodules in as detailed a manner as possible and minimize residual cancerous tissues, thereby prolonging survival.

The successful clinical transition of the intraoperative NIR optical imaging technique can be made by utilizing polymeric micelles aiming at cancer-specific delivery of contrast agents that will cause high SBR in fluorescence signals. NIR fluorescent contrast agents employing polymeric micelles can be delivered to cancer by various strategies, such as passive targeting (the EPR), tumor priming, and active targeting effects.

(1) Passive targeting that relies on the EPR effect can simply permit passive delivery of polymeric micelles carrying contrast agents to solid tumor tissues due to the unique physiological property of solid tumors.

(2) Delivery of polymeric micelles carrying contrast agents to solid tumors can be enhanced when tumor tissues are primed by pretreatment of potent cytotoxic agents causing

significant decreases in cancer cell number, density, and interstitial pressure (tumor priming effect).

(3) Actively targeted polymeric micelles deliver contrast agents to cancer with improved specificity by the active targeting effect. Depending on the targeting moiety decorating the surface of polymeric micelles, polymeric micelles carrying contrast agents can actively target primary tumors, metastases, angiogenesis, or apoptotic tumors with the unique targeting mechanism.

Preclinical studies of polymeric micelles incorporating NIR contrast agents in clinically relevant cancer-bearing xenograft models are critical to understanding the principles and phenomena of tumor visualization with regard to passive targeting, tumor priming, and active targeting effects. Most importantly, findings and discussions in these interdisciplinary studies can provide a basis for developing a promising optical imaging system to facilitate surgical guidance, accuracy, and better outcome in surgical oncology.

1.4.2. Objectives

The primary objective of this dissertation is to investigate delivery systems of NIR contrast agents employing polymeric micelles to visualize tumors by passive targeting, tumor priming, and active targeting effects. Further clinical potentials and merits of polymeric micelles on neoadjuvant chemotherapy followed by intraoperative optical image-guided surgery were evaluated in clinically relevant metastatic ovarian cancer-bearing xenograft model.

1.4.3. Specific aims

1. To design and characterize PEG-*b*-PCL micelles carrying a NIR fluorophore, DiR (1,1'-dioctadecyltetramethyl indotricarbocyanine iodide), which can deliver DiR molecules to solid tumor tissues in a subcutaneous human colon cancer-bearing xenograft model by the passive targeting effect.

2. To enhance delivery of PEG-*b*-PCL micelles carrying DiR to primed solid colon tumor tissues (primed by an IV injection of PEG-*b*-PLA micelles carrying PTX, 17-AAG, and RAPA) by the tumor priming effect, using a 2-step strategy: tumor priming with PEG-*b*-PLA micelles carrying PTX, 17-AAG, and RAPA followed by NIR fluorescence optical imaging with PEG-*b*-PCL micelles carrying DiR.

3. To design and characterize PEG-*b*-PCL micelles carrying PTX, cyclopamine (CYP), and gossypol (GSP) as an intraperitoneal (IP) neoadjuvant therapy in a metastatic peritoneal ovarian cancer-bearing xenograft model.

4. To evaluate a proof-of-concept of the active targeting effect, using a 2-step strategy. Intraoperative optical imaging of therapy-induced apoptosis by a tandem of PEG-*b*-PCL micelles can improve surgical accuracy and outcome for metastatic peritoneal ovarian cancer. In the first step, apoptosis can be induced by PEG-*b*-PCL micelles carrying PTX, CYP and GSP as an IP neoadjuvant ovarian cancer therapy (specific aim 3). In the second step, therapy-induced apoptosis imaging can be obtained by systemically administrated apoptosis-

targeting PEG-*b*-PCL micelles carrying DiR in metastatic peritoneal ovarian cancer-bearing xenograft model.

2 Noninvasive Cancer Imaging by Poly(ethylene glycol)-*b*-poly(ε-caprolactone) Micelles Containing a Near-Infrared Probe: Characterization of Micelles Carrying a Near-Infrared Probe and Evaluation of Their Passive Targeting effect

This chapter has been published in full: Cho H.; Indig G. L.; Weichert J. P.; Shin H.; Kwon, G. S., *In vivo* cancer imaging by poly(ethylene glycol)-*b*-poly(ε-caprolactone) micelles containing a near-infrared probe. *Nanomedicine* **2012**, *8* (2), 228-236.

2.1. Introduction

In a clinical point of view, near-infrared (NIR) probe-incorporated polymeric micelles could be used for both the diagnosis of tumors and the guidance of surgery. Surgical removal of tumors is the best method to treat cancers if the entire tumor can be completely removed. However, complete tumor removal depends on how well the tumor is delineated and how impeccably surgery is performed.[9, 51-61] Monitoring the presence of tumor tissues remaining in surrounding surgical margins by using NIR probe-incorporated polymeric micelles and the removal of tumor tissues are prudent courses of action for avoiding recurrence.[62] It is expected that NIR probe-incorporated polymeric micelles can provide decisive guidance for improved surgical removal of tumors. Here, we investigated the optical imaging of cancer by NIR probe-incorporated polymeric micelles in a colon cancer-bearing animal model. DiR (1,1'-dioctadecyltetramethyl indotricarbocyanine iodide) is a lipophilic carbocyanine dye that is strongly light-absorbing and used as a tool in different research areas, such as lipid membrane-potential sensor, organelle stains for mitochondria and endoplasmic reticulum and long-term labeling of cells in culture.[63, 64] For optical imaging, DiR absorbs in the NIR region (λ_{max} = 750 nm), and it has a high quantum yield. For the clinical applications in optical imaging, PEG-*b*-PCL micelles are a promising class of nanocarriers for DiR for the following reasons: The preparation of PEG-*b*-PCL micelles that contain DiR is facile; PEG-*b*-PCL micelles increase the water solubility of the highly lipophilic DiR in aqueous solution;[65-70] PEG-*b*-PCL micelles have prolonged *in vivo* circulation due to the kinetic stability of PEG-*b*-PCL micelles in blood with respect to disassembly and the avoidance of the reticuloendothelial system (RES) by PEG-*b*-PCL micelles.[71] As a result, passive tumor targeting of PEG-*b*-PCL micelles has been achieved by the

enhanced permeability and retention (EPR) effect in xenograft models.[66, 71] We studied PEG-*b*-PCL micelles with NIR probe, DiR, in a quenched or nonquenched state (Figure 2.1). Although both states showed different kinetic profiles for NIR probe release *in vitro* and photophysical properties *in vivo*, both states achieved high signals in tumor tissues for optical imaging.

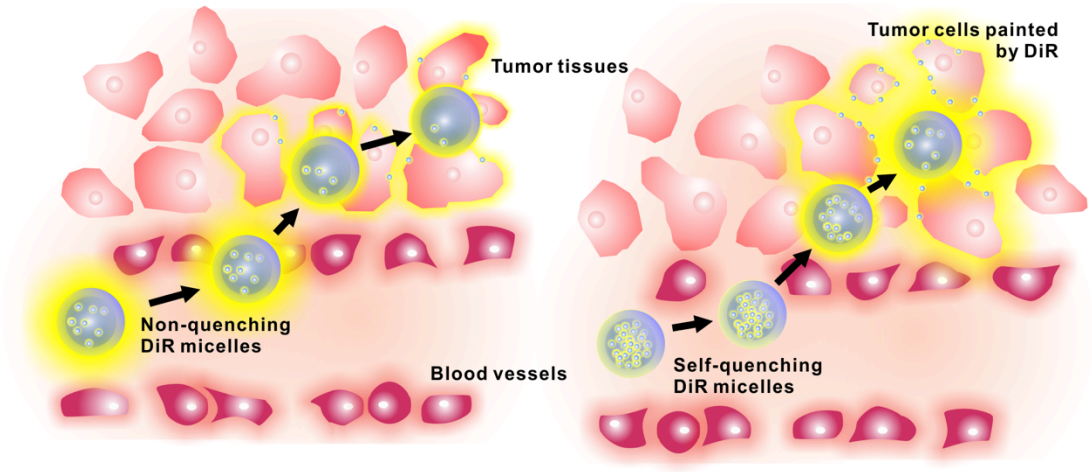

Figure 2.1. Delivery of DiR molecules to cancer either in non-quenched or self-quenched states.

2.2. Materials and methods

2.2.1. Preparation and characterization of PEG-*b*-PCL micelles with DiR

DiR-loaded PEG-*b*-PCL micelles were prepared by dissolving 4.0-200 mg of PEG-b-PCL (5k:10k, M_w/M_n: 1.3), (Polymer Source, Dorval, Quebec, Canada) and 0.10-0.50 mg of DiR (Invitrogen, Carlsbad, California) in acetone (2.0 mL) followed by the dropwise addition of 0.9% sodium chloride (2.0 mL) by a syringe at a flow rate of 1.0 mL/sec with vigorous mixing. Acetone was evaporated from the aqueous solution by stirring at room temperature (20-25 °C) for 1 hr. The PEG-*b*-PCL solution was centrifuged for 5 min at 10,000 g to remove unincorporated DiR that was insoluble. The aqueous micelle solution was filtered through 0.2

μm nylon syringe filter (National Scientific, Rockwood, Tennessee). The aqueous solubility of DiR was determined by UV-visible measurements on a Cary 100 Bio UV-visible spectrophotometer (Varian, Palo Alto, California). Particle-size distributions of PEG-*b*-PCL micelles with DiR were determined by dynamic light scattering (DLS) measurement, using a Zetasizer Nano-ZS (Malvern Instruments, Ltd., Malvern, United Kingdom) at a detection angle of 173 degrees and a He-Ne ion laser ($\lambda = 633$ nm) for the incident beam. Fluorescence measurements on DiR were conducted on AMINCO-Bowman Series 2 spectrofluorometer (Thermo Scientific, Rockford, Illinois) with excitation and emission wavelengths at 745 and 800 nm, respectively. For fluorescence measurements on DiR, absorbances were kept below 0.3 to preclude inner filter effects. The fluorescence self-quenching of DiR as a function of its loading in PEG-*b*-PCL micelles was evaluated by monitoring its fluorescence emission relative to its fluorescence emission upon 100% DiR release from PEG-*b*-PCL micelles; this was realized by freeze-drying of an aliquot of PEG-*b*-PCL micelles, followed by dissolution of the solid sample in acetone and measurement of DiR fluorescence.

2.2.2. *In vitro* DiR release profile for PEG-*b*-PCL micelles

Aqueous micelle solutions (2.5 mL) were loaded into 20,000 MWCO Slide-A-Lyser® dialysis cassettes (Thermo Scientific) and cassettes (n = 4) were then placed in 0.9% sodium chloride solution (2.0 L) at 37 °C with stirring. The sodium chloride solution was refreshed every 3 hr to ensure sink conditions. Samples of 100 μL were withdrawn from cassettes, and cassettes were replenished with 100 μL fresh sodium chloride solution. Sampling intervals were 1, 2, 3, 6,

12, 24, 48, 72 and 96 hr. Withdrawn samples at each time point were analyzed for the amount of DiR release on a Cary 100 Bio UV-visible spectrophotometer.

2.2.3. Xenograft model

LS180 human colon carcinoma cells (kindly provided by Dr. Jamey Weichert, University of Wisconsin-Madison) were cultivated in minimum essential medium (MEM) including Earle's salts (Cellgro, Manassas, Virginia), supplemented with 2% sodium bicarbonate, 1% nonessential amino acids, 1% sodium pyruvate, 10% fetal bovine serum, 1% L-glutamine and 100 U/mL penicillin-streptomycin solution. Cultivated cells were kept at 37 °C under an atmosphere of 5% CO_2 in a humidified incubator. About 1 week prior to imaging, 1×10^6 LS180 cells were inoculated subcutaneously into the right flanks of anesthetized female 6- to 8-week-old athymic nude mice (Laboratory Animal Resources, Madison, Wisconsin). General anesthesia was induced with 1.5% isoflurane/oxygen and anesthesia was maintained with 1% isoflurane/oxygen. All animal experiments were performed with human care of animals and approved by University of Wisconsin-Madison's Instituional Animal Care and Use Committee guidelines, and procedures were in accordance with the institutional guidance.

2.2.4. Animal surgery and tissue excision

Animals were treated in a sterile environment. Ninety-six hours after injection of PEG-*b*-PCL micelles with DiR, mice were sacrificed by CO_2 asphyxia. A midline incision was done with microsurgical instruments under white light illumination, and organs such as liver, lung,

heart, spleen, and kidneys, as well as muscle tissue, were removed. The skin of mice was also removed over the tumor and tumor excision was performed.

2.2.5. NIR fluorescence imaging of DiR

For imaging, DiR-loaded PEG-*b*-PCL micelles, representing 10 μg of DiR, were injected in the tail vein of anesthetized animals when sizes of tumors reached to 80-100 mm^3. Whole-body fluorescence images were recorded 10 min, 1, 4, 9, 12, 24, 48, 72 and 96 hr after intravenous administration using Xenogen IVIS® 200 Series (Caliper Life Sciences, Hopkinton, Massachusetts) equipped with a 150 watt quartz halogen lamp and a 1 mW power scanning laser. Mice (n = 3 for each micelle formulation) were placed in the dorsal and lateral positions to obtain whole-body optical images. Tumors, organs and tissues removed at 96 hr post injection were scanned before dehydration began and their *ex vivo* images were obtained. All images were acquired by back-thinned, back-illuminated grade 1 CCD camera with the following parameters: exposure time = 1 sec; binning = medium; f/stop 2. Filter sets were fixed with the following parameters for DiR: excitation at 745 nm and emission at 800 nm. Acquired images were measured and analyzed with Living Imaging® software. The distribution of DiR in the whole body was quantified by average radiant efficiency, total photons per second per square centimeter per steradian in the irradiance range (microwatts per square centimeter): $[p/s/cm^2/sr]/[\mu W/cm^2]$. The tumor-specific accumulation of DiR was evaluated by signal-to-noise ratio: average radiant efficiency at the region of interest (ROI) was drawn around the tumor to average radiant efficiency at the opposite region indicating background tissue (left flank). Horizontal radiant efficiency maps were drawn by Living Imaging® software according to the

fluorescence intensity of DiR at the horizontal line passing through the center of a tumor. DiR uptake values in organs and tumors were calculated by its fluorescence relative to its fluorescence in muscles after tissue excision. *In vitro* fluorescence measurements of DiR-loaded PEG-*b*-PCL micelles seeded in 96-well black fluorescence microplates were also performed using the Xenogen IVIS® 200 Series.

2.3. Results

2.3.1. Characterization of DiR-loaded PEG-*b*-PCL micelles

Table 2.1 shows the results on the solubilization of DiR by PEG-*b*-PCL micelles at varied ratios of DiR to PEG-*b*-PCL. DiR is practically insoluble in water (< 1.0 μg/mL). PEG-*b*-PCL micelles readily increased the water solubility of DiR from 44 to 230 μg/mL with an increase in the quantity of PEG-*b*-PCL. The loading efficiency (wgt $DiR_{PEG\text{-}b\text{-}PCL}$ /wgt $DiR_{initial}$) was approximately 90%. At a low DiR-to-PEG-*b*-PCL ratio (1:400), PEG-*b*-PCL micelles had an average hydrodynamic diameter of 32 nm with a low polydispersity index (PDI). At a higher ratio of DiR to PEG-*b*-PCL (1:40), PEG-*b*-PCL micelles had a higher average hydrodynamic diameter of 47 nm and higher PDI, possibly due to a higher average number of DiR per micelle. Assuming that the association number of PEG-*b*-PCL micelles is 200, there were about 7 DiR per PEG-*b*-PCL micelle at the DiR-to-PEG-*b*-PCL ratio of 1:400,[65] whereas there were about 74 DiR per PEG-*b*-PCL micelle at the DiR-to-PEG-*b*-PCL ratio of 1:40.

Micelles (DiR:PEG-*b*-PCL) (weight:weight)	Z-average diameter (nm)	PDI (Polydispersity index)	Aqueous solubility of DiR in micelle formulations (μg/mL)
1:40 (Self-quenching)	47.06 ± 1.80	0.154 ± 0.017	44.52 ± 4.05
1:25	41.98 ± 0.44	0.123 ± 0.014	56.37 ± 8.01
1:33	41.76 ± 3.39	0.088 ± 0.065	137.9 ± 5.49
1:50	37.80 ± 0.88	0.044 ± 0.035	150.5 ± 6.33
1:80	36.61 ± 0.75	0.062 ± 0.029	175.7 ± 2.98
1:100	32.39 ± 3.46	0.055 ± 0.024	176.9 ± 4.15
1:400 (Non-quenching)	31.90 ± 1.07	0.044 ± 0.054	229.9 ± 3.07

Table 2.1. Z-average diameters of DiR-loaded PEG-*b*-PCL micelles and aqueous solubility of DiR.

2.3.2. Self-quenching of DiR in PEG-*b*-PCL micelles

Figure 2.2A shows the relative fluorescence intensity of DiR at varied ratios of DiR to PEG-*b*-PCL. At a ratio of 1:400, the fluorescence of DiR incorporated in PEG-*b*-PCL micelles was close to the fluorescence of DiR after 100% release from PEG-*b*-PCL micelles in acetone, suggesting that DiR in the core region exists in a non-self-quenched state (monomers). As the content of DiR increased in PEG-*b*-PCL micelles, there was a loss in quantum yield, presumably due to DiR-self-quenching at higher levels of multiply occupied PEG-*b*-PCL micelles. At a ratio of 1:40, the fluorescence of DiR incorporated in PEG-*b*-PCL micelles was less than 10% relative to the acetone control. At about 74 DiR per PEG-*b*-PCL micelle, DiR self-quenching is evident, consistent with multiply occupied PEG-*b*-PCL micelles that have cores with diameters less than 10 nm and the presence of ground-state species of DiR. The absorption spectra of DiR at varied

ratios of DiR to PEG-*b*-PCL are consistent with DiR self- quenching in PEG-*b*-PCL micelles at high loading (Figure 2.2B). As the ratio increased, absorption bands at lower wavelengths relative to the major absorption band of DiR at 745 nm increased. The absorption bands at 650 and 692 nm signify the self- association of DiR in PEG-*b*-PCL micelles, resulting in the self-quenching of fluorescence. The *in vitro* fluorescence intensity of DiR detected by IVIS® 200 Series in a 96-well plate is shown in Figure 2.2C. At a ratio of 1:400, the fluorescence of DiR loaded in PEG-*b*-PCL micelles showed the highest intensity, whereas at a ratio of 1:40, the fluorescence of DiR loaded in PEG-*b*-PCL micelles had a lower intensity than DiR solubilized in acetone at the same level. The fluorescence intensities of DiR in PEG-*b*-PCL micelles and acetone were concentration dependent. In summary, PEG-*b*-PCL micelles could effectively raise the water solubility of DiR and DiR existed in either a quenched or nonquenched state in the cores of PEG-*b*-PCL micelles, depending on the extent of DiR incorporation.

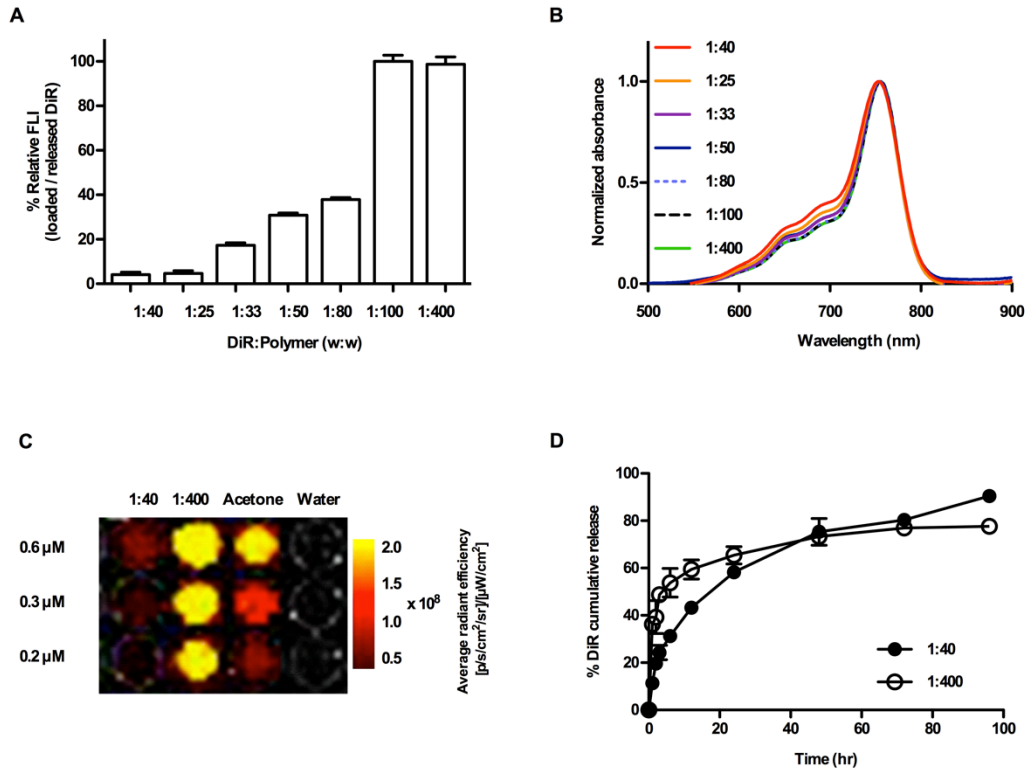

Figure 2.2. (A) Fluorescence intensity of DiR-loaded PEG-*b*-PCL micelles relative to free DiR, and (B) Normalized absorbance spectra of DiR-loaded PEG-*b*-PCL micelles at varied ratios of DiR to PEG-b-PCL. (C) Fluorescence imaging of DiR (0.6, 0.3 and 0.2 µM) in a multi-well format obtained by Xenogen IVIS® 200 Series; DiR-loaded PEG-*b*-PCL micelles (1:40 and 1:400), DiR in acetone, and water (autofluorescence). (D) *In vitro* release profiles of DiR from PEG-*b*-PCL micelles (1:40 and 1:400).

2.3.3. *In vitro* DiR release kinetics for PEG-*b*-PCL micelles

The release kinetics of DiR for PEG-*b*-PCL micelles at 1:40 (self-quenched) and 1:400 (nonquenched) ratios were investigated (Figure 2.2D). At a 1:40 ratio, DiR was gradually released from PEG-*b*-PCL micelles with the half-life for DiR release at approximately 20 hr. On the other hand, the release of DiR from PEG-*b*-PCL micelles at a ratio of 1:400 was biphasic, and most of the DiR was released from PEG-*b*-PCL micelles over 6 hr, followed by a more

gradual release profile over 24 hr. The half-life for nonquenched DiR release was approximately 1 hr. After 48 hr, 70% of the DiR had been released from PEG-*b*-PCL micelles irrespective of the quenched state of the DiR. It is assumed that self-quenched DiR molecules in PEG-*b*-PCL micelles at a 1:40 ratio are aggregated and slowly transform into monomers as function of time. This release profile for DiR from PEG-*b*-PCL micelles was further verified with *in vivo* optical imaging experiments.

2.3.4. NIR fluorescence imaging of DiR-loaded PEG-*b*-PCL micelles in tumor-bearing mice

Tumor-specific accumulation of PEG-*b*-PCL micelles that contain DiR was determined using noninvasive optical imaging based on fluorescence intensity of DiR. The time-dependant whole-body biodistribution of PEG-*b*-PCL micelles that have quenched or nonquenched DiR was monitored by radiant efficiency (Figures 2.3A and B). In a quenched state (1:40), the fluorescence of DiR gradually emerged from the dorsal and lateral portions of the mice over several hours (Figure 2.3E). On the other hand, DiR in a nonquenched state (1:400) showed a rapid onset of fluorescence intensity that was much stronger than that of DiR in a quenched state. Although the fluorescence signal of DiR slowly decreased after approximately 10 minutes, the fluorescence signal of quenched DiR increased over time, reaching a similar value at dorsal and lateral sites after approximately 24-48 hr. Figures 2.3C and D show the fluorescence intensity of DiR following a horizontal line passing through tumors. Radiant-efficiency maps of DiR taken at various time points after injection of the PEG-*b*-PCL micelles that contain quenched DiR showed gradual tumor-specific accumulation of DiR as function of time; the strongest signal from the tumor region was observed after 12 hr and the lowest signal from DiR was detected at

10 min post injection. On the other hand, maps for PEG-*b*-PCL micelles that contain nonquenched DiR showed an opposite tendency; the strongest fluorescence signal of DiR was observed within 1 hr after injection, whereas the lowest signal of DiR was obtained after 72 hr. Tumor-to-muscle ratios for DiR indicate that the tumor-specific accumulation efficiencies were not significantly different for the quenched and nonquenched groups. The ratios were calculated to be approximately 2; however, the ratios calculated from 1:40 group were slightly higher than the ratios for the 1:400 group (Figure 2.3F). The DiR solubilized in 20% DMSO solution was also injected into xenograft mice through the tail vein but no tumor specific accumulation could be observed, noting that slight fluorescence signals were observed in liver (Figure 2.4). Moreover, the whole-body signal was so weak that the biodistribution of DiR could not be visualized with the same fluorescence intensity scale that was used for PEG-*b*-PCL micelles. These results suggest that DiR-incorporated PEG-*b*-PCL micelles are superior to free DiR for visualizing tumor tissues in living mice. No notable toxicity of DiR-loaded PEG-*b*-PCL micelles during the animal experiments was found.

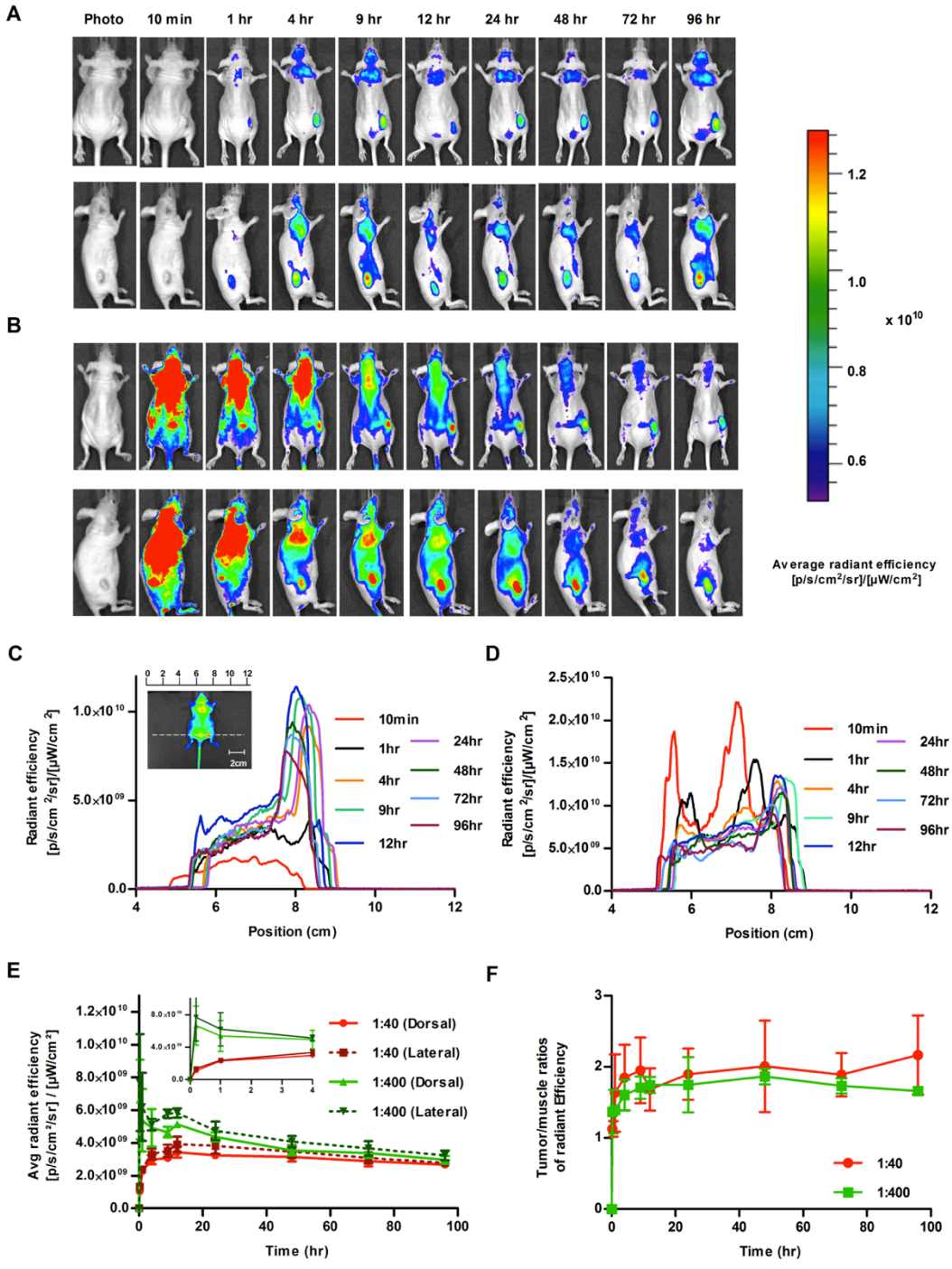

Figure 2.3. *In vivo* fluorescence whole-body images of mice with LS180 human colon carcinoma. Time-dependent images of (A) DiR-loaded PEG-*b*-PCL micelles (1:40) (B) DiR-loaded PEG-*b*-PCL micelles (1:400) in dorsal (upper) and lateral (below) views. Time-dependent radiant efficiency maps according to horizontal lines passing

through the center of tumors for (C) DiR-loaded PEG-*b*-PCL micelles (1:40) and (D) DiR-loaded PEG-*b*-PCL micelles (1:400). (E) Calculated average radiant efficiency of DiR-loaded PEG-*b*-PCL micelles (1:40 and 1:400) in dorsal portions and lateral views as a function of the time based on Figure 2.3A and B (Expanded figure from 0 to 4 hr time point was inserted). (F) Relative radiant efficiency of DiR distributed in tumors in comparison with muscles over time in living mice.

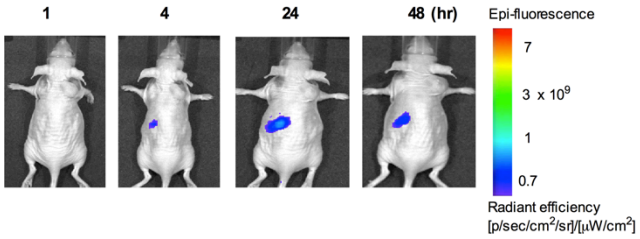

Figure 2.4. *In vivo* fluorescence whole-body images of mice with LS180 human colon carcinoma. DiR (10 μg per animal) in 20% DMSO solution was intravenously injected and whole-body fluorescence images of mice were obtained at 1, 4, 24, and 48 hr post injection.

2.3.5. *Ex vivo* NIR fluorescence imaging of DiR-loaded PEG-*b*-PCL micelles in excised tissues

Color-coded NIR fluorescence images of excised tissues (lung, heart, spleen, tumor, kidneys, liver and muscle) (Figures 2.5A and B) were obtained after 96 hr. Fluorescence images showed that the strongest signal of DiR was observed in tumor tissues, followed by the liver and spleen, for both quenched and nonquenched groups of DiR-loaded PEG-*b*-PCL micelles. The optical signal of DiR from the lungs was also relatively strong for PEG-*b*-PCL micelles with nonquenched DiR (Figure 2.5B). The fluorescence intensity ratio of tumor to muscle was approximately 30 for PEG-*b*-PCL micelles with quenched DiR, whereas the fluorescence intensity ratio of tumor to muscle was approximately 43 for PEG-*b*-PCL micelles with nonquenched DiR (Figure 2.5C).

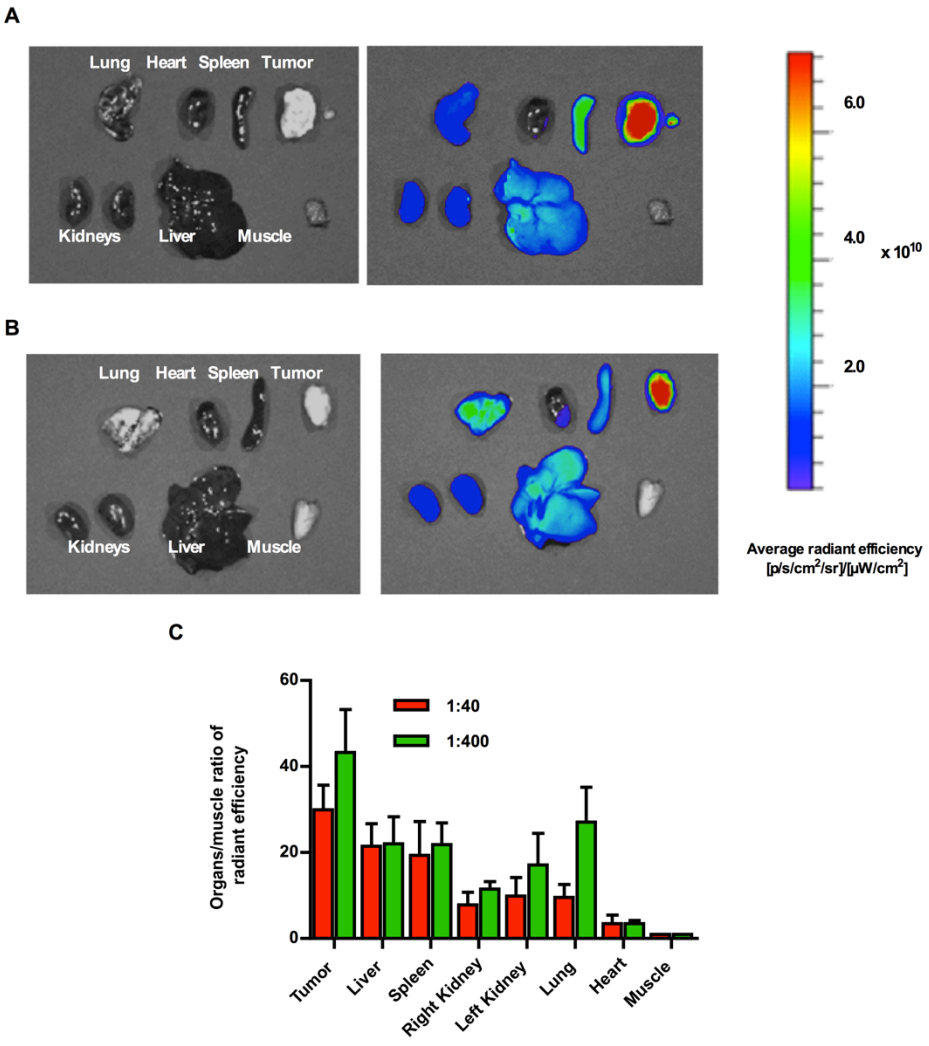

Figure 2.5. *Ex vivo* optical image of tissues for (A) DiR-loaded PEG-*b*-PCL micelles (1:40) and (B) DiR-loaded PEG-*b*-PCL micelles (1:400). (C) Relative radiant efficiency of DiR distributed in excised organs in comparison with muscle after 96 hr.

2.3.6. Residual tumor detection after surgical removal

Xenograft animals were sacrificed 96 hr post injection and their dorsum was opened, guided by the strong fluorescence signal of DiR. Tumor tissue was selectively visualized in the incised animal body due to NIR fluorescence emitted by DiR-loaded PEG-*b*-PCL micelles

(Figure 2.6A). The completeness of tumor removal depends on how finely the tumor is delineated before and during surgery. The LS180 human colon carcinoma solid tumor was removed as completely as possible from the xenograft animal under white light and residual tumor was detected by NIR fluorescence imaging of DiR (Figure 2.6B). A weak fluorescence signal from DiR was detectable at the site of tumor resection, pointing to remaining tumor margins that were not clearly observable by the naked eye during the surgical removal of the primary tumor (Figure 2.6C).

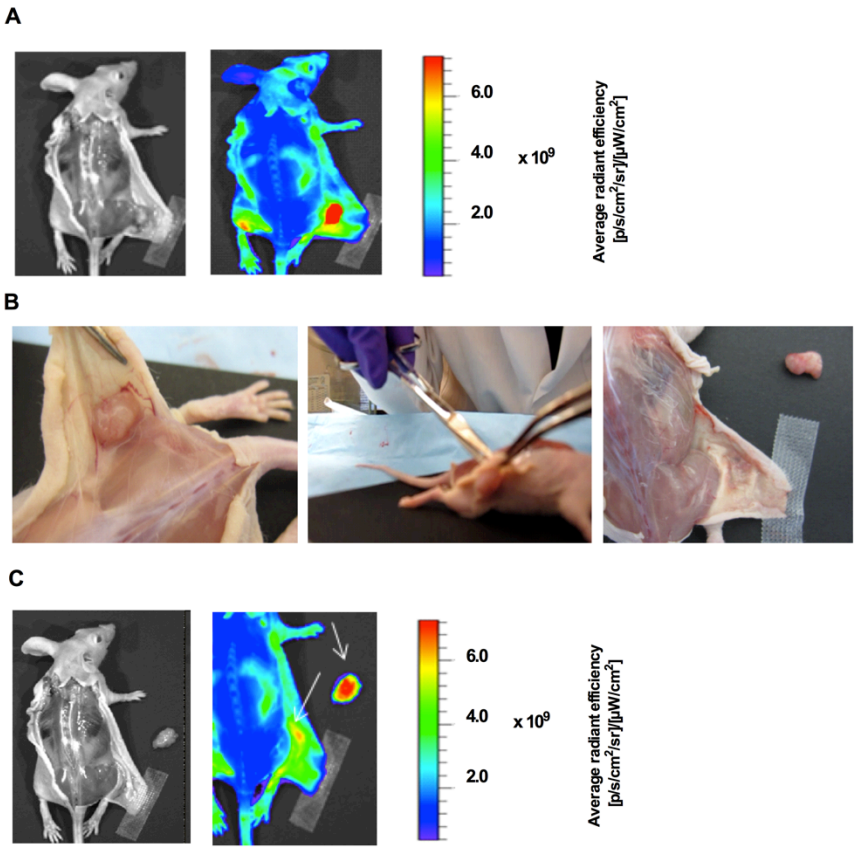

Figure 2.6. Detection of tumor and margins before and after surgery by DiR-loaded PEG-*b*-PCL micelles (1:400). (A) Before surgery, (B) surgical tumor removal and (C) after surgery.

2.4. Discussion

DiR was successfully incorporated into PEG-*b*-PCL micelle by a simple nano-precipitation method and the average diameter of DiR-loaded PEG-*b*-PCL micelles was about 30-50 nm. PEG-*b*-PCL micelles substantially increased the water solubility of DiR, enabling optical imaging experiments in mice. As shown in Table 2.1, the content of DiR in PEG-*b*-PCL micelles could be controlled, resulting in PEG-*b*-PCL micelles that are multiply occupied by DiR. At low occupancy (1:400), photophysical experiments on DiR suggest that the dye exists in a nonquenched state in the cores of PEG-*b*-PCL micelles. At high occupancy (1:40), DiR exists in a quenched state in the cores of PEG-*b*-PCL micelles, probably due to the existence of ground-state species of DiR. Carbocyanine dyes tend to self-associate and exist as H-aggregates. H-aggregates are a one-dimensional array of dyes in which the transition moments of individual monomers are aligned parallel to each other, but perpendicular to the line joining their centers (face-to-face arrangement).[72-76] H-aggregates of DiR do not emit typical fluorescence and their excited states are rapidly deactivated by internal conversion and intersystem crossing. H-aggregates show lower fluorescence intensity than monomers and display blue-shifted absorption spectrum (Figures 2.2A and B).[77] At a ratio of 1:40, DiR molecules are positioned closely and exist also as H-aggregates in the cores of PEG-*b*-PCL micelles, whereas at a ratio of 1:400, DiR molecules are widely separated and exist predominantly as monomers in the cores of PEG-*b*-PCL micelles, resulting in a strong fluorescence signal in comparison with DiR in acetone (Figure 2.2C).

Most researchers have endeavored to avoid dye aggregation and the loss of fluorescence quantum yield for optical imaging.[59] However, we noticed differences in the *in vitro* kinetics of

DiR release for PEG-*b*-PCL micelles, depending on the quantity of incorporated DiR (1:40 *vs*. 1:400) and speculated that *in vivo* optical imaging of DiR in a xenograft model would depend on the release kinetics of DiR from PEG-*b*-PCL micelles. Presumably, H-aggregates of DiR in the cores of PEG-*b*-PCL micelles at 1:40 ratio are responsible for the slow release pattern of DiR obtained *in vitro* (Figure 2.2D), whereas monomers of DiR in cores of PEG-*b*-PCL micelles at 1:400 ratio are quickly released over the first few hr. Thus, it was expected that monomeric DiR in PEG-*b*-PCL micelles would be highly fluorescent after injection and during release from polymeric micelles *in vivo*. In contrast, it was expected that aggregated DiR in PEG-*b*-PCL micelles would have a low fluorescence signal after injection and the optical signal would increase over time due to the release of DiR, which results in the loss of H-aggregates in PEG-*b*-PCL micelles and released monomeric DiR that is highly fluorescent. Real time *in vivo* fluorescence images of DiR injected in either an aggregated state (1:40) or monomeric state (1:400) support these two mechanisms of NIR fluorescence imaging (Figures 2.3A and B). At a 1:40 ratio, the whole-body fluorescence signal from DiR was low and gradually emerged, especially near vascular tissue near the heart region and noticeably at the LS180 human colon carcinoma solid tumor after 4 hr. At a 1:400 ratio, the whole-body fluorescence signal from DiR was high even after 10 min and gradually lost intensity. However, the tumor in the flank region could be readily discerned after 4 hr and quite apparent after 9-24 hr after an increase in tumor signal and loss in background signal. Horizontal radiant efficiency maps going from the left flank to the tumor also showed that the NIR signal from DiR in an aggregated state was low in the left flank and the tumor, and over time the fluorescence signal built up at the tumor. At a 1:400 ratio, the fluorescence signal from DiR was strongest in the tumor and left flank after 10

min and selectivity for the tumor is gained over time, especially after 9 hr. Although the kinetics of *in vivo* fluorescence imaging of DiR depended on its aggregation state in PEG-*b*-PCL micelles, the whole-body optical imaging of tumors was quite similar in terms of selectivity, as shown in Figures 2.3E and F. The tumor-to-muscle ratio was about 2 after 9 hr at a 1:40 ratio and about 1.7 at a ratio of 1:400 at several time points. The tumor-to-muscle ratio indicates a measure of selectivity of an optical imaging agent comparing tumor accumulation to nontarget tissue (muscle). A tumor-to-muscle ratio greater than 1 suggests that the agent has distributed selectively to the tumor.[78] The Prosense 680 (Visen Medical, Woburn, Massachusetts), a commercially available NIR probe in preclinical development, has shown a tumor-to-muscle ratio of about 2.3 *in vivo*.[79] Therefore, DiR-incorporated PEG-*b*-PCL micelles gave equal or better tumor delineation. The tumor selectivity of DiR evidenced by optical imaging probably reflects the EPR effect, enabled by PEG-*b*-PCL micelles. However, pharmacokinetic experiments on DiR and PEG-*b*-PCL micelles are required to prove this hypothesis fully.

Surgical resection of various tissues at 96 hr after the injection of DiR-loaded PEG-*b*-PCL micelles, followed by optical imaging of DiR, confirmed the selectivity of the dye for tumor tissue regardless of the aggregation state of DiR in loaded PEG-*b*-PCL micelles (Figures 2.5A and B). It is noted that the average radiant efficiency of DiR is very high at the solid tumors, approximately 6.0×10^{10} [p/s/cm^2/sr]/[μW/cm^2], reflecting the selective tumor accumulation of DiR-loaded PEG-*b*-PCL micelles, high quantum yield, and dye stability even after 96 hr *in vivo*. In the excised organs, DiR had a remarkably high tumor-to-muscle ratio of 30-43. In this experiment, optical imaging is done without the interference of overlying tissue, *e.g.*, skin and

blood vessels, and it more closely resembles intraoperative procedures in surgical oncology, as opposed to whole-body optical imaging that might have greater diagnostic value.

Surgical incision of mice followed by optical imaging of DiR revealed the clear delineation of tumor tissues (Figure 2.6A). After the removal of skin overlying the tumor region and tumor resection, it was apparent under white light that tumor resection was complete (Figure 2.6B). However, NIR optical imaging by DiR clearly provided evidence of remaining tumor margins (Figure 2.6C). These *in vivo* results suggest that DiR-loaded PEG-*b*-PCL micelles can provide intraoperative guidance for the surgical removal of solid tumors. One limitation of this work is the use of a subcutaneous xenograft model rather than an orthotopic xenograft model that undergoes metastases.

2.5. Conclusions

Noninvasive NIR fluorescence imaging is a promising technique for the intraoperative assessment of solid tumor removal. We incorporated a lipophilic NIR probe, DiR, in PEG-*b*-PCL micelles, resulting in DiR solubilization in water, occupying nanoscopic PEG-*b*-PCL micelles. DiR in a self- quenched or nonquenched state showed different kinetics of release from PEG-*b*-PCL micelles; however, both obtained high tumor delineation (tumor-to-muscle ratio of 30–43 from collected tissues). These results suggest that PEG-*b*-PCL micelles with DiR are a promising nanosized imaging agent that will provide a basis for surgical guidance *via* NIR visualization of tumors, relying on passive targeting effect.

3 Polymeric Micelles for Neoadjuvant Cancer Therapy and Tumor-Primed Optical Imaging: Enhanced Optical Imaging by Tumor Priming Effect

This chapter has been published in full: Cho H.; Kwon, G. S., Polymeric micelles for neoadjuvant cancer therapy and tumor-primed optical imaging. *ACS NANO* **2011***, 5 (11),* 8721-8729.

3.1. Introduction

Nanomaterials such as quantum dots, gold nanoparticles, and nanoparticles that contain fluorescent dyes may accumulate at solid tumors through leaky vasculature, *i.e*. enhanced permeability and retention (EPR) effect,[80-83] and emit fluorescence in the near-infrared (NIR) region,[70, 84] raising the prospect of intraoperative surgical guidance in oncology.[51, 85, 86] While NIR optical imaging will not likely replace other imaging modalities for whole body tumor detection due to attenuation of fluorescence signals by overlying tissue, optically-active nanomaterials may be used for the assessment of tumor margins, adjacent structures, and adjacent tumor deposits during surgery, supplementing visible inspection under white light and palpation.[52, 53, 87] It is noted that complete surgical resection is the single most important predictor of survival in patients with lung, breast, prostate, colon, and pancreatic cancers. However, nanomaterials for NIR optical imaging must fulfill central requirements in safety, targeted delivery,[88, 89] *e.g*. avoidance of mononuclear phagocyte system, and molecular imaging, high target-to-non-target tissue ratio.[52]

While nanomaterials will continue to evolve for NIR optical imaging and certainly merit more attention,[64, 90] strategies that overcome delivery barriers in solid tumors have drawn attention in cancer nanotechnology and may be used to improve efforts in NIR optical imaging in surgical oncology. Jain has highlighted intratumoral barriers that hinder the delivery of nanomaterials into solid tumors for therapy and imaging, noting that nanomaterials > 60 nm in diameter are unable to diffuse effectively in many solid tumors.[16] The distribution of blood vessels throughout solid tumors is uneven; simply, tumor regions lacking blood vessels will receive less nanomaterial than regions perfused with plenty of blood vessels.[17, 18, 91-93] Solid

tumors have high interstitial fluid pressure that diminishes the penetration of nanomaterials from blood vessels into tumors by convection.[92] To overcome delivery barriers at solid tumors, strategies such as co-injection of enzymes that degrade extracellular matrix have been researched. Jain proposed the vascular normalization hypothesis for enhanced intratumoral drug delivery, although its relevance for nanomaterial is less clear.[16] Au and co-workers proposed a strategy, termed "tumor priming," where pretreatment with the single intravenous (IV) injection of a potent anticancer drug such as paclitaxel (PTX) results in tumor cell apoptosis, reduction in tumor cell density, and expansion of interstitial space. As a result, liposomes that contain doxorubicin had higher uptake at solid tumors. It is noted that tumor priming was selective for the solid tumors even though the standard formulation of PTX (40 mg/kg) that contains Cremophor EL was used (Taxol®).[18, 91] Regardless of the proposed strategy for overcoming barriers of nanomaterial uptake into solid tumors, it must be done safely, selectively for solid tumors, and can be achieved after systemic administration, preferably by IV injection or infusion.[7]

Polymeric micelles are a major class of nanomaterials that have entered several clinical trials for drug delivery,[7, 94] and they have drawn recent attention for optical imaging. Herein, we propose a tandem of polymeric micelles for a combined drug delivery and optical imaging strategy, aiming for tumor debulking, tumor priming, and enhanced NIR optical imaging of solid tumors (Figure 3.1). Poly(ethylene glycol)-*block*-poly(*d*, *l*-lactic acid) (PEG-*b*-PLA) micelles act as a nanocontainer for two or three poorly water-soluble anticancer drugs, enabling concurrent IV administration of multiple anticancer drugs for the first time.[95] PEG-*b*-PLA micelles will replace organic cosolvents and toxic surfactants, *e.g.* Cremophor EL, that are required for drug

solubilization for the IV route, noting that PEG-*b*-PLA micelles carrying PTX (Genexol-PM®) are approved in several Asian countries for cancer therapy and are in phase III clinical trials in the USA.[96, 97] In our previous work, PEG-*b*-PLA micelles act as a 3-in-1 nanocontainer for PTX, 17-allylamino-17-demethoxygeldanamycin, and rapamycin (PTX/17-AAG/RAPA), and we hypothesize that 3-in-1 PEG-*b*-PLA micelles can be used for neoadjuvant cancer therapy and for tumor priming for NIR optical imaging (Figure 3.1).[30] For tumor priming, PEG-*b*-PLA is much less toxic than Cremophor EL in Taxol®, noting a 2-fold higher maximum tolerated dose (MTD) for PTX in clinical trials for Genexol-PM®. 2- and 3-drug combinations of PTX, 17-AAG, and RAPA exert synergistic cytotoxicity toward breast, lung, and colon cell lines. After tail vein injection of 3-in-1 PEG-*b*-PLA micelles with PTX/17-AAG/RAPA at 60, 60, and 30 mg/kg on days 0, 4, and 8, there was < 10% body weight change and no deaths, noting that the MTD in nude mice for Genexol-PM is 60 mg/kg on the same dosing schedule and the MTD for Taxol® is 20 mg/kg.[30]

For NIR optical imaging, poly(ethylene glycol)-*block*-poly(ε-caprolactone) (PEG-*b*-PCL) micelles act a long-circulating nanomaterials that accumulate preferentially at solid tumors *via* the EPR effect (Figure 2.3). Allen and co-workers have non-evasively monitored the fate of ^{111}In-labeled PEG-*b*-PCL micelles by microSPECT/CT imaging and shown that they have prolonged circulation in blood and preferential localization at solid tumors (9.0 ± 2% dose/g) in a MDA-MB-231-human breast xenograft model.[98] In the previous chapter, PEG-*b*-PCL micelles have a high capacity for a lipophilic carbocyanine dye, DiR (1,1'-dioctadecyl tetramethyl indotricarbocyanine iodide), a carbocyanine dye that has strong light absorbance in the NIR region (700-800 nm), rendering deep-tissue penetration of light with low autofluorescence.[99] As

shown in previous chapter, in a LS180 human colon xenograft model, PEG-*b*-PCL micelles carrying DiR preferentially illuminated solid tumors, having tumor-to-muscle ratios of 30-43, depending on the aggregation state of DiR in PEG-*b*-PCL micelles. In this chapter, we show how a tandem of 3-in-1 PEG-*b*-PLA and PEG-*b*-PCL micelles carrying DiR can be used for tumor debulking, tumor priming, and enhanced NIR optical imaging of solid tumors in a LS180 human colon xenograft model, coupling progress in drug delivery and NIR optical imaging for advances in integrated cancer therapy involving nanomedicine and surgical oncology.

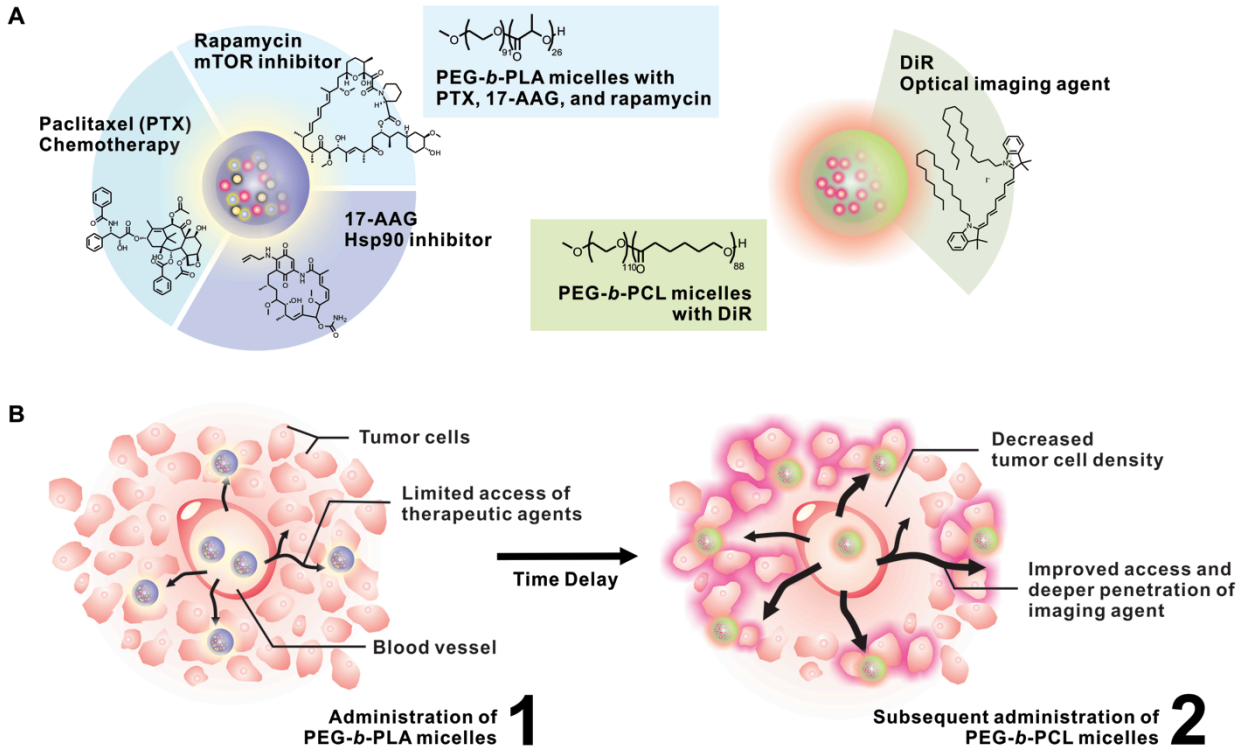

Figure 3.1. (A) The 3-in-1 PEG-*b*-PLA micelles containing PTX/17-AAG/RAPA with the z-average diameter of 37.5 ± 0.74 (PDI: 0.125 ± 0.021) and drug loading capacity of 40.4 ± 1.2% (drugs/polymer), and PEG-*b*-PCL micelles containing DiR with the z-average diameter of 47.05 ± 1.80 (PDI: 0.154 ± 0.017) and DiR loading capacity of 2.3 ± 0.20% (DiR/polymer). (B) Schematic illustration of tumor-primed delivery of NIR optical imaging agent (DiR) by a tandem of PEG-*b*-PLA and PEG-*b*-PCL micelles.

3.2. Materials and methods

3.2.1. Preparation and characterization of 3-in-1 PEG-*b*-PLA micelles and PEG-*b*-PCL micelles carrying DiR

The methods used to prepare PEG-*b*-PLA and PEG-*b*-PCL micelles have been described elsewhere.[98] Briefly, 15 mg of PEG-*b*-PLA at M_n of PEG = 4,200 g/mol; M_n of PLA = 1,900 g/mol; and M_w/M_n = 1.06 (Advanced Polymer Materials Inc., Montreal, Canada) and 2.0 mg of PTX, 2.0 mg of 17-AAG, and 1.5 mg of RAPA (LC Laboratories, Woburn, MA) were dissolved in 0.5 mL of acetonitrile in a round bottom flask, followed by solvent evaporation under reduced pressure using a rotatory evaporator at 60 °C until a thin, even film was formed. The polymeric film was rehydrated with 0.5 mL double-distilled water or 0.9% saline. The aqueous solution was centrifuged for 5 min at 10,000 g to remove water insoluble drug and passed through 0.2 μm nylon syringe filter (National Scientific, Rockwood, TN).

PEG-*b*-PCL micelles were prepared by a distinct method: 4.0 mg of PEG-*b*-PCL at M_n = 5,000 g/mol; M_n of PCL = 10,000 g/mol; and Mw/Mn = 1.3 (Polymer Source, Dorval, Canada) and 0.10 mg of DiR (Caliper Life Science, Hopkinton, MA) were dissolved in 2.0 mL of acetone, followed by a rapid addition of 2.0 mL of double-distilled water or 0.9% saline with vigorous mixing. Acetone was allowed to evaporate from the aqueous micelle solution under stirring at room temperature for 40 min. The aqueous micelle solution was centrifuged for 5 min at 10,000 g to remove insoluble DiR and passed through 0.2 μm nylon syringe filter.

The content of PTX, 17-AAG, and RAPA in PEG-*b*-PLA micelles and content of DiR in PEG-*b*-PCL micelles was quantified by reverse-phase HPLC analysis, using a Shimadzu Prominence HPLC system (Shimadzu, Japan) equipped with an LC-20AT pump, a SIL-20AC

HT autosampler, a CTO-20AV oven, and an SPD-M20A diode array detector. Aqueous micelle solutions (10 μL) were injected into a Zorbax SB-C8 Rapid resolution cartridge (4.6 × 75 mm, 3.5 micron, Agilent). The flow rate was 1.0 mL/min, and column temperature was kept at 40 °C. The separation of PTX, 17-AAG and RAPA was done in isocratic mode with mobile phase consisting of 55% acetonitrile and 45% double-distilled water containing 0.1% phosphoric acid and 1% methanol. PTX, 17-AAG, and RAPA were monitored at 227, 333, and 279 nm and eluted at 2.8, 3.3, and 8.6 min, respectively. The elution of DiR was done in a gradient mode with the mobile phase consisting of 30% acetonitrile containing 0.03% trifluoroacetic acid as solvent A and 70% double-distilled water containing 0.07% trifluoroacetic acid as solvent B. Gradient elution was employed according to the following linear program: 0 min, 100% solvent A and 0% solvent B; 32 min, 30% solvent A and 70% solvent B. DiR was monitored at 745 nm and eluted at 16 min.

Z-average diameters of 3-in-1 PEG-*b*-PLA micelles and PEG-*b*-PCL micelles carrying DiR were determined by dynamic light scattering measurement using a Zetasizer Nano-ZS (Malvern Instruments, UK) at 25 °C with a detection angle of 173° and a He–Ne ion laser (λ = 633 nm) for the incident beam. The correlation function was curve-fitted by the cumulant method, and the z-average diameters of PEG-*b*-PLA and PEG-*b*-PCL micelles were obtained by single exponential algorithm. All measurements were repeated three times, and z-average diameter presented as an average ± standard deviation. The width of the distribution was estimated by polydispersity index (PDI).

3.2.2. LS180 human colon xenograft model

LS180 human colon carcinoma cells were cultivated in minimum essential medium (MEM) including Earle's salts (Cellgro, Manassas, VA), supplemented with 2% sodium bicarbonate, 1% non-essential amino acids, 1% sodium pyruvate, 10% fetal bovine serum, 1% L-glutamine, and 100 U/mL penicillin-streptomycin solution. Cells were maintained at 37 °C under an atmosphere of 5% CO_2 in a humidified incubator. Cells with > 90% viability were harvested from subconfluent cultures after trypsinization, and 1 x 10^6 cells were inoculated subcutaneously into the right flank of anesthetized female 6-8 week-old nude mice (Laboratory Animal Resources, Madison, WI). General anesthesia was induced with 1.5% isoflurane/oxygen, and anesthesia was maintained with 1% isoflurane/oxygen. When solid tumors reached 200-300 mm^3, mice were randomly divided into 3 groups (n = 3): 3-in-1 PEG-*b*-PLA micelles with PTX, 17-AAG, and RAPA at 60, 60, and 30 mg/kg, PEG-*b*-PLA micelles with PTX at 60 mg/kg; and empty PEG-*b*-PLA micelles as a control. Each treatment group was injected through the tail vein of anesthetized animals. Thereafter, tumor volumes and body weights were measured by a digital caliper (Fisher Scientific, Pittsburgh, PA) and a portable scale everyday for 6 days. In the mean time, behavior of animals was monitored. All animal experiments were approved by UW-Madison's institutional animal care and use committee.

3.2.3. Whole body NIR optical imaging

Two days after the primary injection of PEG-*b*-PLA micelles, PEG-*b*-PCL micelles carrying DiR (230 μg/kg) were injected through the tail vein of anesthetized animals. Whole-body images were recorded 10 min, 1, 2, 4, 6, 9, 12, 24, 48, 72, 96 hr, using Xenogen IVIS® 200 Series (Caliper Life Sciences, Hopkinton, MA). Mice were placed in lateral positions to obtain

whole-body optical images color-coded by the fluorescence of DiR, with the filter set at excitation and emission wavelengths of 745 and 800 nm, respectively. In this time course experiment, all images were collected using identical system settings, and the fluorescence emission of DiR was normalized by average radiant efficiency, total photons per second per square centimeter per steradian in the irradiance range (microwatts per square centimeter): [p/s/cm^2/sr]/[μW/cm^2]), using Living Imaging® software. For comparison, a region of interest (ROI) was outlined around the solid tumor region, and the fluorescence intensity of DiR associated with the tumor was measured. The tumor-to-whole body fluorescence intensity ratio for DiR was calculated to evaluate the selective accumulation of DiR incorporated in PEG-*b*-PCL micelles at solid tumors.

3.2.4. *Ex vivo* NIR optical imaging

After 4 days of whole body NIR optical imaging (6 days post primary injection), all animals were sacrificed by CO_2 asphyxia. A surgical midline incision was done with sterilized microsurgical instruments, and abdomen of animals was opened to simulate surgical tumor resection. Tumor, liver, lung, heart, spleen, kidneys and muscle tissues were excised and rinsed. ROIs were drawn around the tissues, and the tissue-to-muscle ratios were calculated to evaluate relative tissue accumulation of DiR.

3.2.5. Laser scanning confocal microscopy

Freshly isolated tissues were fixed with 4% paraformaldehyde in PBS at 4 °C and immersed in 30% sucrose in PBS solution for 1 hr. Tissue blocks were embedded and completely

covered by Tissue-Tek OCT compound (Sakura Finetek, Japan) in intermediate specimen cryomold (Sakura Finetek, Japan), and stored at -80 °C. Ten μm-thick sections were prepared using a cryotome cryostat and placed on superfrost microscope slides (Fisher Scientific, Pittsburgh, PA). A drop of mounting media (Thermo Fischer Scientific, Fremont, CA) was added on sections before placing a glass coverslip (Fisher Scientific, Pittsburgh, PA) on the slides. The nuclei of cells were stained by DAPI (Invitrogen, Carlsbad, CA). DAPI and DiR were visualized at 460 nm and 635 nm, respectively, using a laser scanning confocal microscope (Olympus FV1000 FLUOVIEW, Minneapolis, MN). Twenty tumor sections among 100 tumor sections were randomly selected and marked by different colored-tapes in each group. The operator who did not have knowledge of the identity of the slides conducted a blinded observation.

3.2.6. TUNEL assay

DNA fragmentation resulting from apoptosis in tumor, spleen and liver tissues was detected by TdT-mediated dUTP Nick-End Labeling method (TUNEL) using DeadEnd™ Fluorometric TUNEL assay kit (Promega, Madison, WI). Frozen tissue sections were permeabilized by proteinase K and fixed with 4% formaldehyde in PBS solution. The reaction mixture containing TdT and fluorescein-labeled dUTP was added to sectioned tissue and incubated for 60 min at 37 °C in the humidified chamber under the dark condition. Nuclei of cells were counterstained with DAPI. Fluorescein-labeled DNA fragments were visualized at 520 nm, and blue-colored nuclei stained by DAPI were visualized at 460 nm by using a laser scanning confocal microscope (Olympus FV1000 FLUOVIEW, Minneapolis, MN). The apoptotic index was determined as the number of green-colored DNA fragments (apoptotic cells)

in the area showing 100 blue-colored nuclei. This study was also conducted by blinded observation.

3.2.7. Statistical analysis

Statistical analysis was performed using one-way ANOVA at 5% significance level combined with Tukey's multiple comparison tests provided by GraphPad Prism version 5.00 for Mac OS X (San Diego, CA).

3.3. Results and discussion

3.3.1. Antitumor activity of 3-in-1 PEG-*b*-PLA micelles

After solid tumors reached 200-300 mm^3 in a LS180 human colon xenograft model, 3-in-1 PEG-*b*-PLA micelles carrying PTX/17-AAG/RAPA (60/60/30 mg/kg), PEG-*b*-PLA micelles carrying PTX (60 mg/kg), or empy PEG-*b*-PLA micelles as a vehicle control were injected intravenously, and tumor volume and body weight were measured daily for 6 days (Figure 3.2A). In the vehicle control, tumors gradually increased over 6 days, reaching *ca.* 580 mm^3. Similarly, tumors gradually increased over 6 days in the same way for PEG-*b*-PLA micelles carrying PTX, although at day 2, tumor volume for PTX appeared slightly smaller than the vehicle control. In contrast, a single IV injection of 3-in-1 PEG-*b*-PLA micelles reduced tumor volume by 1.6-fold, reaching *ca.* 100 mm^3. At the same time, body weights of mice treated with 3-in-1 PEG-*b*-PLA micelles declined slightly, but the decrease was < 10% with no deaths, suggesting acceptable acute toxicity (Figure 3.2B). Similar acute toxicity results were observed for the vehicle control and PEG-*b*-PLA micelles carrying PTX at 60 mg/kg. Other options for concurrent and sequential

deliveries of 3 drugs are injecting a mixture of 3 individual single drug-loaded micelles (3-in-3 micelles) and separately injecting the 3 corresponding micelles (3 x 1-in-1 micelles), respectively. However, the strategy of using 3-in-1 micelles would be more practical by minimizing injection volume compared to IV injections of 3 individual single drug-loaded micelles as the minimum injection volume for either 3-in-3 or 3 x 1-in-1 micelles would be beyond the volume limit for IV administration to mice (blood volume 1.2-1.6 mL). In summary, 3-in-1 PEG-*b*-PLA micelles exerted potent antitumor efficacy after a single IV injection, whereas PEG-*b*-PLA micelles carrying PTX at 60 mg/kg was no different than the vehicle control. These *in vivo* results were at odds with in vitro cell culture experiments, which showed that PTX is at least as potent as PTX/17-AAG/RAPA in terms of IC_{50} value (*ca.* 170 nM) against LS180 human colon cells, whereas 17-AAG and RAPA were ineffective (> 10,000 nM). We speculate that 17-AAG, a heat shock protein 90 (Hsp90) inhibitor, and RAPA, a mammalian target of rapamycin (mTOR), inhibitor act in concert with PTX on both tumor cells and tumor-associated stromal cells, whereas PTX acts primarily on tumor cells, limiting its antitumor response in an *in vivo* setting.

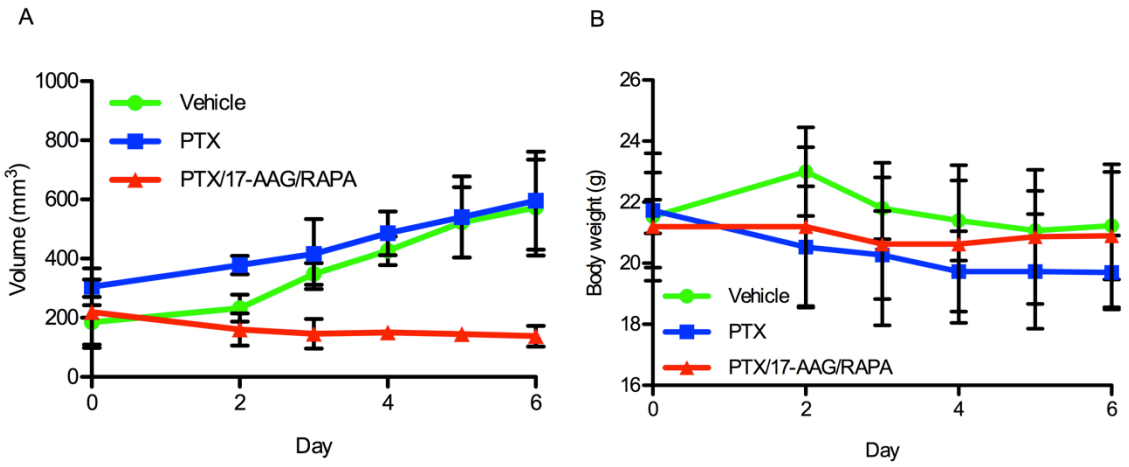

Figure 3.2. Effects of PEG-*b*-PLA micelles carrying PTX/17-AAG/RAPA, PTX, or vehicle control on (A) tumor growth and (B) body weight (mean ± SD; n = 3/treatment group).

3.3.2. Whole body NIR optical imaging

In a FaDu human hypopharyngeal carcinoma xenograft model, PTX as Taxol® injected IV at 40 mg/kg caused maximum apoptosis at solid tumors (> 10%) after 2 to 3 days.[18] For NIR optical imaging of solid tumors, PEG-*b*-PCL micelles carrying DiR (230 μg/kg) were injected intravenously 2 days after the primary IV injection of 3-in-1 PEG-*b*-PLA micelles carrying PTX/17-AAG/RAPA (60/60/30 mg/kg), PEG-*b*-PLA micelles carrying PTX (60 mg/kg), or empty PEG-*b*-PLA micelles. PEG-*b*-PCL micelles carrying DiR clearly delineated solid tumors based on whole-body optical imaging of DiR at 800 nm (Figure 3.3). The optical signal of DiR at solid tumors in mice clearly overlapped with solid tumors observed under white light. In all 3 test cases, the fluorescence signal intensity of DiR at solid tumors increased over 24 hr and had a high average radiant efficiency at in the region of interest (ROI), *i.e.* tumor (*ca.* 5 x 10^9 [p/s/cm^2/sr]/[μW/cm^2]), and high ratio of average radiant efficient at the ROI relative to whole

body (*ca.* 6 at 24 hr). The ROI-to-whole body ratios for DiR were not statistically different for the 3 test cases. In summary, whole-body NIR imaging of DiR in PEG-*b*-PCL micelles after IV injection showed preferential accumulation of DiR at solid tumors in a LS180 human colon xenograft model due to the EPR effect, owing to PEG-*b*-PCL micelles. However, whole-body NIR imaging was unable to distinguish tumor priming effects of 3-in-1 PEG-*b*-PLA micelles, although an obvious antitumor response was observed (Figures 3.2 and 3.3). We suspected that actual differences in fluorescence intensity of DiR of subcutaneously inoculated tumors were blurred under superficial skin layers, and we turned to *ex vivo* NIR optical imaging as a better surrogate of intraoperative NIR surgical guidance for tumor resection and to better ascertain the feasibility of 3-in-1 PEG-*b*-PLA micelles for tumor-primed NIR optical imaging.

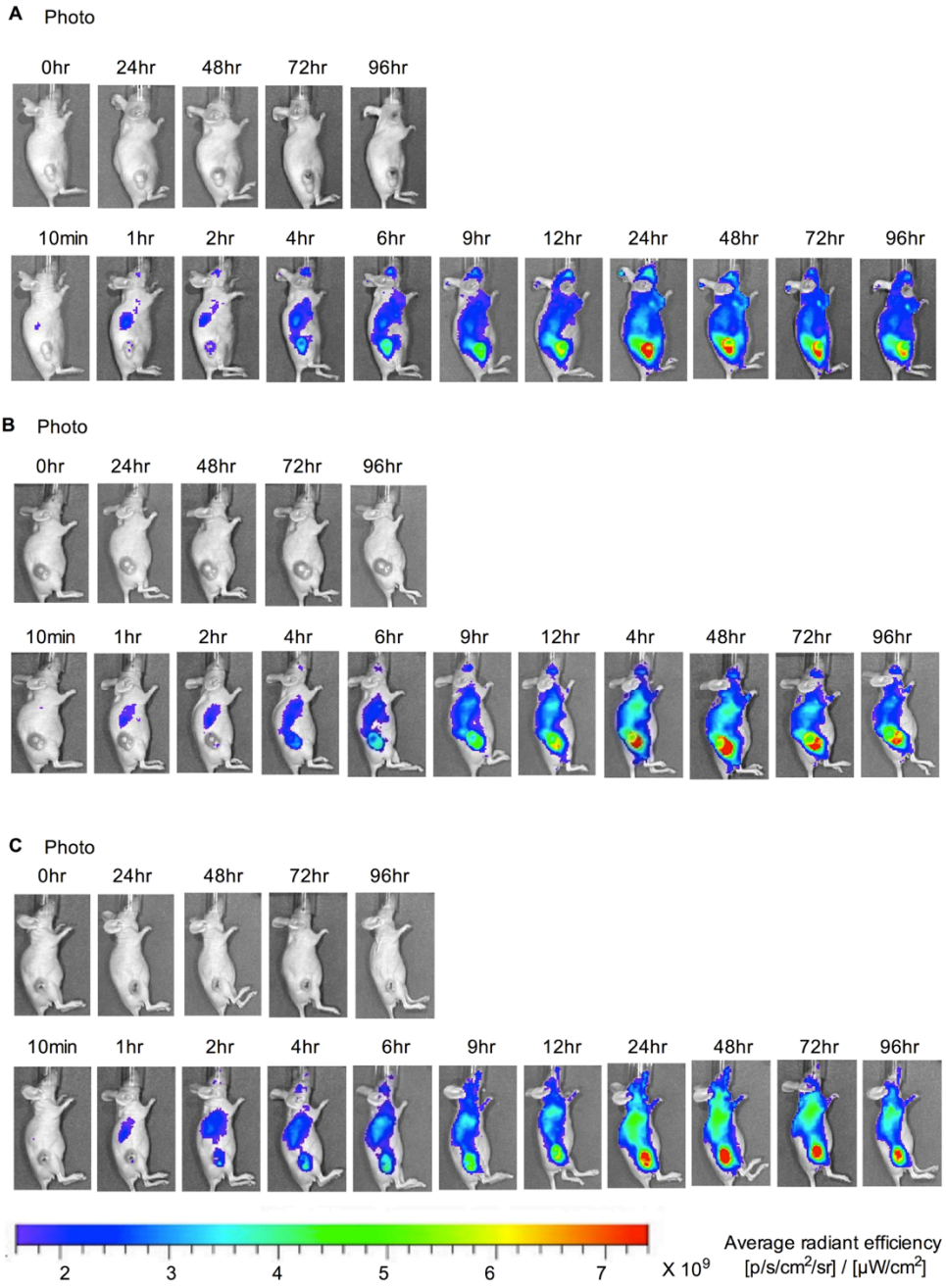

Figure 3.3. Whole-body NIR optical imaging of DiR. (A) Empty PEG-*b*-PLA micelles (vehicle), (B) PTX or (C) PTX/17-AAG/RAPA were injected IV 48 hr before the injection of DiR-containing PEG-*b*-PCL micelles.

3.3.3. *Ex vivo* NIR optical imaging

After 4 days of whole body NIR optical imaging (6 days post primary injection), mice were sacrificed by CO_2 asphyxia, and organs and tissues were surgically resected and subjected to *ex vivo* NIR optical imaging (Figure 3.4). Optical images of dissected tumors showed the highest level of fluorescence signal intensity of DiR, followed by the liver and spleen. kidneys, lungs, heart, and muscle had low fluorescence signal intensity for DiR, indicating a limited volume of distribution for DiR. In the color-coded fluorescence images of tumor tissue, noticeable differences between the 3 test cases were discerned: mice treated with a primary IV injection of 3-in-1 PEG-*b*-PLA micelles carrying PTX/17-AAG/RAPA displayed a red color, whereas mice treated with a vehicle control displayed a yellow color, *ca.* 1.3-fold reduction in fluorescence signal intensity (Figure 3.4). Tumor-to-muscle ratios are often used as a gauge of tumor selectivity in the evaluation of nanomaterials and were calculated for DiR based on *ex vivo* optical imaging (Figure 3.4B). The tumor-to-muscle ratio for mice treated with 3-in-1 PEG-*b*-PLA micelles carrying PTX/17-AAG/RAPA was 149±13, whereas the value for mice treated with PEG-*b*-PLA micelles carrying PTX was 118±10. The tumor-to-muscle ratio for vehicle control was 68±3. Thus, *ex vivo* NIR optical imaging revealed a 2.1- and 1.7-fold increase for the 2 pretreatment groups, respectively, suggestive of higher tumor levels of DiR. Notably, increases in tumor-to-muscle ratios for DiR were not accompanied by statistically higher values for other organs with the exception of the spleen for 3-in-1 PEG-*b*-PLA micelles (Figure 3.4B), suggesting selectivity in tumor priming for NIR optical imaging.

Additional evidence for the enhanced uptake of DiR at solid tumors was obtained from resected tumor tissue, which was collected, fixed with 4% paraformaldehyde, sectioned into 10

μm slices, and visualized by laser scanning confocal microscopy (Figure 3.5A). In this study, DiR was readily observed as red dots in resected tumors for mice pre-treated with 3-in-1 PEG-*b*-PLA micelles. A few red dots were also observed for the PTX group, whereas there were faint signs of DiR for the vehicle control. One limitation of this study was the use of a laser filter set at 635 nm, which is non-optimal for DiR. Still, these qualitative results from resected tumor tissue support the *ex vivo* NIR optical results, which suggest an enhanced tumor accumulation of DiR, particularly after tumor priming with 3-in-1 PEG-*b*-PLA micelles. Finally, apoptosis at solid tumors, spleen, and liver was assessed by the TUNEL method (Figure 3.5B). Apoptotic cells (in green) were clearly visible in solid tumors with 3-in-1 PEG-*b*-PLA micelles. Importantly, apoptotic cells were not visible at the liver and spleen. Here, the apoptotic index, *i.e.* apoptotic bodies in an area having 100 nuclei (stained in blue), was 15±0.22 for 3-in-1 PEG-*b*-PLA micelles and 3±1.02 for the PTX group. It was quite remarkable that apoptosis at solid tumors was evident after 6 days following a single IV injection of 3-in-1 PEG-*b*-PLA micelles, but is consistent with the reduction in tumor volume at day 6, *ca.* 100 mm^3 *vs.* 580 mm^3 for the PTX group (Figure 3.5).

While the mechanisms behind the enhanced uptake of DiR and high NIR optical signal at solid tumors remain to be fully elucidated, tumor-associated apoptosis was evident and clearly a factor in tumor priming. Au and coworkers proposed that PTX as Taxol® injected IV at 40 mg/kg reduced tumor cell density, expanded microvessel diameter, and promoted tumor perfusion.[18] It is noted that tumor priming with PTX as Taxol® in a FaDu human hypopharyngeal carcinoma xenograft model was tumor-selective, resulting in enhanced accumulation of liposomes that contain doxorubicin at solid tumors, but not at other organs, consistent with our *ex vivo* NIR

optical imaging results on DiR, delivered by PEG-*b*-PCL micelles. Other possible mechanisms behind the enhanced uptake of DiR and high NIR optical signal at solid tumors may also include reduced interstitial tumor fluid pressure and vascular normalization as proposed by Jain, noting that PTX, 17-AAG, and RAPA all have anti-angiogenesis activity.

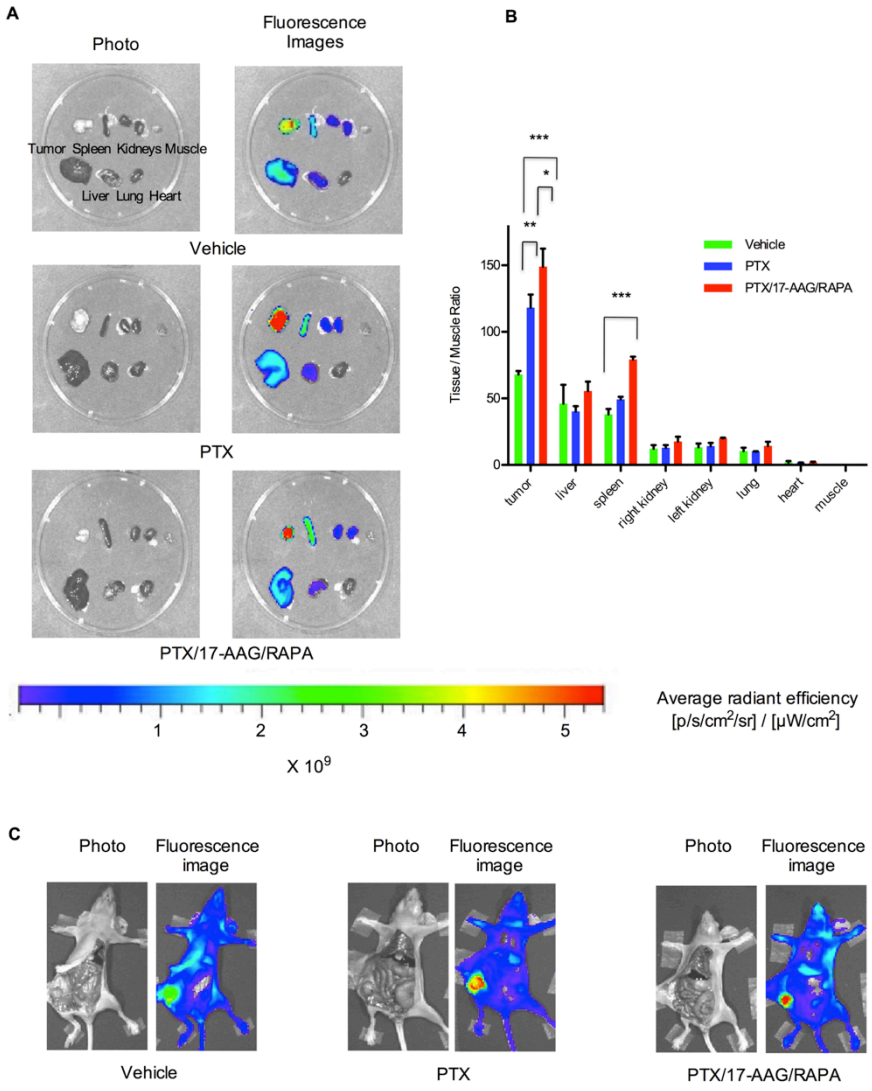

Figure 3.4. (A,B) *Ex vivo* NIR optical imaging of DiR after treatment with empty PEG-*b*-PLA micelles (vehicle), PTX, or PTX/17-AAG/RAPA, injected IV 48 hr before the injection of DiR-containing PEG-*b*-PCL micelles (mean

± SD; *n* = 3/treatment group; * < 0.05, ** < 0.01, *** < 0.0001). (C) Whole-body NIR optical images of DiR (solid tumors in the right flank) after a midline incision in the abdomen.

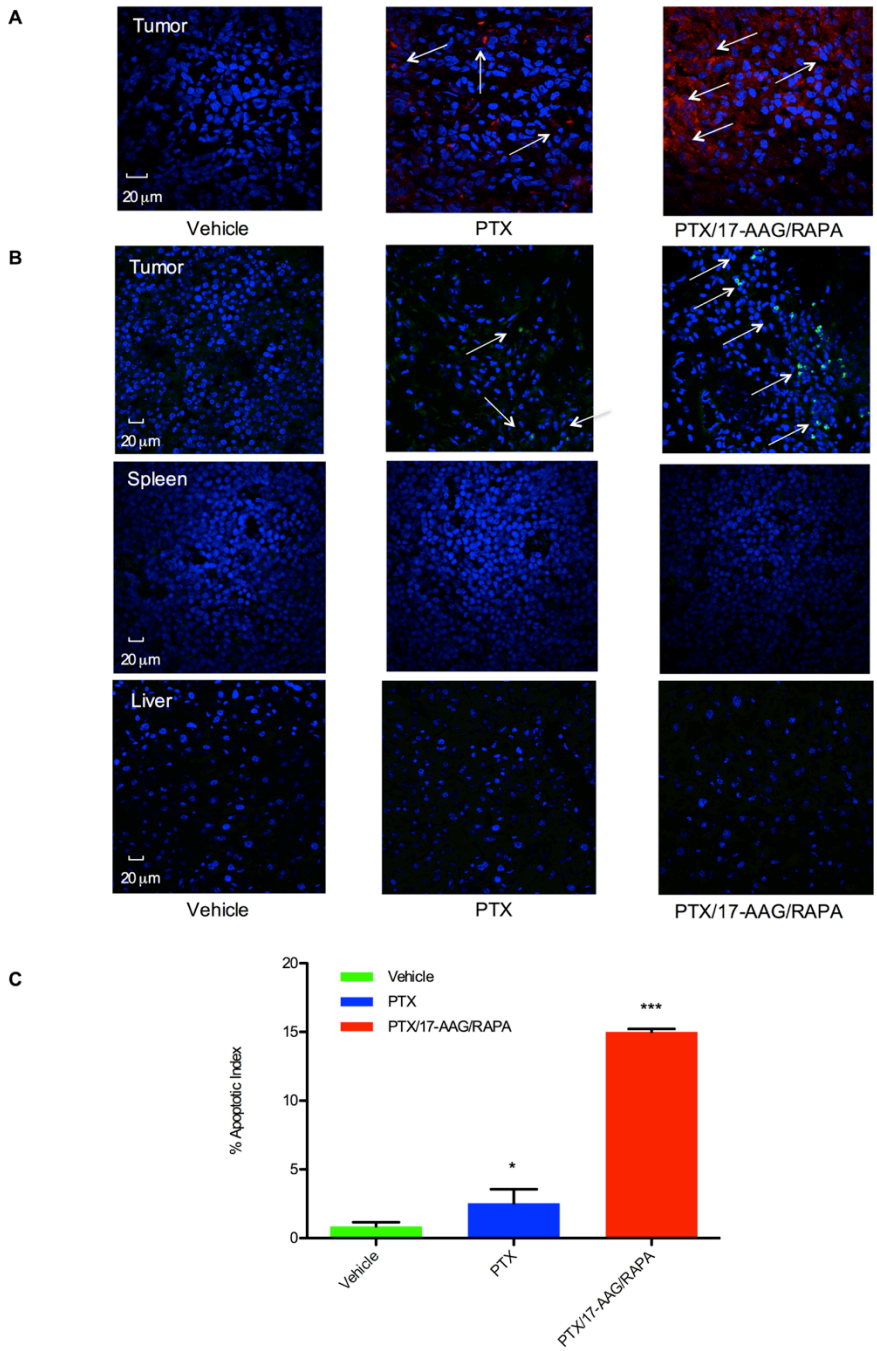

Figure 3.5. (A) Laser scanning confocal microscopy images of tumor tissue (60x magnification). DiR is read, and nuclei of cells are in blue (DAPI). (B) Immunohistochemical analysis of apoptosis by TUNEL in tumor, spleen, and liver tissue (40x magnification). Apoptotic cells are in green, and nuclei of all cells are in blue (DAPI). (C) Apoptosis index (mean ± SD; n = 3/treatment group; * < 0.05, *** < 0.0001).

3.4. Conclusion

NIR optical imaging has unique potential for intraoperative surgical guidance in oncology, beyond simple visualization with white light illumination, palpation, and experience, which is a major factor in surgical oncology. In a LS180 human colon xenograft model, 3-in-1 PEG-*b*-PLA micelles carrying PTX/17-AAG/RAPA induced apoptosis at solid tumors and elicited a striking 1.6-fold reduction in tumor volume after a single IV injection with low acute toxicity. Hence, 3-in-1 PEG-*b*-PLA micelles promoted the delivery of PEG-*b*-PCL micelles carrying DiR into solid tumors, resulting in heightened NIR optical signal for better tumor delineation. This "priming effect" was largely selective for solid tumors, achieving a remarkable tumor-to-muscle ratio of 149±13 for DiR in resected tissue. Thus, a tandem of 3-in-1 PEG-*b*-PLA and PEG-*b*-PCL micelles carrying DiR was used for effective tumor debulking, heightened tumor priming, and enhanced NIR optical imaging of solid tumors. It is noted that neoadjuvant therapy is commonly used for the debulking of solid tumor prior to surgical procedures. Therefore, there is a clinical potential of 3-in-1 PEG-*b*-PLA and PEG-*b*-PCL micelles for intraoperative surgical guidance in human xenograft models, assessing neoadjuvant chemotherapy and NIR optically-guided surgery on the effectiveness of surgical resection of tumors and ultimately survival. Beyond enhanced NIR optical imaging of solid tumors, tumor priming by 3-in-1 PEG-*b*-PLA micelles carrying PTX/17-AAG/RAPA merits consideration for the tumor targeting of nanomedicines in multimodal interventions in cancer therapy.

4 Polymeric Micelles for Neoadjuvant Chemotherapy Before Debulking Surgery in Intraperitoneal Xenograft Model of Ovarian Cancer

This chapter has been published in full: Cho H.; Lai T. C.; Kwon, G. S., Poly(ethylene glycol)-*block*-poly(ε-caprolactone) micelles for combination drug delivery: Evaluation of paclitaxel, cyclopamine and gossypol in intraperitoneal xenograft models of ovarian cancer. *J. Controlled Release* **2013**, *166* (1), 1-9.

4.1. Introduction

Ovarian cancer is the most lethal female gynecological malignancy. The estimated death of ovarian cancer patients in 2011 was 6% based on US mortality data. From 1999 to 2006, localized, regional, and distant ovarian cancers were diagnosed at 15%, 17%, and 62%, respectively, in the United States, and the overall 5-year survival rates for ovarian cancer stand at 94% for localized, 73% for regional, and 28% for distant ovarian cancers.[100] Most ovarian tumors initially respond to conventional cytotoxic agents, such as taxane and platinum analogues. However, ovarian cancer that relapses after first-line treatment presents reduced response to cytotoxic agents and eventually recurs as a more aggressive disease.[101]

Current treatment strategies for ovarian cancer in preclinical and clinical studies involve novel drug combinations that seek to overcome drug resistance of cytotoxic agents by targeting cancer cell survival signaling pathways with molecular targeted agents. For example, the hedgehog (Hh) pathway is activated in several malignancies and cancer stem cells, and it has recently been shown that the inhibition of Hh signaling results in reduced growth of ovarian cancer spheroid-forming cells: 10-, 5-, and 4-fold reduction in growth for ES-2, SKOV-3, and TOV112D cells, respectively.[102] Inhibition of Hh signaling in ovarian cancer has recently been shown to reverse taxane resistance in several cell lines by what appears to be a reduction in p-glycoprotein expression (multidrug resistance protein 1, MDR1).[103] In another cancer cell survival pathway, overexpression of anti-apoptotic Bcl-2 proteins is a common hallmark of many malignancies, and acquired cisplatin resistance in ovarian cancer cells has been linked to Bcl-2 overexpression.[104] Not surprisingly, interest in drug combinations of targeted agents with different mechanisms of action along with cytotoxic agents has developed, given tumor

heterogeneity and redundancy in cancer cell signaling, with the caveat that dose-limiting toxicity is not overlapping.

At the same time, progress has been made in drug delivery strategies for the treatment of ovarian cancer, relying mostly on the intraperitoneal (IP) route.[105] Metastasis of ovarian cancer proceeds primarily *via* the peritoneal cavity, as opposed to the vascular system for other malignancies.[106] Thus, IP injection or infusion of cytotoxic agents enables direct access to ovarian cancer, reduced systemic exposure, and increased overall survival relative to intravenous injection of cytotoxic agents. More recently, De Souza *et al.* have shown in xenograft models that an IP, sustained release or continuous exposure of docetaxel reduces tumor mRNA-expression of genes encoding drug efflux transporters, *e.g.* MDR1.[107] Lastly, Au and co-workers have championed the strategy of "tumor priming" for bulky peritoneal tumors and shown that apoptosis induction by paclitaxel (PTX) may promote tumor penetration of drugs, drug-containing nanoparticles, and drug-containing microparticles, overcoming barriers to transport in tumor interstitium and drug resistance owing to inadequate drug delivery.[108]

Here, we show that poly(ethylene glycol)-*block*-poly(ε-caprolactone) (PEG-*b*-PCL) micelles have a carrying capacity for PTX, cyclopamine (CYP), and gossypol (GSP) (Figure 4.1). CYP antagonizes the Hh pathway by directly binding to Smoothened in a Patched-independent manner.[109] GSP is a polyphenolic pro-apoptotic compound, inhibiting anti-apoptotic proteins (Bcl-2, Bcl-x_L, and Mcl-1).[110, 111] All three anticancer agents are poorly water-soluble, and PEG-*b*-PCL micelles can deliver all three together following multiple drug solubilization, enabling *in vivo* toxicity and efficacy studies in xenograft models. Our results corroborate studies on 3-drug poly(ethylene glycol)-*block*-poly(*d,l*-lactic acid) micelles, which also had a capacity for multiple

drug solubilization. Tail vein injection of 3-drug poly(ethylene glycol)-*block*-poly(*d*,*l*-lactic acid) micelles resulted in robust antitumor responses in breast and lung cancer xenograft models.[31] In this chapter, we evaluated for the first time antitumor responses after IP injection of PEG-*b*-PCL micelles containing PTX, CYP, and GSP in ES-2 and SKOV-3 xenograft models, assessing tumor burden by noninvasive optical bioluminescence imaging, micro-positron emission tomography/computed tomography (microPET/CT) imaging, and overall survival. Our results suggest that IP delivery of polymeric micelles carrying multiple anticancer agents is a highly promising treatment strategy for ovarian cancer, benefiting from novel drug combinations that act on drug resistance pathways and also regional and sustained drug release for enhanced intratumoral drug delivery.

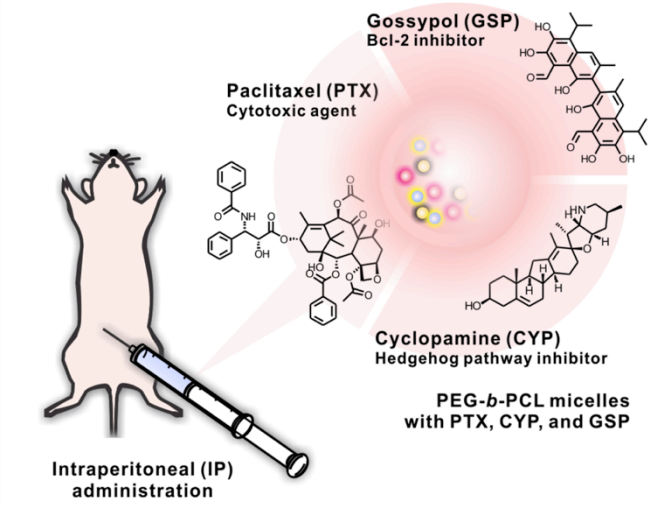

Figure 4.1. 3-drug PEG-*b*-PCL micelles with PTX, CYP, and GSP, injected IP in ovarian xenograft models.

4.2. Materials and methods

4.2.1. Preparation and characterization of drug-loaded PEG-*b*-PCL micelles

Drug-loaded PEG-*b*-PCL micelles were prepared by a solvent evaporation technique as previously described.[112] Briefly, 6.0 mg of PTX (LC Laboratories, Woburn, MA), CYP (Logan Natural Products, Plano, TX), and GSP (LKT Laboratories, Inc., St. Paul, MN) each and 180 mg of PEG-*b*-PCL (M_n of PEG = 5,000 g/mol; M_n of PCL = 10,000 g/mol; and M_w/M_n = 1.3, Polymer Source, Dorval, Canada) were dissolved in 1.0 mL of acetone, followed by a rapid addition of 1.0 mL of pre-warmed 0.9% saline or PBS (10 mM, pH 7.4) at 60 °C with vigorous mixing. Acetone was evaporated under reduced pressure using a rotatory evaporator at 60 °C. Insoluble drugs were removed by centrifugation for 5 min at 10,000 g, followed by filtration with 0.2 μm nylon syringe filters. The content of PTX, CYP, and GSP in PEG-*b*-PCL micelles was quantified by reverse-phase HPLC (RP-HPLC) analysis with a Shimadzu Prominence HPLC system (Shimadzu, Japan). Samples (10 μL) were injected into a Zorbax SB-C_8 rapid resolution cartridge (4.6 mm x 75 mm, 3.5 mm, Agilent). The flow rate was 1.0 mL/min, and the column was kept at 40 °C. The separation of PTX, CYP, and GSP was done in an isocratic mode with mobile phase consisting of 55% of acetonitrile, 45% distilled water, and 0.1% trifluoroacetic acid. PTX, CYP, and GSP were monitored at 227, 204, and 373 nm, respectively, and eluted at 2.7 min, 1.9 min, and 10.6 min, respectively.

Z-average diameters of PEG-*b*-PCL micelles at 25 °C were determined by dynamic light scattering (DLS) measurements using a Zetasizer Nano-ZS (Malvern Instruments, UK) at a fixed angle of 173°. Autocorrelation functions were treated by cumulant analysis, calculating the hydrodynamic diameter of PEG-*b*-PCL micelles from the Stokes-Einstein equation and the

polydispersity index (PDI). Prior to measurements, PEG-*b*-PCL micelle solutions were diluted 10 times with 0.9% saline or PBS (10 mM, pH 7.4), resulting in the level of PEG-*b*-PCL at 1.8 mg/mL (above the critical micelle concentration).

The physical stability and drug release kinetics of drug-loaded PEG-*b*-PCL micelles were studied *in vitro*. An aqueous solution of drug-loaded PEG-*b*-PCL micelles (6.0 mg/mL of each drug) was incubated at 25 °C for 24 hr and centrifuged for 5 min at 10,000 g, followed by filtration using 0.22 mm nylon syringe filters to remove any precipitated drug. The level of drug remaining in solution after 24 hr was quantified by RP-HPLC analysis as described above, and the % remaining drug in solution was calculated. In *in vitro* drug release experiments, an aqueous solution of drug-loaded PEG-*b*-PCL micelles (0.6 mg/mL of each drug) was put into dialysis cassettes (MWCO 20,000, Thermo Fisher Scientific Inc., Rockford, IL), and cassettes were placed in 2.0 L of PBS (10 mM, pH 7.4) at 37 °C with stirring. Samples (20 μL) were withdrawn, and cassettes were replenished with 20 μL of fresh PBS. Withdrawn samples at various time points, 0, 0.5, 1, 2, 3, 6, 15, 18, 24, 48, and 72 hr, were analyzed by RP-HPLC to quantify the level of drug left in the dialysis cassette. Assuming that drug release from PEG-*b*-PCL micelles was rate-limiting, % drug release was calculated over time, and curve-fitting and estimation of time for 50% drug release ($t_{1/2}$) were done based on a two-phase exponential association model using GraphPad Prism version 5.00 for Mac OS X (San Diego, CA).

4.2.2. Luciferase-expressing ES-2 and SKOV-3 cells (ES-2-luc and SKOV-3-luc)

ES-2 and SKOV-3 human ovarian cancer cell lines (ATCC, Manassas, VA) were cultured in McCoy's 5a medium and RPMI-1640 medium, respectively, supplemented with 1%

L-glutamine, 10% fetal bovine serum, and 1% penicillin/streptomycin. ES-2 and SKOV-3 cells were maintained at 37 °C under an atmosphere of 5% CO_2 in a humidified incubator. Both ovarian cancer cell lines were stably transfected with luciferase-expressing plasmid pGL4.51 containing the neomycin-resistance gene (Promega, Madison, WI) using Lipofectamine 2000™ (Invitrogen, Carlsbad, CA) according to the manufacturer's protocol. After 48 hr, ES-2 or SKOV-3 cells were cultured in corresponding medium containing 750 μg/mL G418 selective antibiotics for 3 to 4 weeks until cell foci were obtained. Several G418-resistant clones were isolated and maintained in G418-containing medium at 500 μg/mL. Luciferase expression for expanded clones was quantified using a luciferase assay system kit (Promega, Madison, WI). The clone with the highest luciferase expression for each cell line was chosen for subsequent *in vitro* and *in vivo* experiments.

4.2.3. *In vitro* cytoxicity study

In vitro cytotoxicity of drug-loaded PEG-*b*-PCL micelles was assessed in 2-D cell culture with luciferase-expressing ES-2-luc and SKOV-3-luc cells and with 3-D tumor spheroids formed from ES-2-luc cells. SKOV-3-luc (10,000 cells/well) and ES-2-luc (5,000 cells/ well) were seeded in 96-well plates and incubated for 24 hr to form 2-D monolayers. ES-2-luc cells (1,000 cells/well) were suspended in agarose-coated 96-well plates and incubated for 4 days to generate 3-D tumor spheroids.[113] Drug-loaded PEG-*b*-PCL micelles were added at final drug concentrations of 0.1, 1, 10, 100, and 1000 nM, and cell viability was determined 72 hr post drug treatment by quantifying the intensity of bioluminescence signal expressed in surviving cells using Xenogen IVIS® 200 Series (Caliper Life Science, Hopkinton, MA). D-luciferin (Caliper

Life Science, Hopkinton, MA) at 15 mg/well was added to 96-well plates 5 min prior to bioluminescence imaging. The half maximal inhibitory drug concentration (IC_{50}) was determined with the median effect equation provided by GraphPad Prism. The morphology of ES-2-luc tumor spheroids 3 days post drug treatment was observed by an inverted light microscope (Nikon, Japan).

4.2.4. Human ovarian cancer xenografts and drug treatment

Female 6-8 week-old athymic nude-Foxn1^{nu} mice were purchased from Harlan Laboratories (Madison, WI). General anesthesia was induced with 1.5% isoflurane/oxygen and maintained with 1% isoflurane/oxygen. All animal experiments were approved by UW-Madison's Institutional Animal Care and Use Committee and conducted in accordance with institutional and NIH guidance. ES-2-luc and SKOV-3-luc cells were harvested from sub-confluent cultures after trypsinization, and ES-2-luc (1 x 10^6 cells/animal) and SKOV-3-luc (2 x 10^6 cells/animal) cells were injected (approximately 100 μL) IP into anesthetized mice. Drug treatment was initiated 4 days and 16 days post cell inoculation of ES-2-luc cells and SK-OV-3-luc cells, respectively, after observation of bioluminescence in whole-body images of animals by Xenogen IVIS® 200 Series. Both ES-2-luc-bearing and SKOV-3-luc-bearing xenografts were divided into 3 groups (n = 4): 3-drug PEG-*b*-PCL micelles with PTX, CYP, and GSP at 30, 30, and 30 mg/kg; PEG-*b*-PCL micelles with paclitaxel at 30 mg/kg; and empty PEG-*b*-PCL micelles as a control. Each (approximately 200 μL) was injected IP into anesthetized nude mice q7d x 3 (days 0, 7, and 14). Body weights and radii of abdomen of mice were recorded up to 2 months by a portable scale and a digital caliper (Fisher Scientific, Pittsburgh, PA), respectively.

All mice used for treatment response evaluations were euthanized at the time of reaching a moribund condition, and Kaplan-Meier survival curves were constructed.

4.2.5. Whole-body bioluminescence imaging

Animals were anesthetized as described above. All mice were imaged using a cooled CCD camera (Xenogen IVIS® 200 Series), using Live Imaging® software for image acquisition and analysis (Caliper Life Science, Hopkinton, MA). Color-coded whole-body images were recorded on days 0, 4, 7, 8, 11, 14, 17, 21, and 35 after the first treatment to measure the dynamics of peritoneal tumor growth. In these experiments, all images were acquired and collected using identical system settings: exposure time = 1 sec; binning = medium; f/stop 2 for ES-2-luc-bearing animals and exposure time = 10 sec; binning = medium; f/stop 2 for SKOV-3-luc-bearing animals. D-luciferin (Caliper Life Science, Hopkinton, MA) at 113 mg/kg was injected IP into ES-2-luc-bearing and SKOV-3-luc-bearing mice 5 and 20 min, respectively, prior to whole-body imaging. Live Imaging® software was used to quantify the total photon counts of bioluminescence from ES-2-luc-bearing or SKOV-3-luc cells in the regions of interest (ROIs), which was selected manually over IP tumors.

4.2.6. Whole-body microPET/CT imaging

The proliferation of ES-2-luc cells was noninvasively monitored *in vivo*, using an Inveon microPET/CT hybrid scanner (Siemens, Knoxvile, TN). 3'-deoxy-3'-^{18}F-fluorothymidine (^{18}F-FLT) was purchased from the University of Wisconsin Cyclotron Research Center (Madison, WI). Animals were intraocularly (IO) injected with 107 ± 10 mCi of ^{18}F-FLT on days 0, 7, and

17 after the first treatment. One hour after injection, mice were prepared for dual hybrid microPET/CT imaging; microPET acquisition was performed immediately, followed by microCT acquisition. Maximum intensity projections were created using a Siemens Inveon Research Workplace (Knoxville, TN); PET images were reconstructed using OSEM3D/MAP. MicroCT images were also reconstructed using standard conebeam reconstruction. Both microPET and microCT images were fused in Siemens Inveon Software. ROIs were manually drawn on CT pictures around the region with highest signal intensity in the IP cavity, and tumor volume and ^{18}F-FLT uptake, assessed by standard uptake value (SUV) mean, were calculated by the estimation of voxels within tomographic planes. The relative SUV (% SUV) was calculated by comparing the SUV mean at each time point to the initial SUV mean on day 0.

4.2.7. Statistical analysis

Data were represented as mean ± standard deviation (SD). Statistical analysis was conducted using one-way ANOVA at 5% significance level combined with Tukey's multiple comparison tests provided by GraphPad Prism. (*), (**), and (***) signify $p < 0.05$, $p < 0.01$, and $p < 0.001$, respectively.

4.3. Results

4.3.1. Characterization of drug-loaded PEG-*b*-PCL micelles

Table 4.1 presents the level of PTX, CYP, and GSP in 0.9% saline (mg/mL) and loading efficiency (weight drug/weight polymer), achieved after loading in PEG-*b*-PCL micelles by a solvent evaporation technique. PEG-*b*-PCL micelles had z-average diameter of 80-90 nm and

PDI < 0.1 regardless of drug loading. The maximum loading efficiency of PTX, CYP, and GSP in PEG-*b*-PCL micelles was *ca*. 2, 1, and 1%, respectively. Similarly, 2-drug PEG-*b*-PCL micelles had low loading efficacy (Table 4.1). In both cases at 200 mg/mL of PEG-*b*-PCL micelles, however, aqueous drug solubility was 0.9 to 3.8 mg/mL, which is enough to enable *in vivo* treatment studies. Interestingly, 3-drug PEG-*b*-PCL micelles had the highest drug loading efficiency, *ca*. 9.4%, achieving water solubility for PTX, CYP, and GSP at *ca*. 6 mg/mL of each drug for a total water solubility of 18 mg/mL.

After 24 hr at 25 °C, single drug PEG-*b*-PCL micelles retained CYP and GSP, *ca*. 96 and 89%, respectively, whereas PEG-*b*-PCL micelles retained 34% of PTX, indicating poor physical stability (Table 4.2). Not surprisingly, 2-drug PEG-*b*-PCL micelles also poorly retained PTX, and PEG-*b*-PCL micelles containing CYP and GSP were stable, *ca*. 91 and 90%, respectively. 3-drug PEG-*b*-PCL micelles showed anomalous stability, retaining PTX, CYP, and GSP at ca. 99%, 37%, and 82%, respectively. A similar relative pattern of *in vitro* drug release for 3-drug PEG-*b*-PCL micelles was observed (Figure 4.2). All three drugs were released from PEG-*b*-PCL micelles over 72 hr in a biphasic pattern, and the individual release curves were fit to a two-phase exponential association model with the goodness of fit of 0.98 (PTX), 1.00 (CYP), and 0.99 (GSP) (Figure 4.2). The $t_{1/2}$ values of PTX, CYP, and GSP for PEG-*b*-PCL micelles were 50, 18, and 30 hr, respectively. Drug release curves reached a plateau at 60, 93, and 67% for PTX, CYP, and GSP, respectively, within 72 hr.

Micelles	Polymer (mg/mL)	PTX (mg/mL)	CYP (mg/mL)	GSP (mg/mL)	Loading efficiency (%)
	200	3.8 ± 0.6	-	-	2.0 ± 0.3
1-in-1	200	-	1.2 ± 0.1	-	0.6 ± 0.1
	200	-	-	2.3 ± 0.5	1.2 ± 0.5
	200	3.6 ± 0.4		2.7 ± 0.5	3.1 ± 0.5
2-in-1	200	2.8 ± 0.2	0.9 ± 0.0		1.8 ± 0.1
	200		3.2 ± 1.0	3.2 ± 1.0	3.2 ± 0.6
3-in-1	200	6.3 ± 0.5	6.2 ± 0.5	6.2 ± 0.5	9.4 ± 0.8

Table 4.1. Combination drug solubilization by PEG-*b*-PCL micelles.

Micelles	Drugs	% w/w Remaining		Z-average size distribution (nm)	
		0 hr	24 hr	0 hr	24 hr
1-in-1	PTX	100.0 ± 9.3	34.3 ± 3.1	83.1 ± 1.0	79.5 ± 1.3
	CYP	100.0 ± 10.6	96.3 ± 5.0	79.2 ± 0.3	76.3 ± 0.9
	GSP	100.0 ± 4.7	89.4 ± 3.3	79.0 ± 0.2	76.5 ± 0.9
2-in-1	PTX	100.0 ± 12.6	27.0 ± 2.9	88.7 ± 0.7	82.2 ± 1.9
	CYP	100.0 ± 11.3	97.4 ± 5.7		
	PTX	100.0 ± 9.4	66.8 ± 4.1	80.7 ± 0.5	76.4 ± 0.5
	GSP	100.0 ± 4.4	97.0 ± 2.5		
	CYP	100.0 ± 8.2	91.0 ± 5.3	80.1 ± 0.6	76.6 ± 1.6
	GSP	100.0 ± 4.9	89.8 ± 3.7		
3-in-1	PTX	100.0 ± 4.7	99.3 ± 2.2		
	CYP	100.0 ± 6.1	36.8 ± 1.5	77.2 ± 0.7	73.4 ± 0.3
	GSP	100.0 ± 3.8	82.3 ± 2.6		

Table 4.2. Physical stability of multi-drug loaded PEG-*b*-PCL micelles after 24 hr at 25°C.

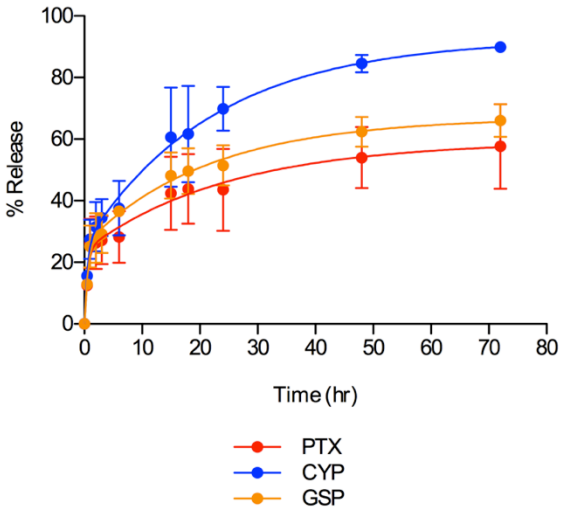

Figure 4.2. *In vitro* drug release kinetics of PTX, CYP, and GSP from PEG-*b*-PCL micelles.

4.3.2. *In vitro* cytotoxicity study

In 2-D and 3-D cell culture, PEG-*b*-PCL micelles containing PTX had the highest *in vitro* cytotoxicity against ES-2-luc and SKOV-3-luc cells based on a loss of bioluminescence signal upon drug treatment (Table 4.3). CYP was also relatively active against luciferase-expressing ES-2-luc having IC_{50} values in 2-D and 3-D cell culture at 234 and 65 nM, respectively, whereas it was much less active against SKOV-3-luc cells, IC_{50} > 100,000 nM. GSP as a single agent was the least active. Accordingly, 2-drug PEG-*b*-PCL micelles containing PTX/CYP and PTX/GSP were relatively active against ES-2-luc and SKOV-3-luc cells, whereas 2-drug PEG-*b*-PCL micelles containing CYP/GSP were largely ineffective. The IC_{50} of 3-drug PEG-*b*-PCL micelles was 51, 101, and 67 nM for ES-2-luc (2-D), ES-2-luc (3-D), and SKOV-3-luc (2-D), respectively. Morphologies of ES-2-luc tumor spheroids upon drug treatment at 1 mM were largely consistent with IC_{50} values for ES-2-luc cells in 3-D cell culture (Figure 4.3): PTX had

the greatest impact on the growth of ES-2-luc tumor spheroids, followed by CYP; GSP did not appear to restrict the growth of ES-2-luc tumor spheroids. In all, single drug and 2-drug treatments, ES-2-luc tumor spheroids retained a spherical morphology. In contrast, ES-2-luc tumor spheroids lost their integrity after treatment with 3-drug PEG-*b*-PCL micelles, appearing to disaggregate into smaller cellular aggregates that lack a defined morphology (Figure 4.3).

Cells (condition)	PTX (nM)	CYP (nM)	GSP (nM)	PTX/CYP (nM) (1:2 M ratio)	CYP/GSP (nM) (1:1)	GSP/PTX (nM) (2:1)	PTX/CYP/ GSP (nM) (1:2:2)
ES-2 (2D)	12 ± 5	240 ± 54	>100,000	27 ± 4	18,790 ± 4119	40 ± 15	51 ± 18
ES-2 (3D)	9 ± 3	65 ± 10	4823 ± 1521	62 ± 14	2550 ± 920	108 ± 22	101 ± 21
SKOV-3 (2D)	98 ± 15	> 100,000	> 100,000	58 ± 11	> 100,000	67 ± 11	67 ± 35

Table 4.3. IC_{50} values of PTX, CYP, and GSP against 2-D- and 3-D-ES-2-luc- and 2-D-SKOV-3-luc cells based on bioluminescence imaging.

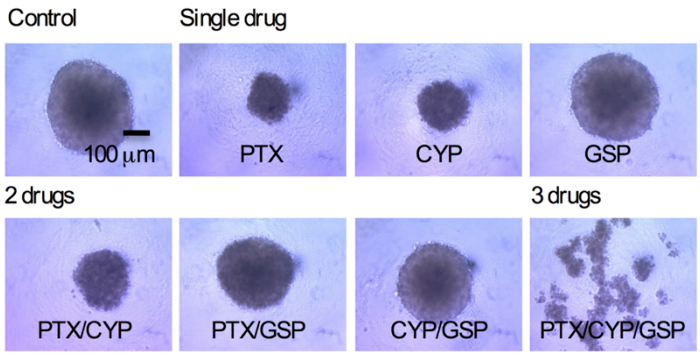

Figure 4.3. Morphologies of ES-2-luc spheroids 3 days post treatment: vehicle (control), single drug, 2-drug, and 3-drug. ES-2-luc spheroids were treated with 1 μM of total drug(s) for each formulation.

4.3.3. Anticancer efficacy of 3-drug PEG-*b*-PCL micelles after IP injection

The acute toxicity of 3-drug PEG-*b*-PCL micelles was assessed in female 6-8 week-old athymic nude-Foxn1^{nu} mice, following IP injection (q7d x 3), monitoring body weight, general appearance, and mortality. 3-drug PEG-*b*-PCL micelles at 30/30/30 mg/kg and PEG-*b*-PCL micelles containing only PTX at 50 mg/kg were well tolerated in a q7d x 3 schedule over 40 days (Figure 4.4).

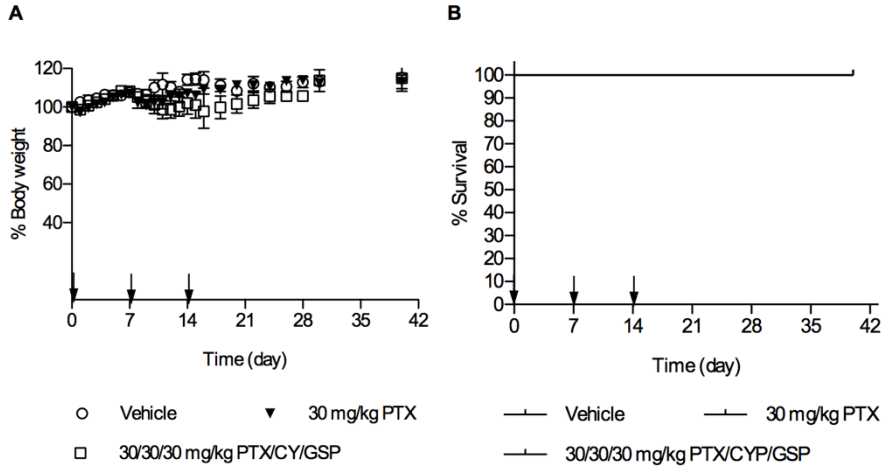

Figure 4.4. (A) Body weight change and (B) Kaplan-Meier analysis for survival of healthy athymic nude mice receiving IP treatment of vehicle, 3-drug PEG-*b*-PCL micelles at 30, 30, and 30 mg/kg, or PEG-*b*-PCL micelles containing PTX at 30 mg/kg on a q7d x 3 schedule were presented.

Peritoneal dissemination of ES-2-luc cells was observed longitudinally in groups of four mice, monitoring bioluminescence relative to initial signal (%BLI) over the peritoneal cavity as a signal of tumor burden (Figures 4.5A and B). By day 4 after IP inoculation of ES-2-luc cells, regional bioluminescence from the peritoneal cavity of mice suggested that ES-2-luc cells had already formed solid tumors (Figure 4.5A).[114, 115] In a vehicle control, bioluminescence from ES-2-luc cells in the peritoneum increased rapidly over three weeks, and ascites, *i.e*. fluid in

peritoneum, rapidly formed in mice based on noninvasive bioluminescence images fused with white-light pictures (Figures 4.5A and F). Twenty-one days after control treatment (25 days post cell inoculation), bioluminescence signals of non-treated ES-2-luc-bearing mice increased 8-fold (Figure 4.5B), and the average abdominal radius of control mice increased 1.2-fold due to ascites formation (Figure 4.5C). Tumor burden killed control mice within 27 days post cell inoculation (Figure 4.5E); *ca*. 4 mL of ascites was in the peritoneum. Extensive metastatic tumor foci were observed adhered onto stomach, intestines, colon, and kidneys in sacrificed animals (data not shown).

PEG-*b*-PCL micelles containing PTX (30 mg/kg) were effective in delaying tumor progression during drug treatment (Figures 4.5A and B); however, %BLI increased rapidly after termination of drug treatment, indicating regrowth of tumors. In this treatment group, we observed less ascite formation (Figures 4.5A and F). After 21 days, %BLI was 3-fold higher than the start of treatment and 2.8-fold less than vehicle control mice (Figure 4.5B); however, all mice died within 35 days post cell inoculation (Figure 4.5E).

3-drug PEG-*b*-PCL micelles with PTX, CYP, and GSP at 30, 30, 30 mg/kg, respectively, also prevented tumor progression (Figures 4.5A and B), but notably, %BLI did not increase after the cessation of treatment. Within the first week after treatment, tumors seemed to develop faster than tumors in PTX-treated mice. But after the second dose, %BLI decreased and reached a plateau for about two weeks. After 21 days, the %BLI value for 3-drug PEG-*b*-PCL micelles was 11-fold and 4-fold less than the vehicle control and PTX, respectively (Figure 4.5B). The average radius of abdomen did not significantly change over time (Figure 4.5C). Lastly, 50% of animals treated with 3-drug PEG-*b*-PCL micelles survived for 46 days post cell inoculation.

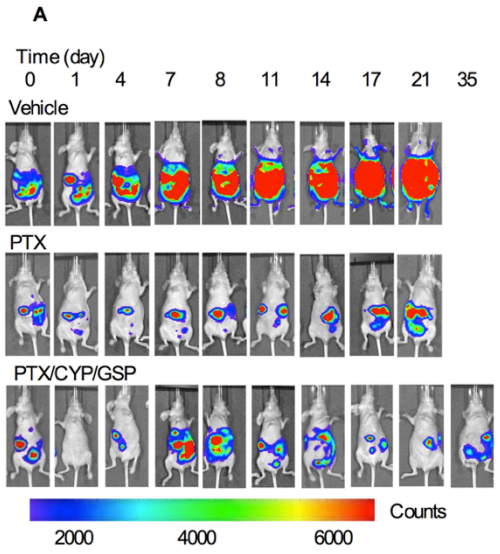
A
Time (day)
0 1 4 7 8 11 14 17 21 35
Vehicle
PTX
PTX/CYP/GSP
Counts
2000 4000 6000

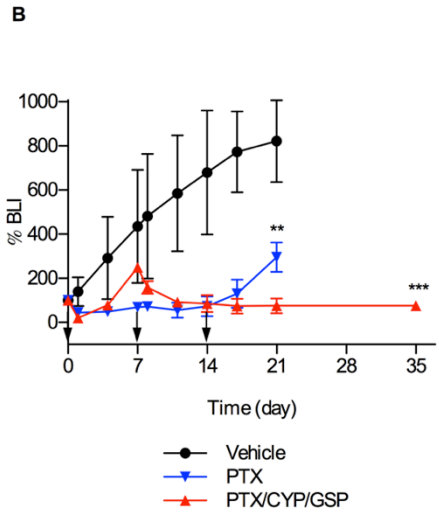
B
% BLI
Time (day)
Vehicle
PTX
PTX/CYP/GSP
**
***

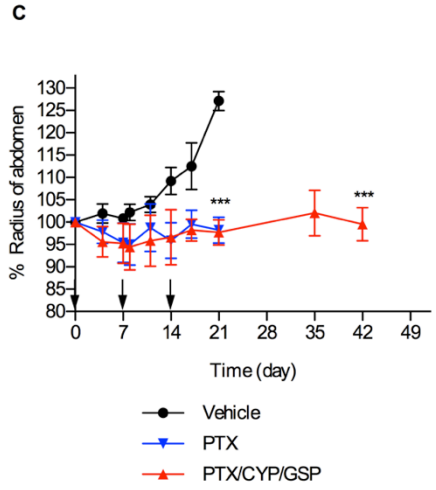
C
% Radius of abdomen
Time (day)
Vehicle
PTX
PTX/CYP/GSP
***
***

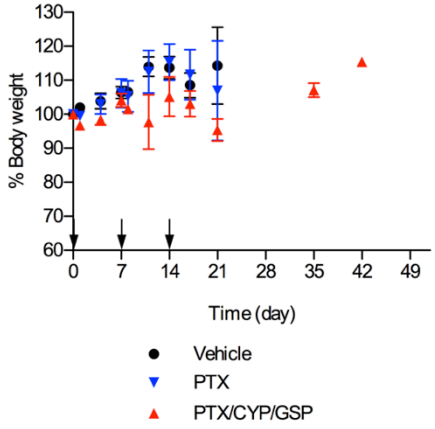
D
% Body weight
Time (day)
Vehicle
PTX
PTX/CYP/GSP

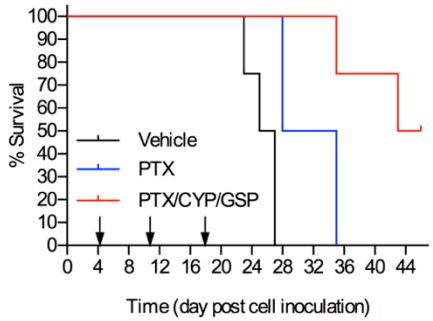
E
% Survival
Vehicle
PTX
PTX/CYP/GSP
Time (day post cell inoculation)

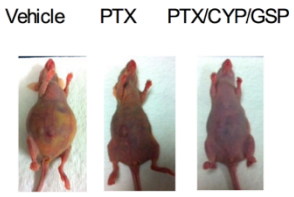
F
Vehicle
PTX
PTX/CYP/GSP

Figure 4.5. Nonevasive bioluminescence imaging and treatment assessment for metastatic ES-2-luc ovarian xenograft model. Results are represented by (A) whole-body bioluminescence images of mice obtained with IVIS imaging system, (B) quantitative bioluminescence intensity (BLI) in ROIs, and (C) % change of radius of abdomen of mice. (D) Body weight change, (E) Kaplan-Meier analysis for survival, and (F) white light observation (on day 25 post cell inoculation) of tumor-bearing mice receiving IP treatment of vehicle, 3-drug PEG-*b*-PCL micelles at 30, 30, and 30 mg/kg, or PEG-*b*-PCL micelles containing PTX at 30 mg/kg on a q7d x 3 schedule (* < 0.05, ** < 0.01, *** < 0.001).

To validate *in vivo* results from bioluminescence imaging, ^{18}F-FLT was used as a PET tracer for the noninvasive visualization of cell proliferation of IP injected ES-2-luc cells and assessment of treatment responses (Figure 4.6A)[116-119]. In the vehicle control, PET imaging showed large tumor masses (highlighted in yellow) at 4 days post cell inoculation that grew larger over 17 days. Tumors were also observed at the start of treatment for PTX-treated mice, but they did not appear to change in size during the course of treatment. In contrast, while tumors were readily discerned at the start of treatment tumors treated with 3-drug PEG-*b*-PCL micelles were eradicated by day 17, noting instead a diffuse signal from ES-2 cells throughout the peritoneum (Figure 4.6A). The high signal of ^{18}F-FLT in the posterior region of mice is due to uptake of ^{18}F-FLT by the kidneys. %SUV on day 17, as a measure of uptake of ^{18}F-FLT in ES-2-luc tumors, was 263, 164, and 86% for vehicle, PTX, and 3-drug PEG-*b*-PCL micelles, respectively (Figure 4.6B).

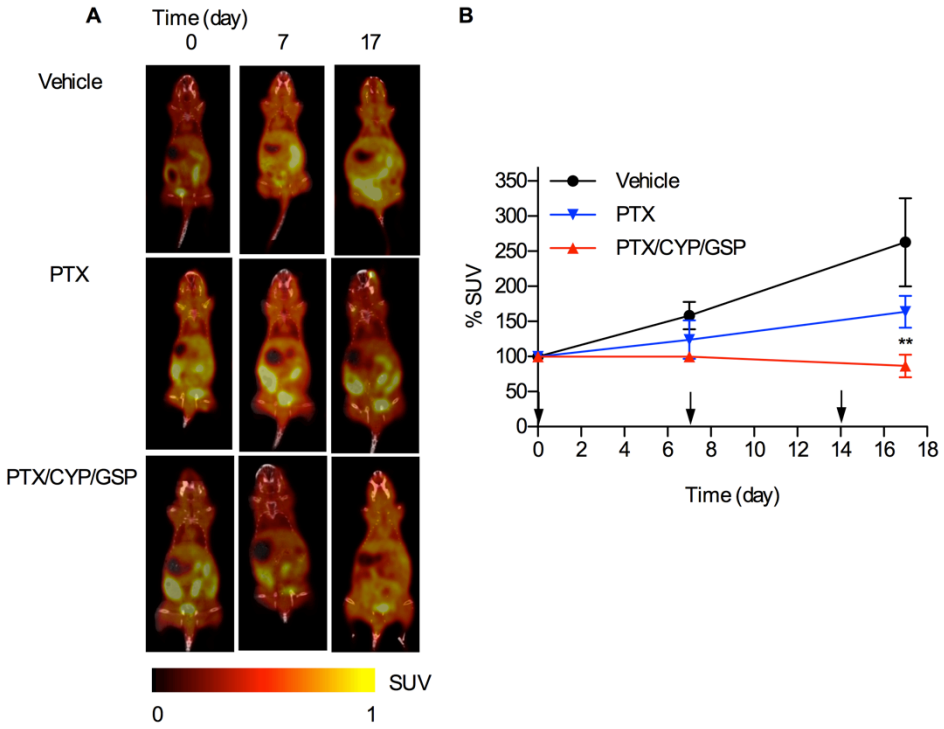

Figure 4.6. Nonevasive microPET/CT imaging and treatment assessment for metastatic ES-2-luc ovarian xenograft model. Results are represented by (A) whole-body images, (B) tracer uptake in ROIs expressed as %SUV of tumor-bearing mice receiving IP treatment of vehicle, 3-drug PEG-*b*-PCL micelles at 30, 30, and 30 mg/kg, or PEG-*b*-PCL micelles containing PTX at 30 mg/kg on a q7d x 3 schedule (* < 0.05, ** < 0.01, *** < 0.001). Tumor tissues at day 0 reached 100-200 mm^3 in volume.

Additionally, 3-drug PEG-*b*-PCL micelles with PTX, CYP, and GSP at 30, 30, 30 mg/kg, respectively, was tested in a SKOV-3-luc ovarian cancer xenograft model of peritoneal carcinomatosis (Figure 4.7). In comparison to the ES-2-luc xenograft model, growth of SKOV-3-luc cells in the peritoneum of mice was slower, and treatment was started 16 days post cell inoculation after appearance of a bioluminescence signal. For the vehicle control, %BLI grew slowly over two weeks and then grew more rapidly for the next two weeks. Both treatment

groups were very effective against SKOV-3-luc ovarian cancer (Figures 4.7A and B), causing a slight decrease in %BLI: 3-fold and 1.5-fold for 3-drug and PTX-treated mice. After 35 days (51 days post cell inoculation), %BLI for 3-drug PEG-*b*-PCL micelles was 2-fold and 73-fold less than %BLI for PTX-treated mice and vehicle control, respectively. Lastly, 75% of vehicle control and 25 % of PTX-treated mice died within 58 days post cell inoculation; however, 100% of the animals receiving 3-drug PEG-*b*-PCL micelles survived with < 15% body weight change until the termination of experiments (Figures 4.7C, D, and E).

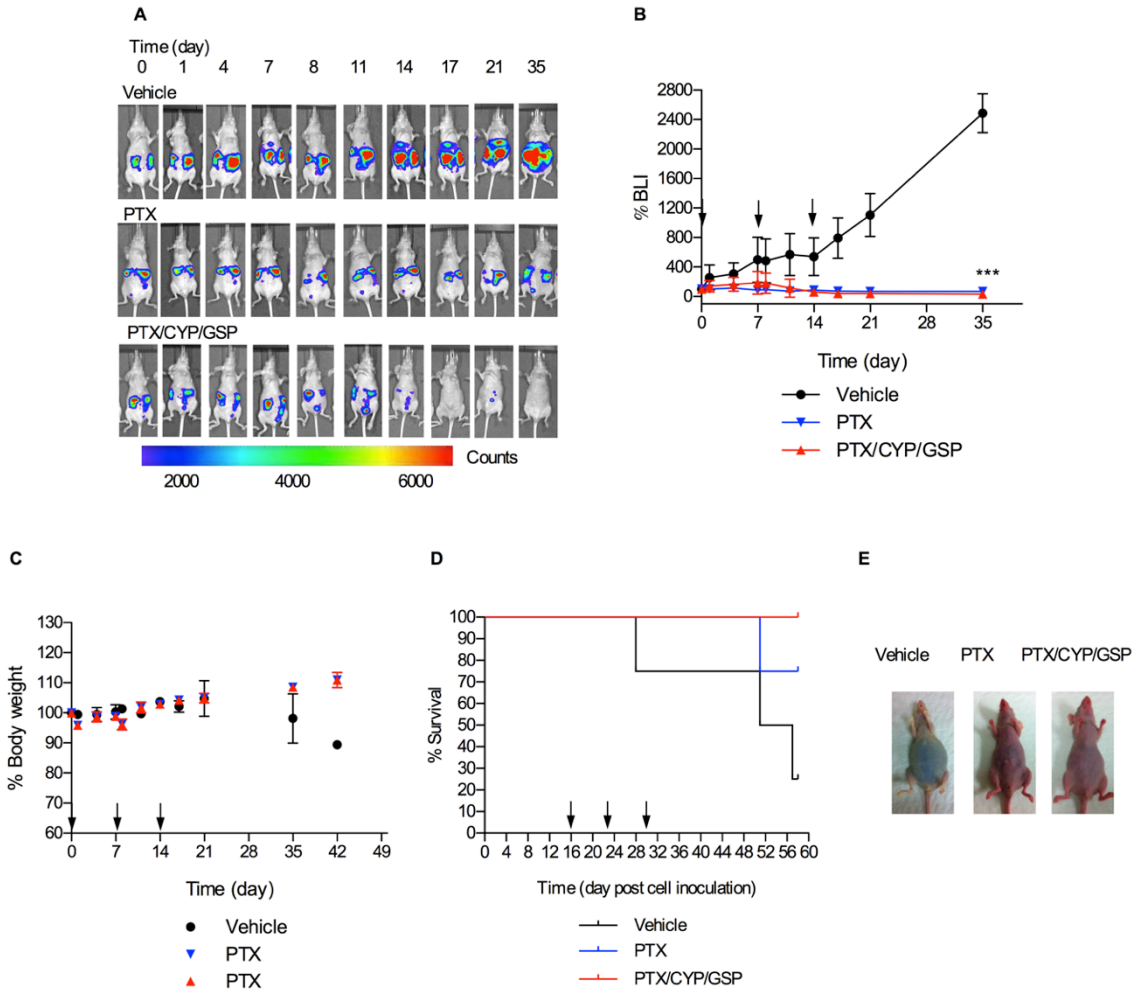

Figure 4.7. Nonevasive bioluminescence imaging and treatment assessment for metastatic SKOV-3-luc ovarian xenograft model. Results are represented by (A) whole-body bioluminescence images of mice obtained with IVIS imaging system and (B) quantitative bioluminescence intensity (BLI) in ROIs. (C) Body weight change, (D) Kaplan-Meier analysis for survival, and (E) white light observation (on day 45 post cell inoculation) of tumor-bearing mice receiving IP treatment of vehicle, 3-drug PEG-*b*-PCL micelles at 30, 30, and 30 mg/kg, or PEG-*b*-PCL micelles containing PTX at 30 mg/kg on a q7d x 3 schedule (* < 0.05, ** < 0.01, *** < 0.001).

4.4. Discussion

IP drug delivery for treatment of peritoneal metastases of ovarian cancer has produced survival benefits in multiple clinical trials despite the fact that IP treatments rely chiefly on vehicles that were developed for intravenous (IV) drug delivery, *e.g*. Cremophor EL for PTX.[108] More recently, novel drug delivery systems for IP drug delivery, *e.g*. liposomes, microparticles, and sustained release gels have generated promising results in ovarian xenograft models.[120] However, research on IP drug delivery has largely focused on the delivery of a single cytotoxic agent. Less attention has been devoted to the IP delivery of molecularly targeted agents for the treatment of ovarian cancer and even less attention on the IP delivery of drug combinations of cytotoxic agent and molecularly targeted agent(s). Amiji and coworkers have done early studies on combination drug delivery using biodegradable polymeric nanoparticles containing PTX and ceramide or PTX and tamoxifen, overcoming multidrug resistance in subcutaneous SKOV-3 xenograft models.[121, 122]

Multi-drug loaded PEG-*b*-PCL micelles may potentially fulfill several major requirements for IP combination drug delivery (Figure 4.1): biocompatibility, multiple drug solubilization, physical stability against drug precipitation, and sustained release. Multi-drug loaded PEG-*b*-PCL micelles enable multi-drug treatment after a single IP injection or infusion, nullifying the requirement of sequential IP dosing of drug combinations for the treatment of

ovarian cancer. Multi-drug loaded PEG-*b*-PCL micelles may derive a major safety benefit for IP combination drug delivery by the elimination of multiple vehicles, *e.g*. Cremophor EL, co-solvents, which are often toxic after either IV or IP administration, noting that the maximum tolerable dose (MTD) of IP bolus PTX solubilized by Cremophor EL was 20 mg/kg/week.[123]

PEG-*b*-PCL micelles prepared by a solvent evaporation technique had a good capacity for PTX, CYP, and GSP, *ca*. 9.4%, resulting in multiple drug solubilization at 18 mg/mL, *ca*. 6.2 mg/mL for each anticancer agent, and PEG-*b*-PCL micelles were obtained with z-average diameters at *ca*. 80 nm, regardless of drug loading (Table 4.1). In prior preclinical and clinical studies, PTX and GSP were solubilized by CrEL and PEG400/Cremophor EL, respectively, for IV administration, and CYP was chemically-modified into a water-soluble analogue (IPI-926).[111, 124, 125] 3-drug PEG-*b*-PCL micelles were fairly physically stable at 25 ºC, although *ca*. 63% of CYP was lost due to precipitation over a 24 hr period (Table 4.2). For *in vitro* and *in vivo* studies, 3-drug PEG-*b*-PCL micelles were tested within *ca*. 1-2 hr after preparation or stored at 4 ºC, where there was higher physical stability. It is noted that drug loss due to precipitation has also been observed for PTX in PEG-*b*-PLA micelles (Genexol-PM) at 25 ºC over 24 hr. Freeze-drying of Genexol-PM and reconstitution were used to enable a stable IV administrated PTX in a sterile aqueous vehicle for clinical trials.

In vitro evidence for sustained release of PTX, CYP, and GSP from 3-drug PEG-*b*-PCL micelles was obtained under approximate sink conditions, with calculated $t_{1/2}$ values at 50, 18, and 30 hr, respectively (Figure 4.2). Our prior studies on 3-drug poly(ethylene glycol)-*block*-poly(*d*,*l*-lactic acid) micelles showed a correlation between the $t_{1/2}$ values for *in vitro* multi-drug release and octanol-water partition coefficients (log P);[30] In contrast, an opposite trend was

observed for 3-drug PEG-*b*-PCL micelles with PTX, CYP, and GSP, with CYP having the fastest release and highest log P value, *ca*. 6.1. The relatively fast release of CYP from 3-drug PEG-*b*-PCL micelles was consistent with the loss of CYP due to precipitation over a 24 hr period at 25 ºC (Table 4.2). Mechanistic analysis for 3-drug PEG-*b*-PCL micelles merits attention, focusing on regions of drug solubilization in PEG-*b*-PCL micelles and drug-drug interactions. In summary, 3-drug PEG-*b*-PCL micelles release PTX, CYP, and GSP over a few days *in vitro*; after IP injection we also predict sustained multi-drug release, which will be verified in pharmacokinetic experiments.

The *in vitro* and *in vivo* activity of 3-drug PEG-*b*-PCL micelles was tested against two human ovarian cancer cell lines, owing to four histological subtypes of ovarian cancer: Serous, mucinous, clear cell, and endometrioid; and tumors having no-distinctive histological features are designated as undifferentiated adenocarcinoma.[126] ES-2 is categorized as undifferentiated adenocarcinoma (aggressive subtype), and SKOV-3 is categorized in serous adenocarcinoma (moderate-grade subtype).[127] 3-drug PEG-*b*-PCL micelles had IC_{50} values of 51 and 67 nM against ES-2-luc and SKOV-3-luc ovarian cancer cells, respectively, based on a decline in bioluminescence, reflecting decreased protein expression (luciferase) (Table 4.3). Previous work by De Souza *et al* showed a linear correlation between bioluminescence from SKOV-3-luc cells and cell viability based on the MTT assay.[107] While the activity of 3-drug PEG-*b*-PCL micelles was not better than PTX in 2-D and 3-D cell culture in terms of IC_{50} value, 3-drug PEG-*b*-PCL micelles at 1000 nM were unique in the disaggregation of ES-2-luc spheroids into smaller cellular aggregates, whereas ES-2-luc spheroids stayed intact after treatment with PTX, but with reduced growth of tumor spheroids, presumably by acting of proliferating ES-2-luc cells in the

periphery (Figure 4.3). It is noted that ovarian cancer cells show anchorage-independent growth in ascites by the formation of tumor spheroids and that ovarian tumor spheroids have been linked to drug resistance due to poor drug penetration or increased pro-survival signaling. Brown and colleagues have also shown that compact ES-2 tumor spheroids have an invasive phenotype, whereas loose, sheet-like SKOV-3 aggregates were unable to invade a 3-D collagen matrix *in vitro*.[128] Thus, disaggregation of ES-2-luc spheroids by 3-drug PEG-*b*-PCL micelles may enhance drug delivery to ovarian cancer cells and preclude invasive behavior, resulting in improved treatment outcomes. It is speculated that disaggregation of ES-2-luc spheroids is induced by multiple mechanisms, such as inhibition of Hh signaling by CYP possibly reversing taxane resistance, improved penetration of PTX into spheroids, and GSP augmented apoptosis.

Both bioluminescence imaging and microPET/CT imaging showed that PTX, CYP, and GSP, injected IP as 3-drug PEG-*b*-PCL micelles, has potent antitumor activity in metastatic ES-2-luc and SKOV-3-luc xenograft models (Figures 4.5-4.7). At the start of drug treatment (4 days post cell inoculation), ES-2-luc tumors were plainly visible in the peritoneum by microPET/CT imaging along with extensive ascite formation, suggesting an advanced stage of disease. Bioluminescence imaging and microPET/CT imaging showed that the tumors spread rapidly in the peritoneum, and median survival time < 30 days. The lethality of ES-2 cells in an IP metastatic xenograft model has been noted in the literature.[129] 3-drug PEG-*b*-PCL micelles with PTX, CYP, and GSP at 30, 30, 30 mg/kg, respectively, prevented the metastatic spread of ES-2-luc tumors in the peritoneum and ascite formation (Figure 4.5). Furthermore, ES-2-luc tumors, plainly visible at the onset of treatment, were completely eradicated after treatment with 3-drug PEG-*b*-PCL micelles (q7d x 3), based on microPET/CT imaging using ^{18}F-FLT as a PET tracer

(Figure 4.6A). Accordingly, ES-2-luc-bearing mice survived longer than mice treated with PTX, where ES-2-luc tumors were still visible after drug treatment (q7d x 3). The antitumor efficacy of 3-drug PEG-*b*-PCL micelles with PTX, CYP, and GSP was also confirmed in an IP metastatic SKOV-3-luc xenograft model (Figure 4.7).

In summary, 3-drug PEG-*b*-PCL micelles disassembled ES-2-luc tumor spheroids *in vitro*, eradicated metastatic ES-2-luc tumors *in vivo*, and prolonged survival, validating the IP delivery of multi-drug polymeric micelles as a meaningful drug delivery strategy for the treatment of ovarian cancer.

4.5. Conclusions

IP drug delivery of PTX, CYP, and GSP was enabled by PEG-*b*-PCL micelles, fulfilling several major requirements for combination drug delivery: Biocompatibility, multiple drug solubilization, physical stability against drug precipitation, and sustained release. Multi-drug loaded PEG-*b*-PCL micelles prepared by a simple solvent evaporation technique enabled solubilization of PTX, CYP, and GSP at *ca*. 18 mg/mL. PEG-*b*-PCL micelles carrying PTX, CYP, and GSP were nanoscopic, fairly stable in aqueous solution, and capable of simultaneous sustained release of PTX, CYP, and GSP *in vitro*. This 3-drug combination was highly effective in metastatic ES-2-luc and SKOV-3-luc xenograft models, eradicating peritoneal tumors and prolonging survival over PTX alone. Antitumor efficacy of PTX, CYP, and GSP may partly be explained by their ability to disassemble ovarian tumor spheroids, which are drug resistant. These results clearly show the unique potential of multi-drug delivery *via* IP-injected polymeric micelles for the treatment of metastatic ovarian cancer.

5 Polymeric Micelles for Apoptosis-Targeted Optical Imaging of Cancer and Intraoperative Surgical Guidance

This chapter has been submitted in full: Cho H.; Cho C. S.; Indig G. L.; Lavasanifar A.; Vakili M.R.; Kwon, G. S. Polymeric micelles for apoptosis-targeted optical imaging of cancer and intraoperative surgical guidance. *PLOS ONE* **2013**, Submitted

5.1. Introduction

Ovarian cancer is portrayed as the disease that whispers due to the indolent symptoms at early stages.[130] Unfortunately, there are no effective screening tests: general screening of serum cancer antigen 125 (CA 125) or transvaginal sonography does not permit early detection of ovarian cancer. In part due to the difficulties in diagnosis, ovarian cancer is the most lethal gynecologic malignancy.[131] The conventional treatment strategy for ovarian cancer involves a combined approach utilizing aggressive cytoreductive surgery and intravenous (IV) chemotherapy (platinum and taxane analogues).[132]

In the last decade, a potential benefit of chemotherapy given through the intraperitoneal (IP) route for ovarian cancer has been seen in several clinical trials, and it has been highlighted that IP chemotherapy can give high response rates within the abdomen due to the peritoneal plasma barrier confining exposure of chemotherapy to peritoneal surfaces, resulting in higher drug concentration in peritoneal cavity.[132]

Surgery is critical for patients with colorectal and ovarian cancers that have spread widely to the peritoneal cavity. There are three types of surgical debulking that have been attempted to treat ovarian cancer patients: (1) primary debulking surgery (initial surgery), which has largely been the standard approach; (2) interval debulking surgery after neoadjuvant chemotherapy (NACT), reserved for patients who are medically unfit for immediate operation or whose extensive metastases cannot be initially resected; and (3) secondary debulking surgery (additional surgery), for patients who develop recurrent chemoresistant ovarian cancer.[130] Although the optimal surgical approach remains controversial, it is very clear that improved intraoperative cancer imaging systems will yield significant benefit for successful surgical

debulking of ovarian cancer. Although radiological approaches such as computed tomography (CT) and magnetic resonance imaging (MRI) have been of great help in characterizing malignancies within peritoneal cavity, they are not useful for intraoperative assessment. In contrast, fluorescence imaging has been shown to be successful in preclinical and clinical trials as an optical technique offering real-time images of surgical targets (peritoneal carcinomatosis and breast cancer) with adequate imaging resolution and high intraoperative sensitivity.[46, 48, 133, 134] Coll and colleagues reported that intraoperative near-infrared (NIR) fluorescence image-guided surgery using a tumor-targeting peptide, RAFT-c(RGDfK)$_4$-Alex Fluor® 700 (IV route), in a TSA-pGL3-bearing mouse model of peritoneal adenocarcinoma could improve the quality of surgical debulking by doubling the number of detected tumor nodules and shortening operation time.[53] Ntziachristos and colleagues successfully conducted the first human trial of intraoperative tumor-specific fluorescence imaging in staging and debulking surgery for ovarian cancer using IV folate-FITC, and proved that the number of tumors detected by surgeons under the guidance of tumor-specific fluorescence images increased by 5.3-fold (34 *vs.* 7) compared with white light visual observation alone.[48] Frangioni and co-workers also demonstrated the utility of the FLARE™ (Fluorescence-Assisted Resection and Exploration™) device for image-guided oncologic surgery in the first human clinical trial of breast cancer sentinel lymph node (SLN) mapping following intratumoral/subcutaneous injection of 1:1 mixture of indocyanine green and human serum albumin (ICG:HAS).[46] In this trial, SLNs identified by lymphoscintigraphy and NIR fluorescence imaging were identical in 4 of 6 breast cancer patients.

Application of nanomaterials as optical fluorescence imaging agents using quantum dots, gold nanoparticles, and fluorescence probe-containing or -conjugated nanoparticles has drawn

attention for diagnostic purposes in pre-clinical studies.[35, 36, 51, 135, 136] Polymeric micelles belong to a major class of nanomaterials that have entered several clinical trials for drug delivery, *eg*. SP-1049C (doxorubicin, phase II), Genexol-PM (paclitaxel, phase II), and NC-6004 (cisplatin, phase I).[137] Polymeric micelles offer several advantages not only as drug carriers but also as optical imaging agents in oncology: small sized-particles with narrow size distribution, structural stability, high water solubility, low toxic side effect over conventional surfactants (*eg*. Cremophor EL), preferential accumulation at solid tumors through the enhanced permeability and retention (EPR) effect, evading renal filtration, and multifunctionality by surface decoration.

It has been discussed that apoptosis-targeted drug delivery and cancer imaging (specially for imaging tumor responsiveness to chemotherapy)[44, 138] could be superior to cancer-associated antigen- or protein-targeting strategy in a broad range of malignancies, because substantial heterogeneity in cancer cell populations does not guarantee the exclusive presence of antigen and protein biomarkers in target tissues.[139] Surgical oncologists could take advantage of apoptosis-targeted tumor imaging (independent of cell type and cell death-inducing triggers) after NACT with greater precision and accuracy.[140] Thus, surgical tumor debulking using intraoperative visual guidance with real-time NIR fluorescence images could result in improved surgical accuracy and outcome. One of the most prominent characteristics of programmed cell death, apoptosis, is the externalization of phosphatidylserine (PS) which normally resides predominantly in the inner leaflet of the plasma membrane.[140]

In the chapter 2, we reported that poly(ethylene glycol)-*block*-poly(ε-caprolactone) (PEG-*b*-PCL) micelles containing DiR (1,1'-dioctadecyltetramethyl indotricarbocyanine iodide) could passively accumulate in LS180 human solid colon tumor tissues by the EPR effect and

provide noninvasive delineation of LS180 tumor tissues with a tumor-to-muscle ratio of 30-43 from collected tissues.[99] We also observed enhanced DiR accumulation in "primed" LS180 tumor tissues after an IV injection of multi-drug containing poly(ethylene glycol)-*block*-poly($_{D,L}$-lactic acid) (PEG-*b*-PLA) micelles, suggesting the availability of a tandem of polymeric micelles that could possibly enable improved tumor delineation for use in surgical oncology in the chapter 3.[112] In the chapter 4, PEG-*b*-PCL micelles with paclitaxel (PTX), cyclopamine (CYP), and gossypol (GSP) at 30, 30, and 30 mg/kg, respectively (q7d x 3) delivered through IP, prevented the metastatic spread of ovarian cancer and extensive ascites formation, resulting in prolonged survival in peritoneally metastatic ES-2-luc (undifferentiated adenocarcinoma, aggressive subtype) and SKOV-3-luc (serous adenocarcinoma, moderate-grade subtype) murine xenograft models of ovarian cancer.[141]

We propose a novel two-step strategy for NACT, apoptosis-targeted optical imaging and intraoperative surgical guidance (Figure 5.1). In step one, PEG-*b*-PCL micelles containing PTX, CYP, and GSP are used for IP NACT and apoptosis induction in tumor tissues. In a second step, apoptosis-targeting PEG-*b*-PCL micelles containing DiR may actively accumulate in apoptotic tumor tissues, permitting optical fluorescence imaging of apoptosis in a real-time manner (Figure 5.1). DiR molecules, NIR fluorescence probes emitting light in the NIR wavelength window, could be useful as an optical fluorescence imaging agent, avoiding strong autofluorescence from skin and blood and allowing detectable signals to be measured through several millimeters of tissues.[56] Here, we show that this two-step strategy enhanced tumor delineation in NIR fluorescence optical imaging and provided useful guidance for interval debulking surgery in an

IP ES-2-luc-bearing xenograft model of ovarian cancer, coupling two applications of polymeric micelles in drug delivery and optical imaging for surgical oncological therapy of ovarian cancer.

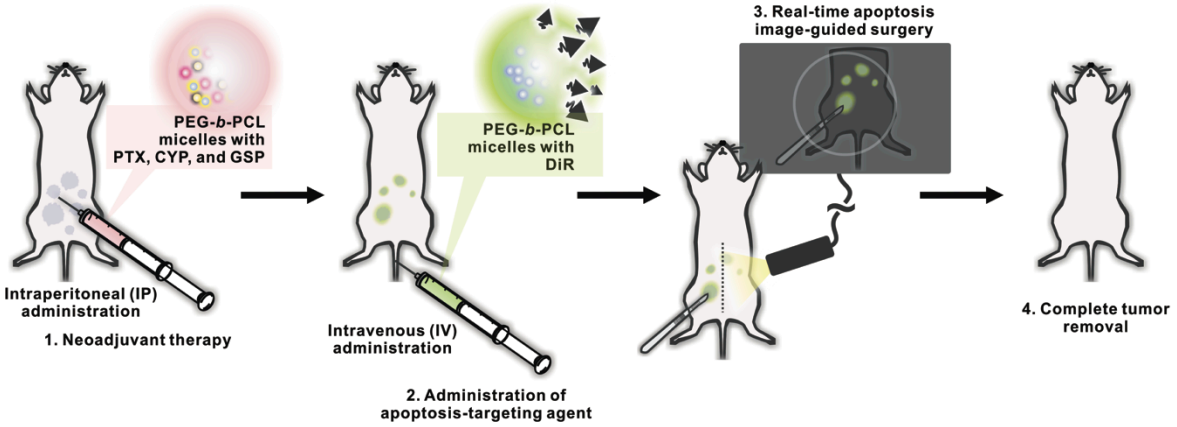

Figure 5.1. Schematic illustration of two-step strategy for neoadjuvant therapy, apoptosis-targeted optical imaging and intraoperative surgical guidance, enabled by a tandem of PEG-*b*-PCL micelles.

5.2. Materials and methods

5.2.1. Preparation of PEG-*b*-PCL micelles carrying PTX, CYP, and GSP.

Drug-loaded PEG-*b*-PCL micelles were prepared by a solvent evaporation method as previous described.[141] Briefly, 4.0 mg of PTX, CYP, and GSP each and 120 mg of PEG-*b*-PCL (M_n of PEG = 5,000 g/mol, M_n of PCL = 10,000 g/mol, and M_w/M_n = 1.26) (Advanced Polymer Materials Inc., Montreal, Canada) were completely dissolved in 1.0 mL of acetone followed by a rapid addition of 1.0 mL of pre-warmed 0.9% saline at 60 °C with vigorous mixing. Acetone was evaporated under reduced pressure at 60 °C. The aqueous micelle solution was centrifuged for 5 min at 10,000 g and passed through a 0.2 μm regenerated cellulose (RC) sterile syringe filter (Corning, Tewksbury, MA) to remove insoluble drugs. The content of PTX, CYP, and GSP in

PEG-*b*-PCL micelles was quantified by reverse phase-HPLC (RP-HPLC) system using a Shimadzu Prominence HPLC system (Himadzu, Japan) as previously described.[141] The separation of PTX, CYP, and GSP was done in an isocratic mode with mobile phase of 55% acetonitrile, 45% distilled water, and 0.1% trifluoroacetic acid. PTX, CYP, and GSP were monitored at 227, 204, and 373 nm, respectively, and eluted at 2.7 min, 1.9 min, and 10.6 min, respectively.

5.2.2. Preparations of apoptosis-targeting PEG-*b*-PCL and methoxy-PEG-*b*-PCL micelles carrying DiR.

Preparation of apoptosis-targeting PEG-*b*-PCL (GFNFRLKAGAKIRFGS-PEG-*b*-PCL) micelles carrying DiR was started with the conversion of acetal groups on the surface of PEG-*b*-PCL micelles to aldehyde groups. Acetal-PEG-*b*-PCL (M_n of PEG = 5,000 g/mol, M_n of PCL = 5,000 g/mol, and M_w/M_n = 1.13) was kindly provided by Dr. Afsaneh Lavasanifar, University of Alberta (Edmonton, Canada). The conversion method was slightly modification from the literature.[142] Acetal-PEG-*b*-PCL copolymer was dissolved in acetone at a concentration of 20 mg/mL. Distilled water was then rapidly added to the polymer solution with vigorous stirring at room temperature followed by evaporation of acetone under reduced pressure at room temperature. The micelle solution was centrifuged for 5 min at 10,000 g and passed through a 0.2 μm RC sterile syringe filter. Conversion of acetal groups on acetal-PEG-*b*-PCL micelles was carried out at pH 2.0 by adding 0.5 N of HCl. After 4 h of moderate stirring at room temperature, the reaction was neutralized with 0.5 N of NaOH to stop the reaction. The neutralized micelle solution was then dialyzed against water with dialysis membrane (MWCO 6,000 g/mol) to

remove the salt overnight and lyophilized for 48 hr for future use. Lyophilized sample was dissolved in $CDCl_3$ (6 mg/mL) to estimate the conversion rate from the acetal to aldehyde group on PEG-*b*-PCL by ^{1}H NMR. Free peptide, GFNFRLKAGAKIRFGS (UW Biotechnology Center, Madison, WI) at Mw = 1,769 g/mol, was dissolved in HEPES buffer (10 mM, pH 6.4) and mixed with the lyophilized aldehyde-PEG-*b*-PCL micelles to obtain 4 mg/mL of polymer and 0.35 mg/mL of peptide concentration at 2:1 molar ratio (aldehyde-PEG-*b*-PCL:GFNFRLKAGAKIRFGS). After 2 hr of moderate stirring, $NaBH_3CN$ (10 equiv) was added to the mixture to reduce Schiff base. After 4 days, the micelle solution was again dialyzed against water with a dialysis membrane (MWCO 6,000 g/mol) overnight and then GFNFRLKAGAKIRFGS-PEG-*b*-PCL micelle solution was lyophilized for 48 hr. The conjugation efficiency of peptide on aldehyde-PEG-*b*-PCL was determined by RP-HPLC analysis. Briefly, samples (10 μL) were injected into a Zorbax 300SB-C18 column (4.6 x 15 mm, 3.5 mm, Agilent) kept at 40 °C and the flow rate was 0.8 mL/min. Gradient elution was performed with the mobile phase of 0.1% trifluoroacetic acid in distilled water and 0.1% trifluoroacetic acid in 90/10 (v/v) acetonitrile/distilled water. The mobile phase was programed as follows: 0 min 85% solvent A and 15% solvent B; 35 min, 50% solvent A and 50% solvent B. Free peptide was monitored at 215 nm and eluted at 16 min. The amount of peptide conjugated on PEG-*b*-PCL micelles was calculated by subtracting the amount of free peptide from the amount of peptide initially added to reaction. In parallel, lyophilized peptide conjugated on PEG-*b*-PCL was dissolved in DMSO-d_6 (6 mg/mL) to calculate conjugation rate of peptide on PEG-*b*-PCL by ^{1}H NMR at 80 °C.

Methoxy-PEG-*b*-PCL and apoptosis-targeting PEG-*b*-PCL micelles carrying DiR were prepared by a solvent evaporation method: 4.0 mg of polymers and 0.1 mg of DiR (Invitrogen, Carlsbad, CA) were dissolved in 1.0 mL of acetone, followed by a rapid addition of PBS (10 mM, pH 7.4) with vigorous mixing. Acetone was evaporated under reduced pressure at room temperature. The aqueous micelle solution containing DiR was centrifuged for 5 min at 10,000 *xg* and passed through a 0.2 μm RC sterile syringe filter to remove unincorporated DiR. The content of DiR in micelles was quantified by RP-HPLC as previously described.[112] The elution of DiR was done in a gradient mode with mobile phase of 70% distilled water and 0.07% trifluoroacetic acid as a solvent A and 30% acetonitrile and 0.03% trifluoroacetic acid as a solvent B. DiR was monitored at 745 nm and eluted at 16 min.

5.2.3. Physical characterization of methoxy-PEG-*b*-PCL and apoptosis-targeting PEG-*b*-PCL micelles carrying DiR.

Z-average diameters of methoxy-PEG-*b*-PCL micelles and apoptosis-targeting PEG-*b*-PCL micelles carrying DiR were determined by dynamic light scattering (DLS) measurements using Zetasizer Nano-ZS (Malvern Instruments, United Kingdom) at 25 °C with a detection angle of 173 ° and a He-Ne ion laser (4 mW, λ = 633 nm) for the incident beam. Autocorrelation functions were created based on cumulant analysis, calculating the hydrodynamic diameter of micelles from the Stokes-Einstein equation and the polydispersity index (PDI). Prior to measurements, micelle solutions were diluted with PBS (10 mM, pH 7.4) to give a polymer concentration at ~ 0.4 mg/mL that represents the polymer concentration above the critical micelle concentration. DiR loading efficiency was shown as % weight DiR/weight polymer. The

in vitro DiR release kinetics of methoxy-PEG-*b*-PCL and apoptosis-targeting PEG-*b*-PCL micelles carrying DiR was studied to estimate the time for 50% drug release ($t_{1/2}$) based on a one-phase decay model using GraphPad Prism version 5.00 for Mac OS X (La Jolla, CA). DiR-loaded micelles, representing 100 mg/mL of DiR, were added into dialysis cassettes (MWCO 20,000 g/mol), and cassettes were placed in 2.0 L of PBS (10 mM, pH 7.4) at 37 °C with moderate stirring. Samples (20 μL) were withdrawn from cassettes at various time points, 0, 0.5, 1, 2, 3, 8, 12, and 24 hr and after each sampling, cassettes were replenished with 20 μL of fresh PBS (10 mM, pH 7.4). The content of DiR in micelles left in cassettes was analyzed by RP-HPLC as described above.

5.2.4. Assessment of PS-selective binding of apoptosis-targeting PEG-*b*-PCL micelles carrying DiR.

Binding of apoptosis-targeting PEG-*b*-PCL micelles carrying DiR to PS was assessed using phospholipid-coated well plates[143] and 3-D tumor spheroids formed from luciferase-expressing ES-2-luc cells.

PC (phosphatidylcholine) or PS solubilized in ethanol was immobilized on clear-bottom 96-well plates at a concentration of about 200 μM in each well, and ethanol was evaporated at room temperature overnight. Some of PC or PS-coated wells were incubated with 1.0 μM of free peptide for 3 hr to saturate PS on phospholipid-coated wells. Apoptosis-targeting PEG-*b*-PCL micelles carrying DiR, representing 1.0 μM of peptide and 500 nM of DiR, were added to wells and incubated for 1 hr at room temperature in dark. Each well was washed with PBS (10

mM, pH 7.4) and apoptosis-targeting PEG-*b*-PCL micelles carrying DiR bound on wells was detected by Xenogen IVIS® 200 Series (Caliper Life Sciences, Hopkinton, MA).

ES-2-luc 3-D tumor spheroids were generated by plating 5,000 ES-2-luc cells/well in agarose-coated 96-well plates and incubated for 4 days. ES-2 human ovarian cancer cells were stably transfected with luciferase-expressing plasmid pGL4.51 containing the neomycin-resistance gene (Promega, Madison, WI) using Lipofectamine 2000™ (Invitrogen, Carlsbad, CA) as previously described.[141] ES-2-luc cells were cultured in McCoy's 5a medium supplemented with 1% L-glutamine, 10% fetal bovine serum, 1% penicillin/streptomycin, and 750 mg/mL G418 antibiotics and maintained at 37 °C under an atmosphere of 5% CO_2 in a humidified incubator. PEG-*b*-PCL micelles containing PTX, CYP, and GSP (3.3, 3.3, and 3.3 nM, respectively) were added to ES-2-luc tumor spheroids and incubated for 3 days. Some of treated ES-2-luc spheroids were incubated 3 hr with 200 nM of free peptide to saturate PS exposed on tumor spheroids. Apoptosis-targeting PEG-*b*-PCL micelles carrying DiR were then added to ES-2-luc tumor spheroids at a final concentrations of 200 nM peptide and 100 nM DiR and incubated for 30 min at 37 °C in 5% CO_2 humidified incubator. As a control, bioluminescence intensity (BLI) of ES-2-luc cells was also monitored to assure that ES-2-luc tumor spheroids were consistently formed in each well, using Xenogen IVIS® 200 Series.

5.2.5. IP human ovarian cancer xenograft and micelle treatments.

Female 6-8 week-old athymic nude Foxnl^{nu} mice were purchased from Harlan Laboratories (Madison, WI). All animal experiments were approved by UW-Madison's Institutional Animal Care and Use Committee and conducted in agreement with the institutional

and NIH guidance. General anesthesia was induced with 1.5% isoflurane/oxygen and maintained with 1% isoflurane/oxygen. ES-2-luc cells were trypsinized, collected from sub-confluent cultures, and 1 x 10^6 cells/animal of ES-2-luc cells were injected into the peritoneal cavity of anesthetized mice. IP injection of PEG-*b*-PCL micelles carrying 30, 30, and 30 mg/kg of PTX, CYP, and GSP was performed 7 days post IP inoculation of ES-2-luc cells after observation of bioluminescence signal in whole-body images of animals by Xenogen IVIS® 200 Series. One day after IP injection of PEG-*b*-PCL micelles containing PTX, CYP, and GSP, methoxy or apoptosis-targeting PEG-*b*-PCL micelles carrying 250 μg/kg of DiR was injected through the tail vein of anesthetized animals. Body weights of animals were measured by a portable scale, and general appearance and mortality of animals was carefully monitored during all sets of animal experiments.

5.2.6. TUNEL assay

ES-2-luc-bearing xenograft was dosed through IP route with PEG-*b*-PCL micelles carrying PTX, CYP, and GSP on day 7 after ES-2-luc cells were inoculated in the peritoneal cavity. Afterwards, animals (n = 4) were sacrificed at 0, 12, 24, 48, and 72 hr post micelle treatment. Tumor, spleen, kidney, and liver tissues were dissected. DNA fragmentation induced by apoptosis was detected in tissues by TdT-mediated dUTP Nick-End Labeling (TUNEL) method using DeadEnd Fluorometric TUNEL assay kit (Promega, Madison, WI). Tissues were frozen sectioned into 10 mm slices, permeabilized by proteinase K, and fixed with 4% formaldehyde. The reaction mixture consisting of TdT and fluorescein-labeled dUTP was added to fixed section of tissues and incubated for 1 hr at 37 °C in a humidified chamber in dark.

Fluorescein-labeled DNA fragments and nuclei of cells couterstained by DAPI were visualized at 520 nm and 460 nm, respectively, using a confocal microscope (Olympus FV1000 FLUOVIEW, Minneapolis, MN). Apoptotic cells and nuclei of cells were shown in green and blue, respectively.

5.2.7. Bioluminescence and fluorescence imagings

Xenogen IVIS® 200 Series was used to image both bioluminescence and fluorescence from objects *in vitro*, *in vivo*, and *ex vivo*. Xenogen IVIS® 200 Series was equipped with a 150 W quartz halogen lamp and a 1 mW power scanning laser. Images were screen-displayed with the spatial resolution of > 60 μm/pixel. Bioluminescence images were acquired by a charged couple device (CCD) camera with the following parameters: exposure time = 1 sec, binning = medium, and f/stop = 2. *In vitro*, D-luciferin (Caliper Life Science, Hopinton, MA) at 10 mg/well was added to ES-2-luc tumor spheroids 5 min prior to bioluminescence imaging, and *in vivo*, D-luciferin at 113 mg/kg was injected IP into ES-2-luc-bearing xenograft model 5 min prior to whole-body bioluminescence imaging. The dynamic of ES-2-luc tumor growth was collected and shown as color-coded images using Live Imaging® software for quantitative analysis and BLI of ES-2-luc tumors was scaled by total counts.

Fluorescence images were also acquired by a charged couple device (CCD) camera with the following parameters: exposure time = 1 sec, binning = medium, and f/stop = 2. A filter setting for DiR detection was fixed at 745 nm for excitation and at 800 nm for emission. All color-coded images were collected using Live Imaging® software for image acquisition and analysis. FLI of DiR was demonstrated by average radiant efficiency, total photons per second

per square centimeter per steradian in the irradiance range (microwatts per square centimeter): [p/s/cm^2/sr]/[μW/cm^2]. The fluorescence of DiR in tumor tissues was determined from the average radiant efficiency at ROI (region of interest) drawn around tumor tissues preset by bioluminescence imaging of an identical animal.

Whole-body bioluminescence and fluorescence images were recorded at 6, 12, 24, and 48 hr post an IV injection of PEG-*b*-PCL micelles carrying DiR. Mice were placed in abdominal positions to obtain whole-body color-coded bioluminescence and fluorescence images. All equipment settings for bioluminescence and fluorescence imagings were identical in the time course experiment.

5.2.8. Real-time fluorescence imaging acquisition in animals

Fluobeam® 800 (Fluoptics, Grenoble, France) is a 2-D NIR fluorescence imaging system composed of CCD camera and an integrated NIR light source (100 mW) with an excitation wavelength at 780 nm and an emission wavelength at > 820 nm. This system provided 7.5 x 10 cm of homogeneous lightened field and the portable hand-held system composed of camera and laser was located approximately 20 cm above the object. Fluorescence images were screen-displayed with the spatial resolution of 110 μm/pixel and recorded as either black-and-white static images (9 images/sec) or real-time videos (25 images/sec).

5.2.9. Surgical procedure

Animals received an IP injection of D-Luciferin (113 mg/kg) 5 min prior to the whole-body bioluminescence imaging on day 9 after ES-2-luc cell inoculation (24 hr post IV injection

of PEG-*b*-PCL micelles carrying DiR). After whole-body bioluminescence imaging was carried out, animals were sacrificed immediately. All sacrificed animals underwent a midline laparotomy and bioluminescence whole-body images of incised animals were obtained again. All surgical procedures were performed on sacrificed animals and by a surgical oncologist experienced in murine surgery.

In one set of experiments (n = 4), for comparison, the traditional surgical tumor resection was performed under the normal white-light. When surgical tumor resection was deemed satisfactory, dissected tumor-like tissues and carcass were scanned by Xenogen IVIS® 200 Series to obtain bioluminescence images. In another group of animals (n = 4), NIR imaging system, the Fluobeam® 800 NIR imaging system was turned on and the surgical tumor resection was assisted by real-time fluorescence images displayed on the screen. When tumor-like FLU^+ (fluoprescence-positive) tissues were excised as completely as possible, dissected tumor-like tissues and the carcass were scanned using the Xenogen IVIS® 200 Series to obtain bioluminescence and fluorescence images.

The duration of surgery was recorded from the time of incision to completion of tumor debulking. Surgical accuracy was assessed using two calculations: (1) % sum of BLU^+ tumor-like tissues to sum of total tumor-like tissues excised throughout the surgical procedure, and (2) total counts of BLI of [ROI in mid-line incised animal minus ROI in dissected animal] over those of ROI in mid-line incised animal. Surgical accuracy was also measured by calculating a post-resection peritoneal cancer index (PCI) as described by Sugarbaker.[132] The PCI relies on the distribution and size of lesions in the abdomen of animal. In this study, PCI was adapted to tumor sizes in mice with the following scores: The abdomen was divided into 13 regions (Figure

5.9) and the lesion size (LS) was scored (0 to 3) in each region as follows: no visual tumors (LS = 0), > 0 to 0.5 mm tumor (LS = 1), 0.6 to 2.0 mm tumor (LS = 2), and > 2.0 mm tumor (LS = 3). Total LS score per animal was summated as a numerical score which can be ranged from 0 (no tumors observed) to 39 (13 areas x 3).

5.2.10. Statistical analysis.

Statistical analysis was done using one-way ANOVA at 5% significance level combined with Tukey's multiple comparison tests by GraphPad Prism ver 5.00 for Mac OS X (La Jolla, CA).

5.3. Results

5.3.1. Characterization of apoptosis-targeting PEG-*b*-PCL micelles carrying DiR

Table 5.1 presents sizes and loading efficiencies (% weight DiR/weight polymer) of apoptosis-targeting PEG-*b*-PCL (GFNFRLKAGAKIRFGS-PEG-*b*-PCL) and methoxy-PEG-*b*-PCL micelles achieved after forming DiR-incorporated micelles by a solvent evaporation technique. Apoptosis-targeting PEG-*b*-PCL micelles had a z-average diameter of 83 ± 2 nm (polydispersity index, PDI 0.1) and methoxy-PEG-*b*-PCL micelles had a z-average diameter of 45 ± 2 nm (PDI 0.1). The loading efficiency of DiR for both micelles was approximately 2%. Peptide (GFNFRLKAGAKIRFGS) was conjugated onto PEG-*b*-PCL micelles with the molar conjugation ratio at 30% *via* a Schiff base reaction, based on results from both HPLC (subtractive quantification of non-conjugated peptide from peptide initially added for reaction) and ^{1}H NMR (quantification of conjugated peptide) analyses (Scheme 5.1). In ^{1}H NMR analysis,

the relative intensity ratio of the peak of benzyl protons of phenylalanine at δ = 7.2 ppm in peptide to the methylene proton peak of PEG protons at δ = 3.7 ppm determined the level of peptide on PEG-*b*-PCL. The data for peptide quantification from HPLC and ^{1}H NMR provided comparable values. No significant difference in $t_{1/2}$ value of DiR for both micelles was observed ($t_{1/2}$ = *ca*. 2 hr) with a similar pattern of *in vitro* DiR release.

Micelles	Size (nm)	PDI	Peptide conjugation (%)	DiR loading efficiency (%)	Half-life ($t_{1/2}$) of DiR release (hr)
Apoptosis-targeting PEG-*b*-PCL micelles	83.4 ± 1.8	0.1 ± 0.0	30	2.4 ± 0.1	2.2
Methoxy-PEG-*b*-PCL micelles	45.1 ± 2.0	0.1 ± 0.0	N/A	2.1 ± 0.2	2.0

Table 5.1. Physicochemical properties of PEG-*b*-PCL micelles carrying DiR.

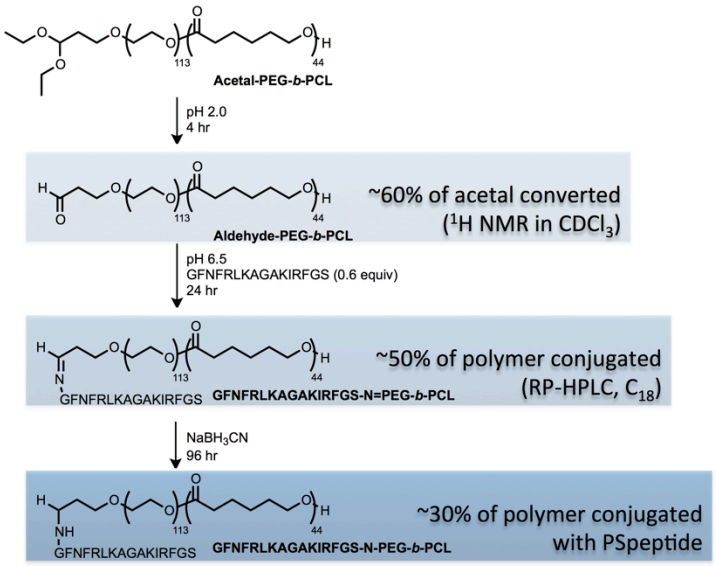

Scheme 5.1. Synthetic scheme of GFNFRLKAGAKIRFGS-PEG-*b*-PCL.

5.3.2. *In vitro* binding studies

Binding of apoptosis-targeting PEG-*b*-PCL micelles carrying DiR to PS was validated in both phospholipid PC or PS-coated 96-well plates and apoptosis-induced ES-2-luc tumor spheroids pretreated with PEG-*b*-PCL micelles with PTX, CYP, and GSP as shown in Figure 2. Considering fluorescence intensity (FLI) of DiR delivered by apoptosis-targeting PEG-*b*-PCL micelles to PS-coated wells to be 100%, apoptosis-targeting PEG-*b*-PCL micelles carrying DiR showed lower adsorption onto PC-coated wells (49 ± 1%), showing a 2-fold weaker FLI on PC-coated wells from DiR (Figure 5.2A). In a competitive binding test, free peptide added prior to the binding study substantially blocked the binding of apoptosis-targeting PEG-*b*-PCL micelles carrying DiR to PS and resulted in a 5-fold decreased FLI of DiR in PS-coated plates (15 ± 2%). Binding of methoxy-PEG-*b*-PCL micelles carrying DiR to both PS- and PC-coated wells was equivalent *ca*. 19%, and PS saturation did not significantly affect the binding affinity of methoxy-PEG-*b*-PCL micelles carrying DiR to both PS- and PC-coated wells.

A similar pattern of binding was observed in ES-2-luc tumor spheroids pretreated with PEG-*b*-PCL micelles carrying PTX, CYP, and GSP at 3.3, 3.3, and 3.3 nM, respectively (spheroids maintained their spherical integrity after treatment) (Figure 5.2B). Assuming PS was externalized by apoptosis induction after treating with PEG-*b*-PCL micelles carrying PTX, CYP, and GSP in equally-sized ES-2-luc tumor spheroids, DiR molecules delivered by apoptosis-targeting PEG-*b*-PCL micelles were observed in tumor spheroids without PS saturation based on FLI of DiR, whereas 42 ± 4% of DiR molecules delivered by the same micelles were detected in tumor spheroids under the condition of PS saturation, indicating decreased DiR accumulation by

2.4-fold in a competitive binding test. Regardless of PS saturation, FLI of DiR molecules delivered by methoxy-PEG-*b*-PCL micelles (55-60%) was not statistically different.

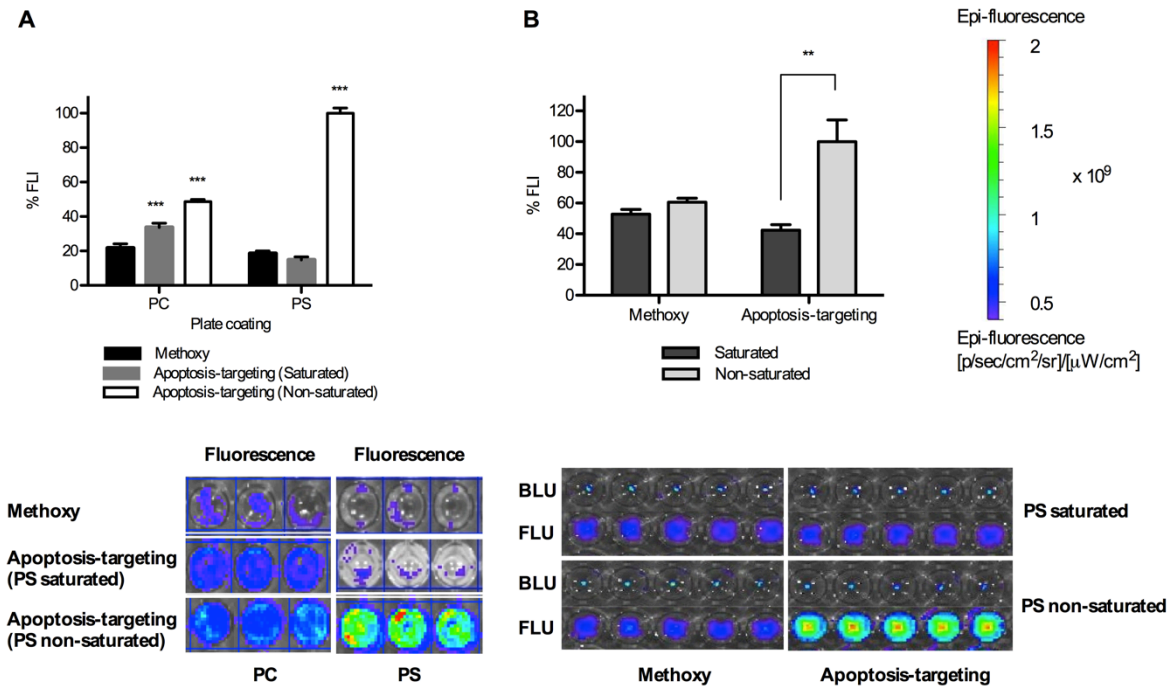

Figure 5.2. Assessment of competitive PS- or apoptosis-binding of apoptosis-targeting PEG-*b*-PCL micelles carrying DiR by PS saturation with free peptides *in vitro*. Results are presented as %FLI DiR molecules bound on plates and %FLI from DiR molecules bound on ES-2-luc ovarian tumor spheroids. BLI from ES-2-luc cells and FLI from DiR molecules were quantified using Xenogen IVIS® 200 Series. (A) Competitive binding test of apoptosis-targeting PEG-*b*-PCL micelles carrying DiR (1.0 μM peptide and 500 nM DiR) to PC- or PS-coated 96-well plates (total 200 μM of phospholipid). (B) Competitive binding test of apoptosis-targeting PEG-*b*-PCL micelles carrying DiR to apoptosis-induced ES-2-luc ovarian tumor spheroids (** < 0.01, *** < 0.001).

5.3.3. *Ex vivo* apoptosis detection

Evidence for apoptosis induction at tumor tissues after a single IP injection of PEG-*b*-PCL micelles carrying PTX, CYP, and GSP to ES-2-luc-bearing xenograft (on day 7 post IP ES-2-luc cell inoculation) was obtained from resected tumor tissues, which were collected at 12, 24, 48, and 72 hr after an IP injection of PEG-*b*-PCL micelles carrying PTX, CYP, and GSP at 30,

30, and 30 mg/kg, respectively, sectioned into 10 μm, and visualized by confocal microscope. In Figure 5.3, a few green colored-DNA fragments in apoptotic cells appeared at tumor tissues at 12 hr, more green dots were clearly visible at 24 hr, and then there were faint signs of DNA fragmentation were present 48 hr post treatment. Apoptotic cells at the kidney and liver were not visible, but a few apoptotic cells were observed at the spleen at 24 hr post treatment.

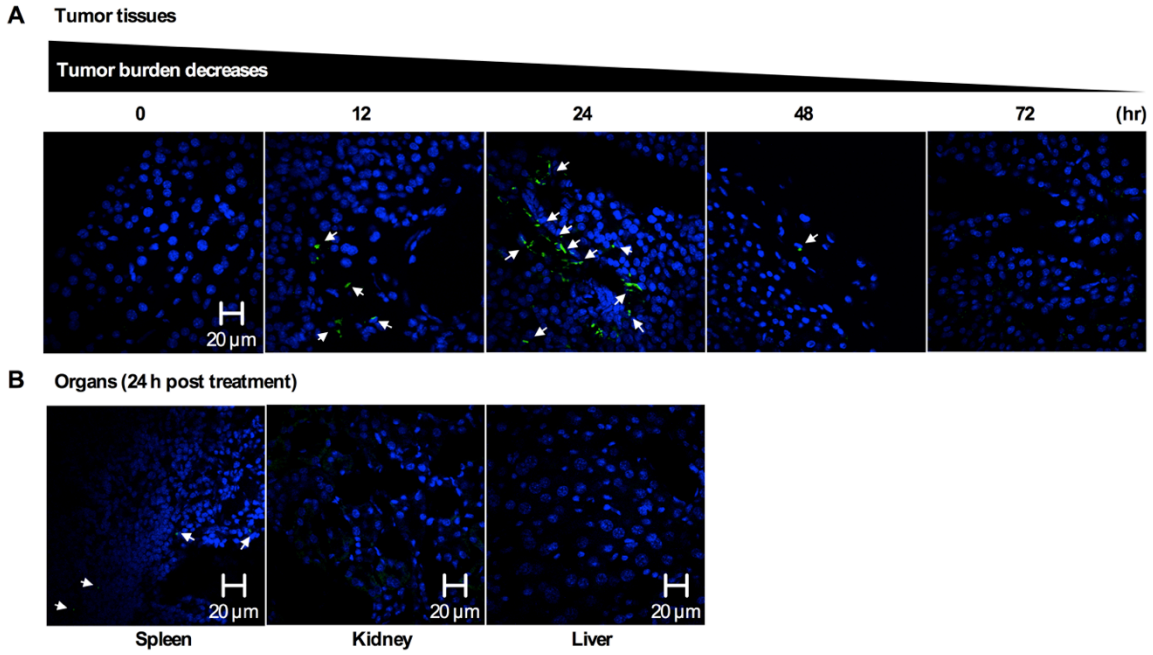

Figure 5.3. (A) Laser scanning confocal microscopic images (60x magnification) of apoptosis by TUNEL in resected ES-2-luc ovarian tumor tissue at 0, 12, 24, 48, and 72 hr post a single IV injection of PEG-*b*-PCL micelles carrying PTX, CYP, and GSP at 30, 30, and 30 mg/kg (B) Laser scanning confocal microscopic images (60x magnification) of apoptosis by TUNEL in resected spleen, kidney, and liver at 24 hr post a single IV injection of PEG-*b*-PCL micelles carrying PTX, CYP, and GSP at 30, 30, and 30 mg/kg. DNA fragmentation in apoptotic cells are in green, and nuclei of cells are in blue (DAPI).

5.3.4. Apoptosis-targeting efficacy of GFNFRLKAGAKIRFGS-PEG-*b*-PCL micelles carrying DiR *in vivo*

NIR fluorescence imaging of DiR delivered by either methoxy-PEG-*b*-PCL or apoptosis-targeting PEG-*b*-PCL micelles carrying DiR was observed longitudinally in groups of four animals (Figure 5.4). Subsequently, peritoneal dissemination of ES-2-luc tumor cells was monitored in identical animals, detecting bioluminescence signal over the peritoneal cavity. A group of animals was treated with PEG-*b*-PCL micelles carrying PTX, CYP, and GSP at 30, 30, and 30 mg/kg, respectively, (delivered IP on day 7 post ES-2-luc cell inoculation) followed by apoptosis-targeting PEG-*b*-PCL micelles carrying DiR at 100 nM (delivered IV on day 8); as shown on the right hand side in Figure 5.4 (an experimental group), whole-body bioluminescence of ES-2-luc tumor cells is shown along with the image of DiR delivered by apoptosis-targeting PEG-*b*-PCL micelles, shown in whole-body NIR fluorescence images at 24 hr after an IV injection of apoptosis-targeting PEG-*b*-PCL micelles carrying DiR. In a control group of animals treated with empty PEG-*b*-PCL micelles followed by methoxy-PEG-*b*-PCL micelles carrying DiR, the distribution of DiR in fluorescence images showed lower correspondence with the peritoneal dissemination of ES-2-luc tumor cells from bioluminescence images with the strongest fluorescence signal observed in liver (black arrows) of animals. Tumor tissues collected from an experimental group of animals were clearly color-coded in both bioluminescence and fluorescence images. Tumor tissues collected from a control group of animals lacked fluorescence in images. Additionally, it was confirmed by Fluobeam® 800, a portable hand-held 2-D NIR fluorescence imaging system that a visually palpable tumor tissue under white-light was also clearly illuminated in gray-scale NIR fluorescence images of animals

treated with apoptosis-targeting PEG-*b*-PCL micelles (an experimental group) after the NIR laser of Fluobeam® 800 was on (dotted circles); however, a palpable tumor tissue was not visible or distinguishable from normal tissues in NIR fluorescence images of animals in the control group under the laser of Fluobeam® 800.

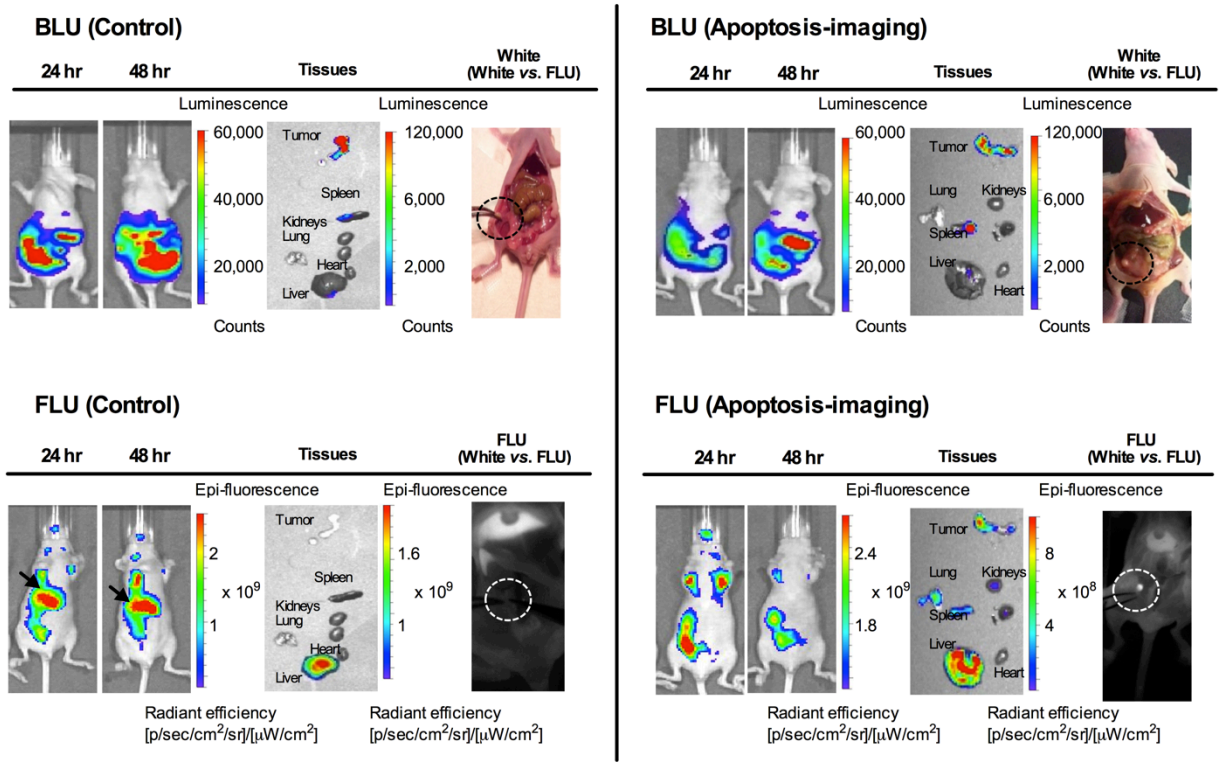

Figure 5.4. Assessment of apoptosis imaging *in vivo* and *ex vivo*: Whole-body and excised tissues in bioluminescence images of ES-2-luc-bearing mice and those in fluorescence images of same animals obtained with Xenogen IVIS® 200 Series. White-light *vs*. fluorescence imagings in midline incised ES-2-luc-bearing mice obtained with Fluobeam® 800. (A) Representative fluorescence and bioluminescence images of ES-2-luc-bearing mouse injected IP with empty PEG-*b*-PCL micelles followed by an IV injection of methoxy-PEG-*b*-PCL micelles carrying DiR at 250 mg/kg as a control (left hand side) and those of ES-2-luc-bearing xenograft model injected IP with PEG-*b*-PCL micelles carrying PTX, CYP, and GSP at 30, 30, and 30 mg/kg followed by an IV injection of PS-targeting PEG-*b*-PCL micelles carrying DiR at 250 μg/kg as an experimental group (right hand side) at 24 and 48 hr after termination of treatments.

From noninvasive bioluminescence imaging, quantitative BLI in ROI is presented longitudinally in Figure 5.5. Two days after termination of treatment, %BLI in ROI (%change in BLI of ROI starting at 6 hr after after an IV injection of apoptosis-targeting PEG-*b*-PCL micelles carrying DiR) increased rapidly up to *ca*. 60% but %FLI in ROI decreased to *ca*. -20% in control mice. In contrast, in the experimental group, %BLI in ROI decreased to *ca*. -50% but %FLI increased to *ca*. 20%.

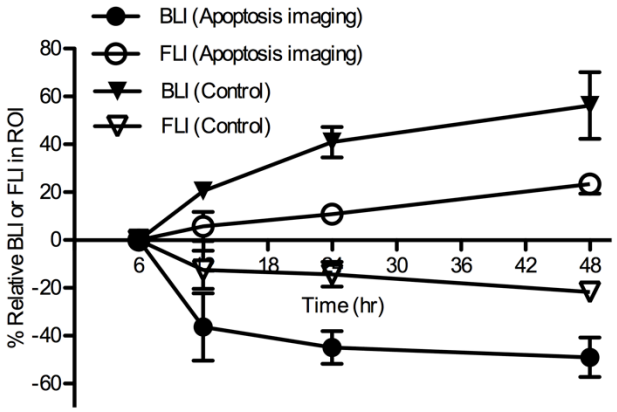

Figure 5.5. Relative BLI and FLI of ROIs in noninvasive whole-body images of ES-2-luc-bearing mouse in a time-dependent manner.

5.3.5. Real-time NIR fluorescence image-guided surgery in IP ovarian cancer model

ES-2-luc-bearing mice received an IP injection of either empty PEG-*b*-PCL micelles or PEG-*b*-PCL micelles carrying PTX, CYP, and GSP at 30, 30, and 30 mg/kg, respectively, on day 7, followed by a subsequent IV injection of either empty apoptosis-targeting PEG-*b*-PCL micelles or apoptosis-targeting PEG-*b*-PCL micelles carrying DiR on day 8 post IP cell inoculation. On day 9, all animals were sacrificed, and the abdominal cavity was opened. Surgical tumor resection of the visually palpable tumor-like tissues was performed under white-

light in control mice (traditional surgery). Resection of the FLU^+ tumor-like tissues was performed under real-time NIR guidance using the Fluobeam® 800 fluorescence imaging system (intraoperative fluorescence image-guided surgery). Bioluminescence images were obtained of mice before incision, mice after laparotomy incision, mice after debulking surgery, and of collected tumor-like tissues for a control group (n = 4) in Figure 5.6A; bioluminescence and fluorescence images of the same were for an experimental group (n = 4) in Figure 5.6B. Not all dissected tumor-like tissues by traditional surgery under white-light were bioluminescence-positive (LUC^+) tissues and only some of dissected tumor-like tissues were genuine luciferase-expressing tumor tissues. The large number of tumors left undissected in the carcass after surgical tumor resection under white-light is shown in Figure 5.6A. In contrast, most of tumor-like tissues dissected with the guidance of intraoperative NIR fluorescence imaging were LUC^+ and good correlation was observed between fluorescence and bioluminescence patterns in the collected tumor tissues (Figure 5.6B). Substantially smaller amounts of LUC^+ and FLU^+ tissues were left undissected in the carcass after real-time NIR image-guided surgery.

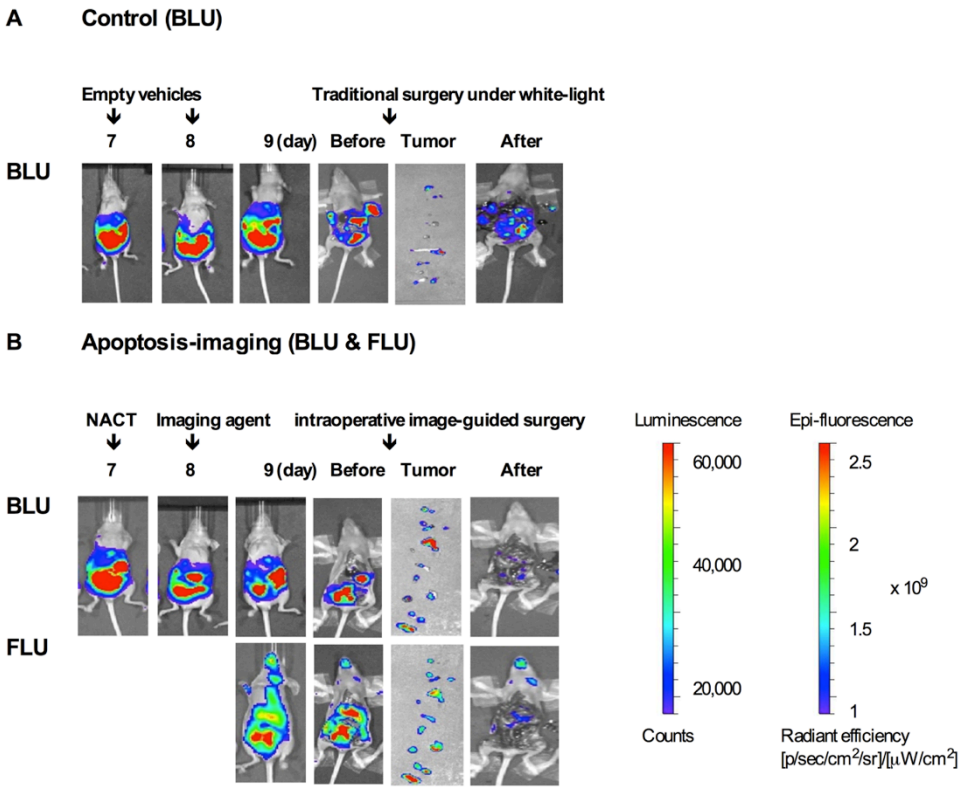

Figure 5.6. Assessment of intraoperative apoptosis imaging: Whole-body, excised tumor tissues, and carcass (before and after surgery) in bioluminescence and fluorescence images of four individual ES-2-luc-bearing xenograft animals obtained with Xenogen IVIS® 200 Series. (A) ES-2-luc-bearing mice injected IP with empty PEG-*b*-PCL micelles followed by empty apoptosis-targeting PEG-*b*-PCL micelles as a control. (B) ES-2-luc-bearing mice injected IP with PEG-*b*-PCL micelles with PTX, CYP, and GSP at 30, 30, and 30 mg/kg followed by an IV injection of PS-targeting PEG-*b*-PCL micelles carrying DiR at 250 μg/kg as an experimental group.

The surgical procedure guided by intraoperative grey-scale NIR fluorescence images using Fluobeam® 800 in ES-2-bearing animals (an experimental group) is shown in Figure 5.7; apoptosis-targeting PEG-*b*-PCL micelles carrying DiR allowed the detection of FLU^+ (white in color) large ovarian tumor tissues and FLU^+ ascites in open peritoneum, noting that BLU^+ cancer cells in ascites are also fluorescent. Following thorough exploration and surgical removal of large FLU^+ tumor tissues and FLU^+ ascites, smaller tumor nodules are visible for resection from

peritoneum. Representative intraoperative images obtained before, during, and after interval debulking surgery in ES-2-bearing animals in an experimental group are presented in Figure 8; FLU^{+} tissues located in pelvic area, caecum, skin, fallopian tube, and rectum were observed under Fluobeam® 800. Real-time NIR fluorescence imaging guidance permitted detection of tumors *ca*. 1 mm in diameter (Figures 5.7 and 5.8).

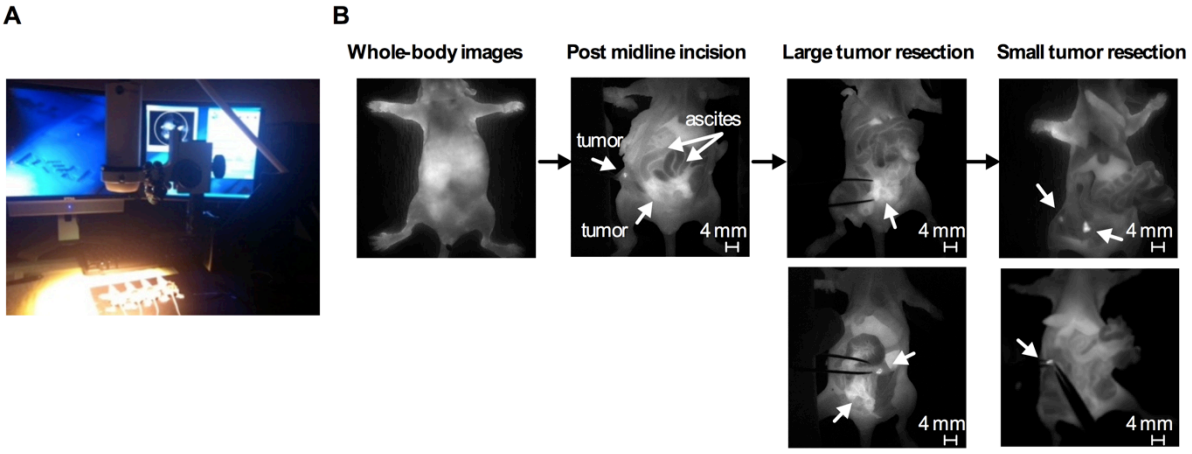

Figure 5.7. Surgical procedure of ES-2-luc bearing mice guided by intraoperative NIR fluorescence imaging of apoptosis. (A) Experimental conduct of animal surgery using Fluobeam®. (B) Fluorescence images of carcass of ES-2-luc-bearing mice captured by Fluobeam® during the peritoneal exploration and surgery.

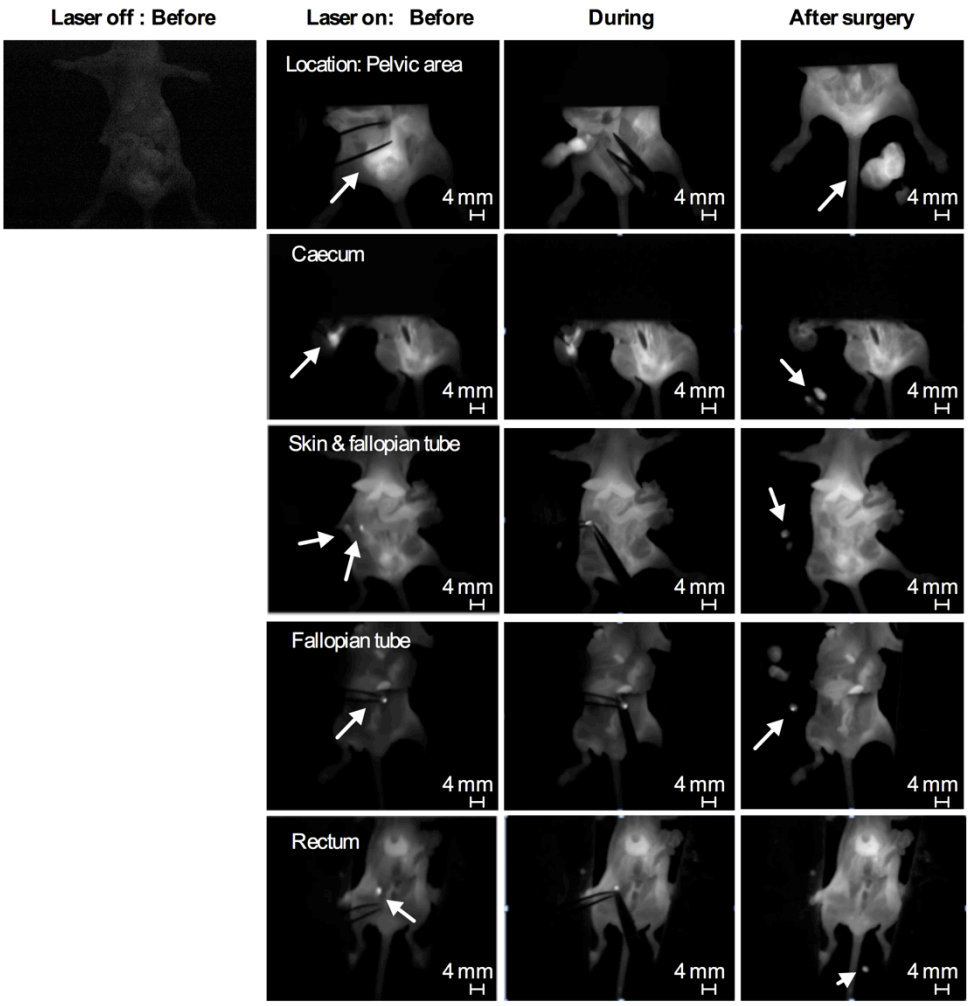

Figure 5.8. Fluorescence images of carcass of ES-2-luc-bearing mice at different surgical stages and locations obtained by Fluobeam®.

The amount of undissected Luc^+ tissues left in carcasses before and after interval debulking surgery was quantified, and the number of total resected tissues and the number of LUC^+ tissues were counted using visual observation and by bioluminescence imaging, respectively (Table 5.2). By comparing the number of LUC^+ tissues with the number of total

resected tissues, surgical accuracy could be estimated (equation 1: % no. of BLU^+ tissues / no. of total resected tissues). Following traditional surgery, 33.5 ± 16.6% of resected tissues were real LUC^+ tumor tissues. Guided by intraoperative NIR fluorescence images, 91.7 ± 8.6% of resected tissue were LUC^+ tumor tissues. Surgical accuracy was also assessed by estimating %BLI of dissected tumors (equation 2: [BLI of ROI in mid-line incised body "before" surgery – BLI of ROI in dissected body "after" surgery]) divided by BLI of ROI in mid-line incised body "before" surgery. Traditional surgery removed 27.5 ± 9.9% of LUC^+ tissues and intraoperative NIR fluorescence image guidance resected 88.6 ± 6.1% of LUC^+ tissues from ES-2-luc-bearing mice.

Group	% Accuracy		Average operation time (min)	PCI (BLI based)
	Equation 1 (*ex vivo* tissue-based)	Equation 2 (*ex vivo* carcass-based)		
Experimental	91.7 ± 8.6	88.6 ± 6.1	12.5 ± 2.0	6.8 ± 3.4
Control	33.5 ± 16.6	27.5 ±9.9	9.2 ± 1.3	26.5 ± 8.1

Table 5.2. Evaluation of apoptosis-targeted interval debulking surgery in ES-2-luc-bearing xenograft model.

Average duration of interval debulking surgery was 9.2 ± 1.3 min under white-light in traditional surgery and 12.5 ± 2.0 min using the intraoperative NIR fluorescence imaging guidance. The median PCI calculated using the scoring system shown in Figure 5.9 was 26.5 ± 8.1 after traditional surgery and 6.8 ± 3.4 after surgery guided by real-time NIR fluorescence images.

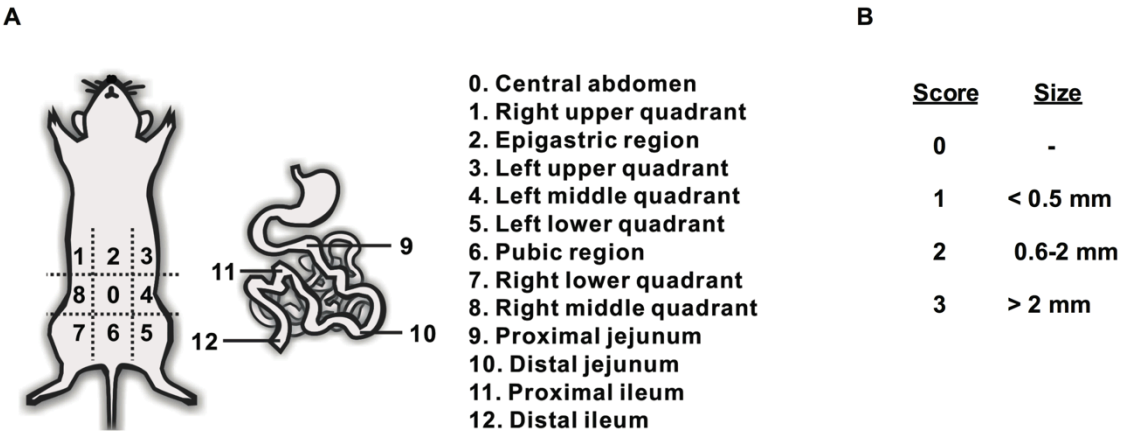

Figure 5.9. (A) Illustration of Peritoneal Cancer Index (PCI) by Sugarbaker, a composite score (0-3) of lesion size in abdomino-pelvic regions (0-12). (B) The scoring system of PCI adapted from Sugarbaker.

5.4. Discussion

In preclinical and clinical trials, there are four factors to consider in determining the success of intraoperative NIR image-guided surgery: (1) targeting agent, (2) disease type, (3) surgical intent, and (4) imaging equipment.[49] Our study demonstrated that a combined approach with IP NACT and real-time NIR fluorescence image-guided interval debulking surgery may represent an improved strategy for ovarian cancer, addressing the aforementioned four factors as follows. (1) Targeting agents: several NIR fluorescence probes and fluorescence agent-containing or -conjugated nanoparticles have been developed for a tumor-targeted imaging purposes, *eg*. Cy5-labeled RAFT-c(RGDfK)$_4$, Cy5.5-labled glycol chitosan nanoparticles, and GRGDS-PEG-*b*-PCL micelles containing DiI.[142, 144, 145] Selection of tumor targets in tumors impacts the surgical treatment because the surgeon completely relies on images to be visible in the surgical field. In this chapter, therapy-induced apoptosis was chosen as a target for

intraoperative NIR fluorescence imaging and a strategy of targeting apoptosis at tumor tissues using apoptosis-targeting peptide (GFNFRLKAGAKIRFGS)-conjugated PEG-*b*-PCL micelles containing the NIR fluorescence probe DiR was validated in a preclinical mouse model of ovarian cancer debulking. Li and colleagues identified a 14-mer peptide, FNFRLKAGAKIRFG, which demonstrated nanomolar binding affinity to PS in apoptotic tumors for therapy-induced apoptosis imaging purpose.[25] In our study, a FNFRLKAGAKIRFG-containing linear peptide, GFNFRLKAGAKIRFGS (G and S were added to enhance serum stability of FNFRLKAGAKIRFG residues after conjugation), was conjugated on the surface of aldehyde-PEG-*b*-PCL micelles for serum stability and apoptosis-targeted delivery of a NIR fluorescence imaging probe. DiR-incorporated GFNFRLKAGAKIRFGS-PEG-*b*-PCL micelles (named as apoptosis-targeting PEG-*b*-PCL micelles) prepared by a solvent evaporation method obtained similar physical characteristics of DiR-incorporated methoxy-PEG-*b*-PCL micelles, *eg*. DiR loading capacity at *ca.* 2% and the $t_{1/2}$ value for *in vitro* DiR release at *ca.* 2 hr, but 1.8-fold larger z-average diameter of apoptosis-targeting PEG-*b*-PCL micelles carrying DiR at *ca.* 80 nm. Despite their slightly enlarged particle size, there were no signs of uneven size distribution or aggregation of apoptosis-targeting PEG-*b*-PCL micelles in aqueous solution (PDI 0.1) as shown in Table 5.1, enabling safe IV injection for *in vivo* studies without rapid renal clearance (typically problematic for a low molecular weight peptides) or severe hepatic uptake of aggregates. GFNFRLKAGAKIRFGS, maintained PS-selective binding affinity after decorating the surface of aldehyde-PEG-*b*-PCL micelles and apoptosis-targeting PEG-*b*-PCL micelles adsorbed selectively onto PS-coated wells and apoptosis-induced ES-2 ovarian tumor spheroids *in vitro* (Figure 5.2). Apoptosis-targeting PEG-*b*-PCL micelles preferentially delivered DiR

molecules preferably to apoptosis-induced ES-2-luc ovarian tumor spheroids with 2.4-fold increased DiR uptake over pre-saturated ES-2-luc ovarian tumor spheroids. Apoptosis-targeting PEG-*b*-PCL micelles carrying DiR have potential as a promising NIR fluorescence imaging agent for intraoperative surgical guidance in oncology, as they satisfy the major needs of NIR fluorescence imaging agents (facile preparation, the ability to be injectable as nanomaterials, enhanced aqueous solubility of highly lipophilic imaging probe, strong light absorbance in the NIR window, and most importantly, active tumor targeting).

(2) Disease type: a tandem of PEG-*b*-PCL micelles, PEG-*b*-PCL micelles carrying PTX, CYP, and GSP for NACT-induced apoptosis and apoptosis-targeting PEG-*b*-PCL micelles carrying DiR for optical imaging purpose, was tested in metastatic human ovarian cancer (ES-2-luc)-bearing animal model categorized as undifferentiated type in ovarian carcinomas. The undifferentiated carcinoma is defined by the absence of distinctive histological features or only small foci of differentiation, and is known as clinically aggressive neoplasm accounting for 4-5% of all primary ovarian malignancies.[127, 146] ES-2-luc cancer cells inoculated in the peritoneal cavity tend to widely spread in the abdominal peritoneum and rapidly invade ovaries, fallopian tubes, pelvic structures (uterus, bladder, and rectum), and intestines leading to 100% animal death within 4 weeks after IP inoculation.[141] Due to the aggressive nature of peritoneal malignancies, successful treatment of metastatic peritoneal ovarian cancer is challenging and requires aggressive debulking surgery.[132]

(3) Surgical intent: because of the number and broad distribution of tumors, surgical resection of aggressively metastatic ovarian cancer requires a large incision, thorough explorations, and precise tumor resection with minimization of injury to involved organs. It is

therefore important to clearly delineate tumor margins and differentiate highly undistinguishable lesions from normal tissues. Confocal microscopic images of collected tissues demonstrated that a single IP injection of PEG-*b*-PCL micelles carrying PTX, CYP, and GSP at 30, 30, and 30 mg/kg, respectively, in ES-2-luc-bearing animals increased the level of apoptosis in tumor tissues over time, reaching to the peak apoptosis level on day 1 post drug treatment. The subsequent decrease in the number of DNA fragments was presumably due to DNA fragments of apoptotic cells engulfed by macrophages. No apoptosis was observed in the kidney and liver but, a few DNA fragments of apoptotic cells were found in the spleen on day 1: as ES-2-luc ovarian cancer cells often travel to spleen and pancreas, it is possible that DNA fragments might be induced in metastatic tumor tissues residing in spleen. When apoptosis induction was optimized at 24 hr after an IP injection of PEG-*b*-PCL micelles carrying PTX, CYP, and GSP in ES-2-luc-bearing animals, PEG-*b*-PCL micelles carrying DiR were injected *via* IV route. Some correlation was observed between NIR fluorescence signal (from DiR molecules accumulating at tumor tissues) and BLI of tumor tissues on bioluminescence imaging 24 hr after an IV injection of apoptosis-targeting PEG-*b*-PCL micelles carrying DiR (Figure 5.4). However, methoxy-PEG-*b*-PCL micelles carrying DiR were observed mostly in the liver, indicating that passive targeting by the EPR effect was not sufficient to deliver DiR-incorporated methoxy-PEG-*b*-PCL micelles to metastatic tumor tissues disseminated in the peritoneal cavity. Moreover, a tumor priming strategy achieved by IP injection of PEG-*b*-PCL micelles carrying PTX, CYP, and GSP followed by an IV injection of methoxy-PEG-*b*-PCL micelles carrying DiR, was also insufficient to deliver DiR-incorporated methoxy-PEG-*b*-PCL micelles to metastatic tumor tissues in our ES-2-luc-bearing xenograft model (data not shown). As metastatic ovarian tumor tissues are deficient

in blood supply and spread discontiguously along the peritoneal surfaces, microenvironment of metastatic ovarian tumors may impede delivery of agents by the EPR effect. The present study demonstrates that apoptosis-targeting PEG-*b*-PCL micelles carrying DiR improved delivery of DiR molecules to metastatic ovarian tumor tissues with a 1.5-fold stronger FLI in collected tumor tissues compared to passively-targeted DiR using methoxy-PEG-*b*-PCL micelles at 48 hr after IV injection. To illustrate the potential utility of our observations, small tumor tissues that were routinely left undissected near the left fallopian tube that were not visible by DiR-incorporated methoxy-PEG-*b*-PCL micelles under Fluobeam® 800, were clearly visible by apoptosis-targeting PEG-*b*-PCL micelles carrying DiR under the same condition with Fluobeam® 800 (Figure 5.4). In this study, the surgical intention for undifferentiated ovarian cancer at advanced stage is certainly to eradicate ovarian tumors after complete interval debulking surgery with minimum residual tumors (< 1 cm in size of residual tumors) guided by intraoperative NIR fluorescence imaging.[130]

(4) Imaging equipment: Fluobeam® 800 provided real-time gray-scale images after NIR excitation of surgical targets and allowed for acquisition of both static and real-time images of objects (Figures 5.7 and 5.8). The real-time feedback of NIR fluorescence images during operative exploration can maximize the practical benefit of NIR fluorescence imaging compared to wide-field whole-body epifluorescence illumination approach by minimizing concerns regarding depth of detection and high autofluorescence from skin, as a large abdominal incision is necessary for the surgical process in peritoneal malignancies. In the experimental group, IP NACT followed by interval debulking surgery with a support of real-time NIR fluorescence images, resulted in *ca.* 90% debulking of ES-2-luc tumor tissue, whereas *ca.* 30% of ES-2-luc

tumor tissues were removed in the control group of traditional debulking surgery (IP and IV injections of empty vehicles) under white-light (Figures 5.6-5.9 and Table 5.2). The surgical superiority of real-time NIR fluorescence image-guided surgery was also demonstrated using the PCI, an indicator of distribution and size of residual tumors, adapted from Sugarbaker (7 *vs.* 27).[132] A modified PCI scoring system was applied in our study to translate the scoring system from human to mouse scale. Unlike results reported by Coll and colleagues, in which the operation time of surgical tumor resection was reduced with the use of Fluobeam® 800 in peritoneal adenocarcinoma-bearing mouse model, intraoperative fluorescence NIR image-guidance did not reduce the duration of surgery compared to traditional white-light surgery (13 min *vs.* 9 min). In our experience, it was evident that the additional tumors visualized by real-time NIR fluorescence (not seen under white light) necessitated longer operation time, resulting in more optical tumor debulking. Surprisingly, real-time videos recorded by Fluobeam® 800 show that the NIR fluorescence signal of DiR molecules at tumor tissues permitted identification of tumors as small as 1 mm in diameter and as large as 5 mm in diameter. The heightened sensitive tumor detection could greatly improve the efficacy of surgical therapy for peritoneal metastases, as optical tumor debulking ideally requires minimum residual tumors < 1cm.[33, 48] It is expected that improved detection of submillimeter sized-tumor tissues could enhance the delivery of surgical therapy and ultimately improve survival.[48]

5.5. Conclusion

Optical NIR fluorescence imaging has shown potential for intraoperative surgical guidance in ovarian cancer beyond preoperative radiological imaging and visual inspection or

palpation of tumors under white-light illumination. A successful strategy of ovarian cancer management requires a combination of aggressive surgical therapy with chemotherapy.

In this chapter, a treatment strategy coupling NACT and an interval debulking surgery guided by intraoperative apoptosis-targeted NIR fluorescence imaging using a tandem of administrated PEG-*b*-PCL micelles resulted in induction of apoptosis in tumor tissues, accurate delineation of tumor tissues in NIR fluorescence images, and ultimately, improved surgical accuracy and outcome in an ES-2-luc-bearing xenograft model of ovarian cancer. The unique approach employing PEG-*b*-PCL micelles may be seamlessly integrated into ovarian cancer surgery, enhancing visualization of tumor tissues and providing valuable guidance using intraoperative NIR fluorescence imaging for surgical oncology.

6 General discussion and conclusions

6.1. Primary findings and conclusions

In this dissertation, three strategies, passive targeting (enhanced permeability and retention, EPR), tumor priming, and active targeting, used in surgical oncology aimed at tumor visualization were investigated.

Poly(ethylene glycol)-*block*-poly(ε-caprolactone) (PEG-*b*-PCL) micelles carrying DiR (1,1'-dioctadecyltetramethyl indotricarbocyanine iodide) passively targeted LS180 solid colon tumors by the EPR effect showed a high tumor-to-background ratio in *ex vivo* fluorescence images.

The major drawback of micellar drug delivery solely relying on the EPR effect is that intratumoral barriers drawn by complexity and heterogeneity of cancers, *i.e*. high cancer cell density, increased interstitial pressure, and uneven angiogenesis hinder the intratumoral penetration of polymeric micelles. This issue can be overcome simply by pretreating solid tumors with potent cytotoxic agents prior to delivery of polymeric micelles carrying a near-infrared (NIR) fluorophore. This tumor priming process can reduce tumor cell density, expand interstitial space, and induce apoptosis. As a result, tumor uptake of PEG-*b*-PCL micelles carrying DiR into LS180 solid tumors could be facilitated with enhanced tumor-to-background ratio in *ex vivo* fluorescence images.

To consider a clinically translational approach in surgical oncology, highly invasive and metastatic intraperitoneal (IP) ovarian cancer xenograft models were used. This is because extensive debulking surgery aiming at maximal surgical tumor removal and the minimal residual tumor nodules is the most critical procedure in treating peritoneally spread cancers. The EPR and tumor priming effects seemed to be promising strategies for solid tumor painting but their tumor

visualization efficiencies in highly metastatic, invasive, and undifferentiated IP ovarian cancer model are questionable.

A 2-step strategy using a tandem of polymeric micelles, a neoadjuvant chemotherapy followed by apoptosis-targeted optical imaging, debulked metastatic ovarian tumor nodules with no notable toxicity, induced the optimum apoptosis at tumor tissues, and painted apoptotic tumors with a heightened fluorescence intensity. Intraoperative apoptosis-targeted optical imaging improved accuracy of surgical tumor resection, provided useful guidance, allowed detailed surgery, and decreased residual tumor tissues in the metastatic IP ovarian cancer model.

The details of the major findings in chapters 2-5 are summarized as follows.

6.1.1 Passive delivery of PEG-*b*-PCL micelles carrying DiR for solid tumor delineation

DiR was successfully incorporated into PEG-*b*-PCL micelles by a simple nano-precipitation method. The average diameter of DiR-loaded PEG-*b*-PCL micelles was about 30-50 nm. The photophysical state of DiR was manipulated by controlling the occupancy of micelles with DiR molecules: PEG-*b*-PCL micelles highly occupied by DiR emitted weak fluorescence as DiR molecules existed in a self-quenched state in the core of PEG-*b*-PCL micelles, due to the close proximity of DiR molecules and their aggregate formation. At low occupancy, DiR molecules existed in a nonquenched state, widely dispersed in the cores of PEG-*b*-PCL micelles and emitted strong fluorescence. It was noticed that *in vitro* and *in vivo* release kinetics of DiR molecules from PEG-*b*-PCL micelles were different depending on the states of DiR in PEG-*b*-PCL micelles: self-quenched DiR in PEG-*b*-PCL micelles showed a gradual increase of fluorescence intensity (FLI) over time whereas nonquenched DiR in PEG-*b*-PCL

micelles showed the rapid onset of FLI at early time points post IV administration and gradually lost FLI. Although kinetics of *in vivo* distribution of DiR in the LS180 colon cancer-bearing xenograft model depended on the photophysical properties of DiR in PEG-*b*-PCL micelles, we obtained equal tumor selectivity indicated by tumor-to-muscle ratios, *ca*. 2 from *in vivo* and *ca*. 30-40 from *ex vivo* images. Importantly, we found the potential of passively delivered PEG-*b*-PCL micelles carrying DiR in surgical oncology as we were able to detect tumor margins left undissected in fluorescence imaging after traditional surgery by visual observation and palpation in the LS180 colon cancer-bearing xenograft model.

6.1.2. Enhanced solid tumor visualization by tumor priming effect

The "tumor priming effect" was applied to overcome tumor penetration issues caused by high cancer cell density, increased interstitial pressure, and uneven angiogenesis. The tumor priming effect was planned with a 2-step strategy. (1) A single intravenous (IV) injection of poly(ethylene glycol)-*block*-poly($_{D,L}$-lactic acid) (PEG-*b*-PLA) micelles carrying paclitaxel (PTX), 17-allylamino-17-demethoxygeldanamycin (17-AAG), and rapamycin (RAPA) at 60, 60, and 30 mg/kg, respectively, induced apoptosis at LS180 solid tumors and elicited a 1.6-fold reduction in tumor volume with low acute toxicity. (2) PEG-*b*-PCL micelles carrying DiR were IV administrated in LS180 colon cancer-bearing xenograft model to visualize LS180 solid tumors.

The tumor priming effect obtained by PEG-*b*-PLA micelles promoted the delivery of PEG-*b*-PCL micelles carrying DiR into solid tumors, resulting in a heightened NIR optical signal for better tumor delineation with the tumor-to-muscle ratio of 149±13 in collected tissue.

Fluorescence images of midline-incised animals also proved that the tumor priming effect obtained by PEG-*b*-PLA micelles containing PTX, 17-AAG, and RAPA uniformly visualized LS180 solid tumors with the strongest fluorescence signal. In contrast, DiR molecules visualized non-primed LS180 solid tumors with the weak fluorescence signal and those unevenly visualized LS180 solid tumors primed by PTX-incorporated PEG-*b*-PLA micelles with the strongest signals on the rim and the gradually weaker signals toward the center of tumors. Thus, a tandem of PEG-*b*-PLA carrying PTX/17-AAG/RAPA and PEG-*b*-PCL micelles carrying DiR was used for effective tumor debulking, heightened tumor priming, and enhanced NIR optical imaging of LS 180 solid tumors. One limitation of this work was the use of a subcutaneous xenograft model rather than a xenograft model undergoing metastases that is clinically relevant.

6.1.3. PEG-*b*-PCL micelles carrying PTX, CYP, and GSP for neoadjuvant chemotherapy before debulking surgery in IP metastatic ovarian cancer model

Polymeric micelles for effective neoadjuvant ovarian chemotherapy were developed before tumor debulking surgery in an IP metastatic ovarian cancer model, the ES-2-luc ovarian cancer (undifferentiated adenocarcinoma)-bearing xenograft model. PEG-*b*-PCL micelles prepared by a solvent evaporation technique had a good capacity for paclitaxel (PTX), cyclopamine (CYP), and gossypol (GSP), *ca*. 9.4%, resulting in multiple drug solubilization at 18 mg/mL, *ca*. 6.2 mg/mL for each anticancer agent. PEG-*b*-PCL micelles were obtained with z-average diameters at *ca*. 80 nm, regardless of drug compositions in PEG-*b*-PCL micelles. PEG-*b*-PCL micelles carrying PTX/CYP/GSP at 1000 nM showed a unique anticancer effect on ES-2-luc ovarian cancer spheroids *in vitro*: PEG-*b*-PCL micelles carrying PTX/CYP/GSP dissembled

ES-2-luc spheroids into smaller cellular aggregates loosing spherical integrity, whereas ES-2-luc spheroids stayed intact after treatment with PTX, but reduced growth of tumor spheroids, presumably by the action of proliferating ES-2-luc cells in the periphery. It was speculated that disaggregation of ES-2-luc spheroids is induced by synergistic mechanisms: inhibition of Hh signaling by CYP possibly reversed PTX resistance, facilitating the penetration of PTX into spheroids, and GSP simultaneously augmented apoptosis to make spherical integrity vulnerable.

Both bioluminescence imaging and microPET/CT imaging also proved that IP injected PEG-*b*-PCL micelles carrying PTX, CYP, and GSP at 30, 30, and 30 mg/kg, respectively, have potent antitumor activity in metastatic ES-2-luc xenograft models. At 21 days (7 days post cessation of q7x3 treatment), the %BLI value (indicating ES-2-luc tumor progression) for PEG-*b*-PCL micelles carrying PTX/CYP/GSP was 11-fold and 4-fold less than the vehicle control and PEG-*b*-PCL micelles carrying PTX, respectively. Importantly, 50% of animals treated with PEG-*b*-PCL micelles carrying PTX/CYP/GSP survived for 46 days post cell inoculation, whereas 100% of animals treated with vehicle control and PEG-*b*-PCL micelles carrying PTX died within 27 and 35 days, respectively. Similar patterns of potent antitumor activity and prolonged survival of PEG-*b*-PCL micelles carrying PTX/CYP/GSP were observed in an SKOV-3-luc ovarian cancer (serous adenocarcinoma)-bearing xenograft model.

6.1.4. Polymeric micelles for apoptosis-targeted optical imaging of metastatic ovarian cancer and intraoperative surgical guidance

Apoptosis-targeting PEG-*b*-PCL (GFNFRLKAGAKIRFGS-PEG-*b*-PCL) micelles carrying DiR with a z-average diameter of 80 nm showed PS- and apoptosis-specific binding

affinities *in vitro*: DiR delivered by apoptosis-targeting PEG-*b*-PCL micelles showed *ca*. 2-fold stronger FLI in PS-coated wells over PC-coated wells, and DiR delivered by apoptosis-targeting PEG-*b*-PCL micelles also presented *ca*. 2-fold stronger FLI in primed ES-2-luc ovarian cancer spheroids (primed by PEG-*b*-PCL micelles carrying PTX/CYP/GSP) than FLI from DiR delivered by non-targeting PEG-*b*-PCL micelles.

Actively targeted apoptosis imaging was obtained *in vivo* by a 2-step strategy in the ES-2-luc ovarian cancer model. In the first step, IP administrated PEG-*b*-PCL micelles carrying PTX/CYP/GSP at 30/30/30 mg/kg debulked tumors and induced apoptosis with optimum apoptosis level in tumors at 24 hr post injection. In the second step, taken 24 hr after the first step, apoptosis-targeting PEG-*b*-PCL micelles carrying DiR were IV injected.

Surgical tumor resection was conducted in a control group for traditional surgery under white-light (IP empty PEG-*b*-PCL micelles followed by IV empty PEG-*b*-PCL micelles) and an experimental group for surgery under intraoperative surgical guidance using the Fluobeam® 800, NIR imaging system (IP PEG-*b*-PCL micelles carrying PTX/CYP/GSP followed by IV apoptosis-targeting PEG-*b*-PCL micelles carrying DiR). As a result, not all dissected tumor-like tissues by traditional surgery were LUC^+, and only some of the dissected tumor-like tissues were genuine luciferase-expressing tumor tissues. A large number of tumors were left undissected in the carcass after surgery under white-light. In contrast, most of tumor-like tissues dissected with the guidance of intraoperative optical imaging were LUC^+ and there was a good correlation between fluorescence and bioluminescence patterns in *ex vivo* images. Substantially smaller amounts of LUC^+ and FLU^+ tissues were left undissected in the carcass after intraoperative image-guided surgery. Intraoperative optical imaging surprisingly permitted identification of

tumor nodules as small as 1 mm. Surgical accuracy was significantly higher in an experimental group under intraoperative surgical guidance, compared to that of a control group under traditional surgery (*ca.* 90% *vs. ca*. 30%). Operation time was *ca.* 3 min longer under the intraoperative surgical guidance, because there was more opportunity to explore suspicious small cancerous tissues visualized under the Fluobeam® 800. PCI (peritoneal cancer index) was substantially lower for the intraoperative surgical guidance group (*ca.* 7 *vs. ca.* 27), indicating less residual LUC^+ tumor tissues left undissected in the carcass.

The unique approach of employing a tandem of PEG-*b*-PCL micelles may be seamlessly integrated into ovarian cancer surgery, enhancing visualization of metastatic tumor tissues and providing valuable guidance using intraoperative NIR fluorescence imaging.

6.2. Suggestions for future research

6.2.1. Alternatives for neoadjuvant chemotherapy

A carboplatin-PTX combination is, by now, the standard first-line treatment of ovarian cancer.[147] The evolution of ovarian cancer therapy over the last 50 years has shown that platinum-based therapy (cyclophosphamide + alkeran radiotherapy in 1960's, cisplatin + doxorubicin in late 1970's, carboplatin + cyclophosphamid or cisplatin + taxane in early 2000's, and carboplatin + taxane or carboplatin + Doxil in 2010-present) remains the standard of care.[148] However, when choosing an optimal treatment for ovarian cancer patients, a standard regimen cannot be generalized due to the numerous subtypes of ovarian carcinoma (prevalence, morphology, immunophenotype, and genotype).[149] In particular, neoadjuvant chemotherapy (NACT) in women with stage III/IV ovarian cancer (bulky and widespread disease) should be

well tailored to the patient, taking resectability, age, histology, stage, and performance status into account.[150]

In this dissertation (chapter 4), we found that a concurrent IP delivery of PTX, CYP, and GSP using PEG-*b*-PCL micelles (q7d x 3 dosing schedule) was highly effective in metastatic ES-2-luc and SKOV-3-luc ovarian cancers (ES-2: undifferentiated adenocarcinoma, highly aggressive/invasive subtype, SKOV-3: serous adenocarcinoma, moderate-grade subtype),[129] eradicating peritoneal tumors and ascites and prolonging survival. Although we observed striking results in treating two different subtypes of ovarian cancer, we still believe that there might be more effective combinations to treat ovarian cancer covering a broader range of subtypes.

Based on recent clinical and molecular investigations, around 70% of ovarian cancers show PI3K signaling activation.[151] Thus, efforts for developing biomarkers measuring PI3K activity have been made. Moreover, it has been hypothesized that PI3K/Akt pathway inhibitors combined with platinum and taxane analogues may be beneficial in ovarian cancer patients because PI3K/Akt pathway activation has been revealed to be involved in resistance to platinum and taxanes. For example, combining wortmanin, an irreversible inhibitor of PI3K, with paclitaxel and carboplatin may be a good alternative for treating ovarian cancer, considering both clinical evolution of ovarian chemotherapy and molecular investigations. It is assumed that toxicity caused by IV administration of potent multi-drug combinations may be minimal in application of polymeric micelles by passively targeting the diseased site and gradually releasing payloads specifically to targets.

6.2.2. Improving stability, loading capacity, and targeting of polymeric micelles carrying NIR contrast agents

In chapter 5, we prepared PEG-*b*-PCL (M_n of PEG = 5,000 g/mol, M_n of PCL = 5,000 g/mol) micelles decorated with GFNFRLKAGAKIRFGS to actively deliver DiR to apoptotic tumors. The characterization result showed that 50% of DiR molecules were released from apoptosis-targeting PEG-*b*-PCL micelles within 2 hr *in vitro*, and loading efficiency of DiR was 2%. We can simply improve release kinetics of DiR by occupying apoptosis-targeting PEG-*b*-PCL micelles with larger amounts of DiR. A large number of DiR molecules in the core of apoptosis-targeting PEG-*b*-PCL micelles formed aggregates, existing in self-quenched state (weak in FLI), as shown in chapter 2. DiR molecules in aggregates may show slower release kinetics, being delayed by the dissociation process from aggregates to monomers upon leakage of micelles. Loading efficiency can be increased by the use of block copolymers with longer hydrophobic blocks. With respect to the micelle formation (the hydrophobic core serves as a reservoir to increase solubility of hydrophobic components), longer hydrophobic blocks can create more space in the core of micelles, permitting an increased loading of payloads.

Sustained release can be achieved by preparing physically stable micelles consisting of linkage of polymer-payload. Strategies for sustained release for polymeric micelles include cross-linking, conjugation, and temperature- or pH-responsive formulations.[152] In particular, cross-linking or conjugation strategies can improve stability and release kinetics of micelles carrying NIR contrast agents in the blood stream, and they can increase the loading efficiency of payloads.[153] Furthermore, with some modification of polymeric micelles, as mentioned in chapter 1, polymeric micelles can be adopted to release NIR contrast agents under certain

conditions, such as apoptosis (activated by casepase-3 and -7) or an invasive condition (activated by matrix metalloproteinase, MMP).[44]

Tumor targeting property may be improved by the use of different targeting moieties. As there is no universal target for all types of cancers, a wise selection of targeting moiety is critical to excel disease-specific targeting. In chapter 5 of this dissertation, apoptosis-targeting peptide, GFNFRLKAGAKIRFGS, was used to deliver payloads to therapy-induced apoptotic ovarian tumor tissues. Targeting of apoptotic ovarian tumors can be even better facilitated by decorating polymeric micelles with apoptosis-specific peptides having higher binding affinity to apoptotic cells/tissues, probably selected by using the phage display technique. Other target alternatives, other than apoptosis, can be the EGF receptor and the folate receptor α expressed on ovarian cancer cells.[154, 155] Although investigators have been introducing successful applications and results of ovarian cancer targeting, targeting EGF receptor and folate receptor α, neither can target broadly-ranged subtypes of ovarian cancers. The expression rate of receptors depending on age, histology, stage and treatment history of patients should be clearly investigated.

6.2.3. Survival study

In chapter 5, it was shown that a treatment strategy coupling NACT and an interval debulking surgery guided by intraoperative apoptosis-targeted optical imaging resulted in improved surgical accuracy and outcome in an ES-2-luc-bearing xenograft model of ovarian cancer. Surgery was performed in a sacrificed ES-2-luc-bearing mouse model to evaluate the efficacy of the treatment strategy. However, surgical accuracy and outcome must be validated by long-term survival of animals after surgical tumor resection. It is assumed that animals bearing

less residual tumor tissues after surgical resection guided by intraoperative optical imaging (4-fold less PCI than traditional white-light surgery) will show extended survival. Surgery will have to be performed with the intention of maximally removing as many tumor deposits as possible, under either conventional white-light or using intraoperative optical fluorescence image-guided surgery in ovarian cancer-bearing rats. After surgery and exploration of residual tumors, the abdomen will be sutured and closed, and animals will then recover, allowing measurement of survival duration as an evaluation of surgical outcome. It will be also worth comparing different subtypes of ovarian cancer rat models (one bearing aggressive and widely invasive metastases at late stages and another bearing local moderate-grade metastases at early stages) to monitor how the 2-step treatment strategy can affect the survival rate of animals given different disease stages and aggressiveness.

6.3. Final remarks

To summarize, optical NIR fluorescence imaging has shown a potential for intraoperative surgical guidance in ovarian cancer beyond preoperative radiological imaging and visual inspection or palpation of tumors. PEG-*b*-PCL micelles carrying DiR passively targeted solid colon tumors with high tumor-to-background ratio in fluorescence images by the EPR effect. The tumor priming effect debulked tumors, induced apoptosis, and, as a result, facilitated tumor uptake of PEG-*b*-PCL micelles carrying DiR into solid colon tumors with improved tumor-to-background ratio in fluorescence images. A 2-step treatment strategy, NACT followed by apoptosis-targeting PEG-*b*-PCL micelles carrying DiR, debulked tumors, induced apoptosis, and provided real-time NIR fluorescence imaging with heightened tumor visualization in the ES-2-

luc-bearing metastatic ovarian cancer model. In turn, intraoperative optical imaging provided detailed surgical guidance, increased surgical accuracy, and decreased residual tumor tissues in the ES-2-luc-bearing metastatic ovarian cancer model.

Appendix

Evaluation of Commercially Available NIR Imaging Agents for Supporting Chapter 5

S1. Introduction

In chapter 5, it has been concluded that a 2-step treatment strategy coupling neoadjuvant chemotherapy (NACT) and intraperitoneal (IP) surgery guided by intraoperative apoptosis-targeted imaging, using (1) poly(ethylene glycol)-*block*-poly(ε-caprolactone) (PEG-*b*-PCL) micelles carrying paclitaxel (PTX), cyclopamine (CYP), and gossypol (GSP) and (2) GFNFRLKAGAKIRFGS-PEG-*b*-PCL micelles carrying DiR (1,1'-dioctadecyltetramethyl indotricarbocyanine iodide), facilitated visualization of IP metastatic ovarian tumor tissues in fluorescence imaging, enhanced surgical accuracy, and resulted in improved surgical outcomes in an ES-2-luc-bearing xenograft model.

There are several NIR (near-infrared) fluorescence imaging agents commercially available for research purposes that permit visualization of primary tumor tissues in murine xenograft models. In this supplementary chapter, we validated the tumor delineation efficiency of three commercially available NIR fluorescence imaging agents (AnnexinVivo^{TM}750, IntegriSense^{TM}750 and MMPSense^{TM}750Fast) in an ES-2-luc IP metastatic ovarian cancer model. Although tumor-targeting mechanisms of NIR fluorescence imaging agents used for the study (GFNFRLKAGAKIRFGS-PEG-*b*-PCL micelles carrying DiR (chapter 5), AnnexinVivo^{TM}750, IntegriSense^{TM}750 and MMPSense^{TM}750Fast) are not identical or suitable for direct comparison, it is worth monitoring differences between GFNFRLKAGAKIRFGS-PEG-*b*-PCL micelles

carrying DiR and commercially available NIR fluorescence imaging agents for effectiveness of tumor delineation.

S2. Materials and methods

S2.1. AnnexinVivo^{TM}750

AnnexinVivo^{TM}750 (MW 35,000 g/mol, PerkinElmer Inc., Boston, MA) is a targeted fluorescence imaging agent comprising a selective protein, Annexin A5 and an NIR fluorophore (λ_{ex} = 755 nm, λ_{em} = 772 nm). AnnexinVivo^{TM}750 is developed to visualize phosphatidylserine (PS) exposed on the outer leaflet of the cell membrane lipid bilayer during the early stage of apoptosis. AnnexinVivo^{TM}750 is supplied in a solution of 25 mM HEPES/NaOH, 140 mM NaCl, pH 7.4, and the recommended intravenous (IV) dose per mouse is 100 μL. *In vivo* imaging of animals at 2 hr post IV administration is recommended in general, and AnnexinVivo^{TM}750 clears from tissues < 3 days post IV injection.

In this experiment, ES-2-luc-bearing xenograft models (7 days post intrraperitoneal (IP) cell inoculation) were IP administrated with PEG-*b*-PCL micelles carrying PTX/CYP/GSP at 30/30/30 mg/kg and 24 hr later, animals were IV injected with100 μL of AnnexinVivo^{TM}750. Whole-body fluorescence and bioluminescence images were obtained 0.5, 12, 24, and 48 hr post AnnexinVivo^{TM}750 injection, using Xenogen IVIS® 200 Series (Caliper Life Sciences, Hopkinton, MA). Animals received an IP injection of D-Luciferin (113 mg/kg) 5 min prior to the whole-body bioluminescence imagings. Forty-eight hr after IV injection of AnnexinVivo^{TM}750, a midline incision of animals was made, and tumor tissues and organs were removed under the

Fluobeam® 800 NIR imaging system (Fluoptics, Grenoble, France). *Ex vivo* bioluminescence and fluorescence images were obtained from collected tumor tissues and organs.

S2.2. IntegriSense™750 and MMPSense™750Fast

IntegriSense™750 (MW 1,278 g/mol, PerkinElmer Inc., Boston, MA) is a targeted fluorescence imaging agent consisting of a selective non-peptide small molecule integrin $\alpha_v\beta_3$ antagonist and an NIR fluorophore (λ_{ex} = 755 nm, λ_{em} = 775 nm). IntegriSense™750 can be used to monitor tumor growth, tumor angiogenesis, and treatment efficacy. Integrin $\alpha_v\beta_3$ antagonist has been widely studied as a targeting ligand for neovasculature of tumors. IntegriSense™750 is lyophilized powder and was rehydrated with 10 mM PBS (pH 7.4) prior to IV injection. The recommended IV dose for IntegriSense™750 is 100 μL per mouse (2 nmol). *In vivo* imaging of animals at 24 hr post IV administration is recommended in general, and IntegriSense™750 clears from tissues < 5 days post IV injection. In this experiment, ES-2-luc-bearing xenograft models (7 days post IP cell inoculation) were IV injected with 100 μL of IntegriSense™750.

MMPSense™750Fast (MW 43,000 g/mol, PerkinElmer Inc., Boston, MA) is the activatable fluorescence imaging agent comprising a FAST (Fluorescence Activatable Sensor Technology) and an NIR fluorophore (λ_{ex} = 749 nm, λ_{em} = 775 nm). MMPSense™750Fast is a matrix metalloproteinase (MMP) activatable agent that is silent upon injection but produces a fluorescence signal after cleavage by MMPs (MMP 2,3,7,9,12, and 13). As MMP activation is involved in cancer progression, invasion, and metastasis, MMPSense™750Fast may be suitable to image invasive and metastatic tumor tissues. MMPSense™750Fast is lyophilized powder and was rehydrated with 10 mM PBS (pH 7.4) prior to IV injection. The recommended IV dose for

MMPSense^{TM}750Fast is 100 μL per mouse (2 nmol). *In vivo* imaging of animals at 6 hr post IV administration is recommended in general, and IntegriSense^{TM}750 clears from tissues < 4 days post IV injection. In this experiment, ES-2-luc-bearing xenograft models (7 days post IP cell inoculation) were IV injected with100 μL of MMPSense^{TM}750Fast.

Whole-body fluorescence images were obtained 0.5, 1, 2, 4, 6, 9, 12, and 24 hr post IV injections of IntegriSense^{TM}750 or MMPSense^{TM}750Fast, and whole-body bioluminescence images were obtained 0.5, 6, 12, and 24 hr post injections of those, using Xenogen IVIS® 200 Series. Animals received an IP injection of D-Luciferin (113 mg/kg) 5 min prior to the whole-body bioluminescence imagings. Twenty-four hr after IV injection of AnnexinVivo^{TM}750, a midline incision of animals was made under the Fluobeam® 800 NIR imaging system.

S3. Results and discussion

S3.1. AnnexinVivo^{TM}750

Whole-body bioluminescence of ES-2-luc tumor cells is shown along with the fluorescence image of AnnexinVivo^{TM}750 (Figure S1). The distribution of AnnexinVivo^{TM}750 in whole-body fluorescence images showed low correspondence with the peritoneal dissemination of ES-2-luc tumor cells presented in bioluminescence images. It was noted that the strongest fluorescence signal was observed in the bladders of animals. Fluorescence images of carcasses after tumor resection proved that the strongest fluorescence signals were monitored in kidneys and bladder of animals (white arrows). Collected kidneys also lit up with the strongest intensity, and the liver was also bright in *ex vivo* fluorescence images.

Under the Fluobeam® 800, NIR imaging system, the kidneys of midline-incised ES-2-luc-bearing animals were illuminated, with the strongest fluorescence intensity (FLI) at 12 and 48 hr post IV injection of AnnexinVivo™750 in Figure S2.

Relative % bioluminescence and fluorescence intensities (BLI and FLI) of collected tissues were calculated compared to those of kidneys (BLI and FLI in kidneys were 100%) (Figure S3). Kidneys showed the strongest FLI but significantly low BLI because a substantially large amount of AnnexinVivo™750 presumably passed through renal clearance. (There was no evidence of metastases in kidneys.) Bioluminescent-positive (BLU^+) tumor tissues (> 3,000% of BLI in tumors) emitted weak fluorescence with < 10% of FLI.

In comparison with NIR fluorescence images obtained by IV injected apoptosis-targeting PEG-*b*-PCL carrying DiR, shown in Figures 5.4-5.6 (chapter 5), AnnexinVivo™750 failed tumor-specific NIR imaging in the ES-2-luc-bearing xenograft model. It is assumed that apoptosis-targeting PEG-*b*-PCL carrying DiR facilitated the active tumor-targeting effect due to its nanoscopic particle size (20-100 nm) and the enhanced permeability and retention (EPR) effect, in part avoiding renal clearance and liver uptake, residing intact in blood stream, and providing higher opportunity to reach tumor tissues. Additional benefits can be expected if apoptosis-targeting PEG-*b*-PCL carrying DiR are used. For example, peptide, GFNFRLKAGAKIRFGS, targets PS in Ca^{2+}-independent manner, whereas annexin V requires substantial amounts of Ca^{2+} in order to make complete binding to PS. Apoptosis-targeting PEG-*b*-PCL carrying DiR is smaller in size and less immunogenic than AnnexinVivo™750.

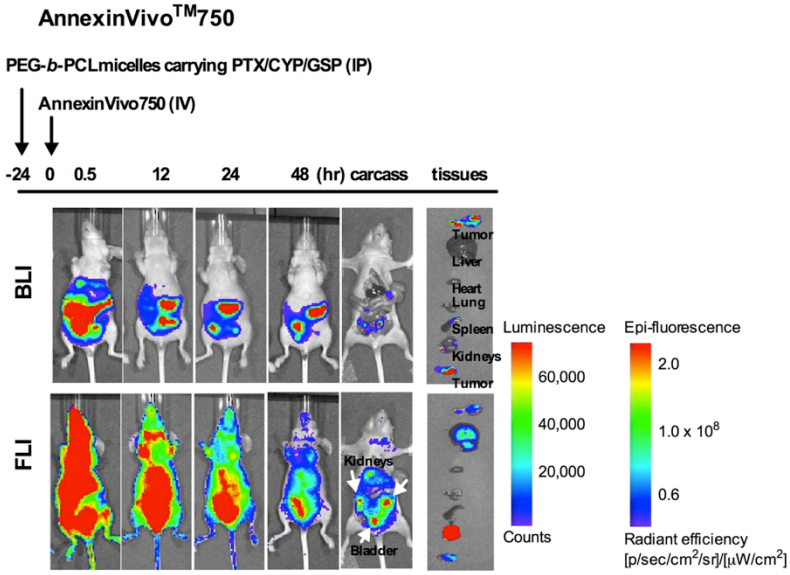

Figure S1. Assessment of apoptosis imaging *in vivo* and *ex vivo*: Whole-body and excised tissues in bioluminescence images of ES-2-luc-bearing mice and those in fluorescence images of the same animals obtained with Xenogen IVIS® 200 Series. Representative fluorescence and bioluminescence images of ES-2-luc-bearing mouse injected IP with PEG-*b*-PCL micelles carrying PTX, CYP, and GSP at 30, 30, and 30 mg/kg, followed by an IV injection of AnnexinVivo™750 at 24 hr after termination of treatments.

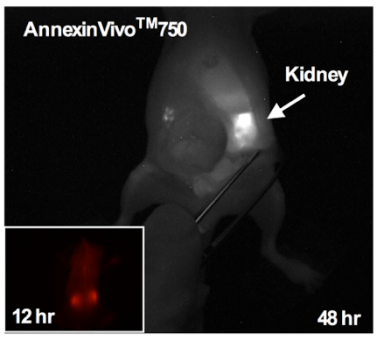

Figure S2. Fluorescence imaging of the whole-bodies of ES-2-luc-bearing mice at 12 hr post IV injection of AnnexinVivo™750 (bottom left) and fluorescence imaging of midline incised ES-2-luc-bearing mice at 48 hr post IV injection of AnnexinVivo™750 obtained with Fluobeam® 800.

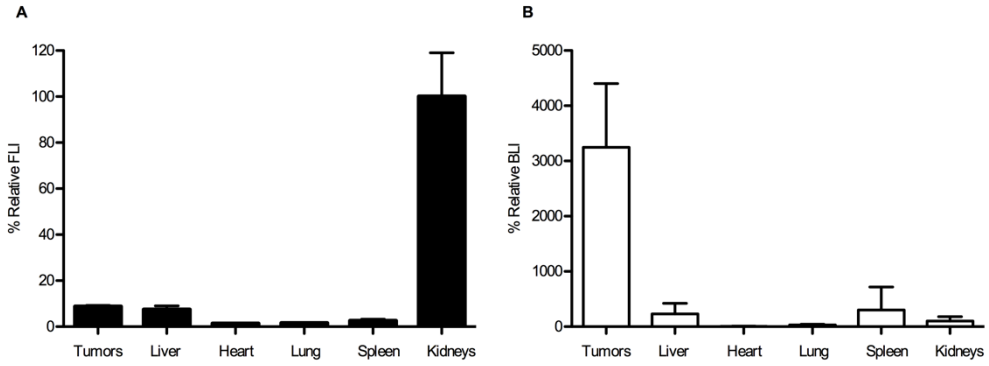

Figure S3. (A) %FLI and (B) %BLI of collected tumors and organs relative to those of kidneys at 48 hr post IV injection of AnnexinVivo^{TM}750 in ES-2-luc-bearing xenograft model.

S3.2. IntegriSense^{TM}750 and MMPSense^{TM}750Fast

Whole-body bioluminescence images of ES-2-luc tumor cells are shown along with the fluorescence images of IntegriSense^{TM}750 and MMPSense^{TM}750Fast (Figure S4). As expected, IntegriSense^{TM}750 was rapidly cleared from animals due to its small size (MW 1,278 g/mol). The distributions of IntegriSense^{TM}750 and MMPSense^{TM}750Fast in whole-body fluorescence images showed no correspondence with the peritoneal dissemination of ES-2-luc tumor cells presented in bioluminescence images, presenting the strongest signals in bladders during the entire sets of experiments.

The same distribution patterns of IntegriSense^{TM}750 and MMPSense^{TM}750Fast were observed under the Fluobeam® 800 in the midline-incised ES-2-luc-bearing xenograft model (Figure S5): intestinal organs in IntegriSense^{TM}750-received animals (left) and kidneys in MMPSense^{TM}750Fast-received animals (right) were illuminated. Notably, the fluorescence signal in IntegriSense^{TM}750-received animals was evenly distributed throughout peritoneum (grey in color) with no prominent signals. Therefore, it is because there was no specific uptake of

IntegriSense^{TM}750 at certain sites after rapid clearance of IntegriSense^{TM}750 that the entire peritoneum was equally fluorescent under the auto-settings of Fluobeam® 800.

From noninvasive bioluminescence and fluorescence imagings, quantitative BLI and FLI in the ROI (region of interest: tumor tissues in the abdomen of animals) are presented longitudinally in Figure S6. %BLI in the ROI gradually increased for both animal groups, whereas %FLI in the ROI for both rapidly decreased at 2 hr post injections, *ca*. -8% in IntegriSense^{TM}750 and -95% in MMPSense^{TM}750Fast. This implies that IP injected IntegriSense^{TM}750 and MMPSense^{TM}750Fast were not successfully delivered to metastatic IP tumor tissues, resulting in a rapid decrease of FLI at the ROI in the ES-2-luc-bearing xenograft model.

In comparison with apoptosis-targeting PEG-*b*-PCL carrying DiR, IntegriSense^{TM}750 and MMPSense^{TM}750Fast may not successfully offer tumor-targeted NIR imaging in the ES-2-luc-bearing xenograft model. Because IntegriSense^{TM}750 is relatively smaller than AnnexinVivo^{TM}750, MMPSense^{TM}750Fast and apoptosis-targeting PEG-*b*-PCL carrying DiR, earlier laparotomy and IP exploration of IntegriSense^{TM}750-received animals may be necessary to enhance tumor visualization with stronger FLI. However, early laparotomy seems not to be significantly helpful, as IntegriSense^{TM}750 still presented the strongest FLI in bladders, even at the early time point for noninvasive scanning (0.5-2 hr) as seen in Figure S4. MMPSense^{TM}750Fast also cleared from animals in rapid manner and as a consequence, the strongest FLI is observed in bladders. Although IntegriSense^{TM}750 and MMPSense^{TM}750Fast can successfully visualize primary solid tumors, given the complexity of ovarian cancer (highly invasive and metastatic tumors with large amount of ascites fluid), instability and rapid clearance

of IntegriSense^{TM}750 and MMPSense^{TM}750Fast seem to diminish their efficiencies in tumor-targeted NIR imagings.

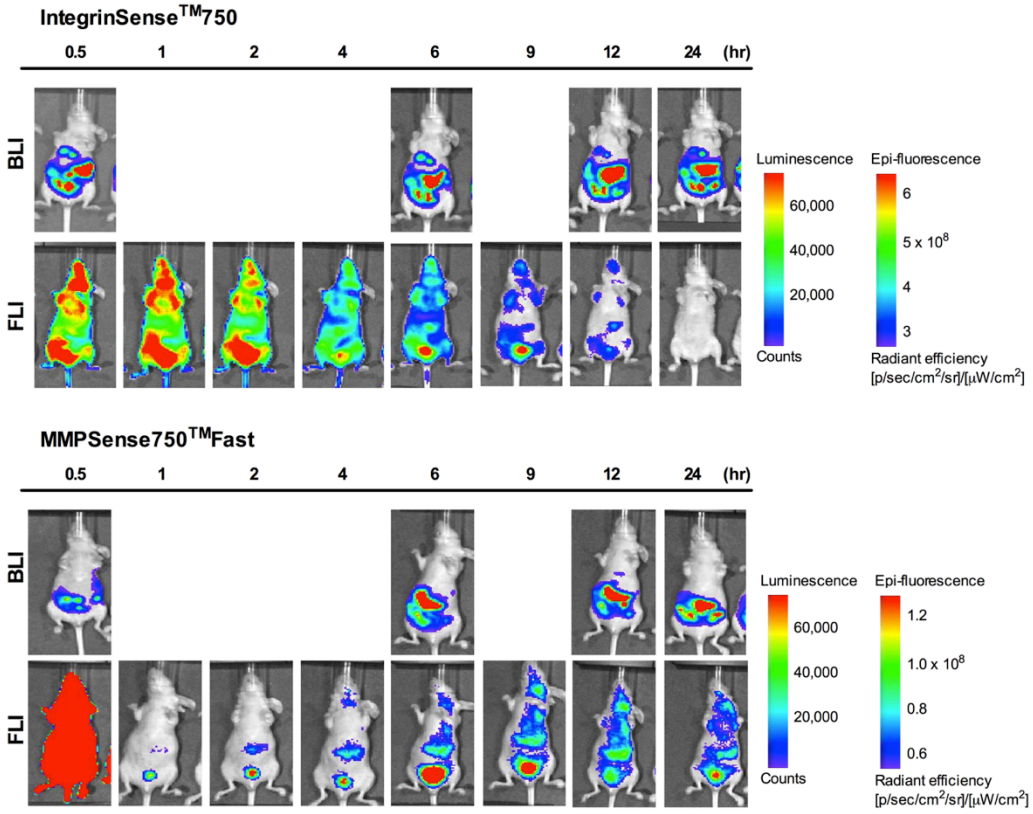

Figure S4. Assessment of metastatic tumor imaging *in vivo*: Whole-body and excised tissues in bioluminescence images of ES-2-luc-bearing mice and those in fluorescence images of same animals obtained with Xenogen IVIS® 200 Series. Representative fluorescence and bioluminescence images of ES-2-luc-bearing mouse injected IV at 0 hr with IntegriSense^{TM}750 (top) and MMPSense^{TM}750Fast (bottom).

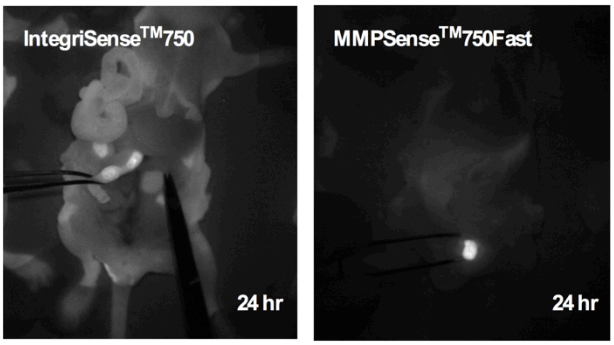

Figure S5. Fluorescence imaging of midline incised ES-2-luc-bearing mice at 24 hr post IV injection of IntegriSense^{TM}750 (left) and MMPSense^{TM}750Fast (right) obtained with Fluobeam$^{®}$ 800.

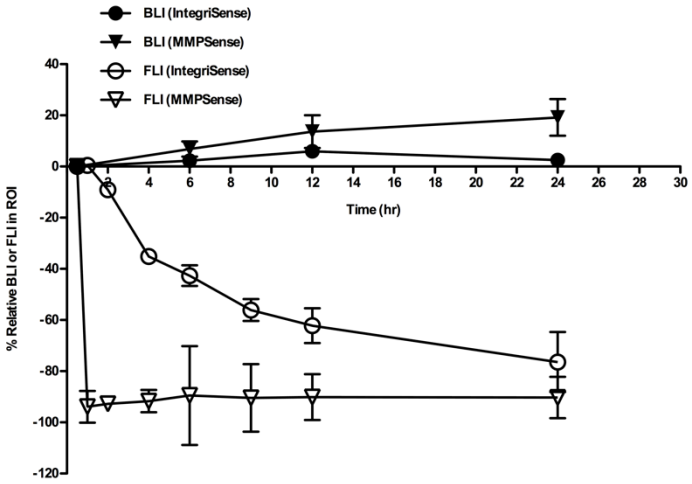

Figure S6. Relative %BLI and %FLI of ROIs in noninvasive whole-body images of ES-2-luc-bearing mouse in a time-dependent manner.

S4. Conclusion

Although it has been reported that commercially available NIR imaging agents successfully provided tumor-targeted NIR fluorescence images in primary solid tumor tissues, they failed to show superior efficiency in tumor-targeted NIR fluorescence imaging of highly invasive and metastatic ovarian tumor tissues in this investigation.

Bibliography

1. Kwon, G. S.; Okano, T., Polymeric micelles as new drug carriers. *Adv. Drug Deliver Rev.* **1996,** *21* (2), 107-116.

2. Miyata, K.; Christie, R. J.; Kataoka, K., Polymeric micelles for nano-scale drug delivery. *React. Funct. Polym.* **2011,** *71* (3), 227-234.

3. Rapoport, N., Physical stimuli-responsive polymeric micelles for anti-cancer drug delivery. *Prog. Polym. Sci.* **2007,** *32* (8-9), 962-990.

4. Jones, M. C.; Leroux, J. C., Polymeric micelles - a new generation of colloidal drug carriers. *Eur. J. Pharm. Biopharm.* **1999,** *48* (2), 101-111.

5. Sutton, D.; Wang, S. H.; Nasongkla, N.; Gao, J. M.; Dormidontova, E. E., Doxorubicin and beta-lapachone release and interaction with micellar core materials: Experiment and modeling. *Exp. Biol. Med.* **2007,** *232* (8), 1090-1099.

6. Lipinski, C. A., Drug-like properties and the causes of poor solubility and poor permeability. *J. Pharmacol. Toxicol. Methods* **2000,** *44* (1), 235-249.

7. Kim, S.; Shi, Y. Z.; Kim, J. Y.; Park, K.; Cheng, J. X., Overcoming the barriers in micellar drug delivery: loading efficiency, *in vivo* stability, and micelle-cell interaction. *Expert Opin. Drug Del.* **2010,** *7* (1), 49-62.

8. Owens, D. E.; Peppas, N. A., Opsonization, biodistribution, and pharmacokinetics of polymeric nanoparticles. *Int. J. Pharm.* **2006,** *307* (1), 93-102.

9. Matsumura, Y.; Kataoka, K., Preclinical and clinical studies of anticancer agent-incorporating polymer micelles. *Cancer. Sci.* **2009,** *100* (4), 572-579.

10. Alexis, F.; Pridgen, E.; Molnar, L. K.; Farokhzad, O. C., Factors affecting the clearance and biodistribution of polymeric nanoparticles. *Mol. Pharm.* **2008,** *5* (4), 505-515.

11. Hashizume, H.; Baluk, P.; Morikawa, S.; McLean, J. W.; Thurston, G.; Roberge, S.; Jain, R. K.; McDonald, D. M., Openings between defective endothelial cells explain tumor vessel leakiness. *Am. J. Pathol.* **2000,** *156* (4), 1363-1380.

12. Maeda, H., The enhanced permeability and retention (EPR) effect in tumor vasculature: The key role of tumor-selective macromolecular drug targeting. *Adv. Enzyme Regul.* **2001,** *41*, 189-207.

13. Lee, K. S.; Chung, H. C.; Im, S. A.; Park, Y. H.; Kim, C. S.; Kim, S. B.; Rha, S. Y.; Lee, M. Y.; Ro, J., Multicenter phase II trial of Genexol-PM, a Cremophor-free, polymeric

micelle formulation of paclitaxel, in patients with metastatic breast cancer. *Breast Cancer Res. Treat.* **2008,** *108* (2), 241-250.

14. Heppner, G. H., Tumor Heterogeneity. *Cancer Res.* **1984,** *44* (6), 2259-2265.

15. Prabhakar, U.; Maeda, H.; Jain, R. K.; Sevick-Muraca, E. M.; Zamboni, W.; Farokhzad, O. C.; Barry, S. T.; Gabizon, A.; Grodzinski, P.; Blakey, D. C., Challenges and key considerations of the enhanced permeability and retention effect for nanomedicine drug delivery in oncology. *Cancer Res.* **2013,** *73* (8), 2412-2417.

16. Jain, R. K.; Stylianopoulos, T., Delivering nanomedicine to solid tumors. *Nat. Rev. Clin. Oncol.* **2010,** *7* (11), 653-664.

17. Jang, S. H.; Wientjes, M. G.; Lu, D.; Au, J. L. S., Drug delivery and transport to solid tumors. *Pharm. Res.* **2003,** *20* (9), 1337-1350.

18. Lu, D.; Wientjes, M. G.; Lu, Z.; Au, J. L. S., Tumor priming enhances delivery and efficacy of nanomedicines. *J. Pharmacol. Exp. Ther.* **2007,** *322* (1), 80-88.

19. Byrne, J. D.; Betancourt, T.; Brannon-Peppas, L., Active targeting schemes for nanoparticle systems in cancer therapeutics. *Adv. Drug Delivery Rev.* **2008,** *60* (15), 1615-1626.

20. Hanahan, D.; Weinberg, R. A., The hallmarks of cancer. *Cell* **2000,** *100* (1), 57-70.

21. Schellenberger, E. A.; Bogdanov, A.; Petrovsky, A.; Ntziachristos, V.; Weissleder, R.; Josephson, L., Optical imaging of apoptosis as a biomarker of tumor response to chemotherapy. *Neoplasia* **2003,** *5* (3), 187-192.

22. Fadeel, B.; Xue, D., The ins and outs of phospholipid asymmetry in the plasma membrane: roles in health and disease. *Crit. Rev. Biochem. Mol. Biol.* **2009,** *44* (5), 264-277.

23. Schlegel, R. A.; Williamson, P., Phosphatidylserine, a death knell. *Cell Death Differ.* **2001,** *8* (6), 551-563.

24. Song, S. L.; Xiong, C. Y.; Lu, W.; Ku, G.; Huang, G.; Li, C., Apoptosis imaging probe predicts early chemotherapy response in preclinical models: a comparative study with F-18-FDG PET. *J. Nucl. Med.* **2013,** *54* (1), 104-110.

25. Xiong, C. Y.; Brewer, K.; Song, S. L.; Zhang, R.; Lu, W.; Wen, X. X.; Li, C., Peptide-Based Imaging Agents Targeting Phosphatidylserine for the Detection of Apoptosis. *J. Med. Chem.* **2011,** *54* (6), 1825-1835.

26. Fodale, V.; Pierobon, M.; Liotta, L.; Petricoin, E., Mechanism of cell adaptation: when and how do cancer cells develop chemoresistance? *Cancer J.* **2011,** *17* (2), 89-95.

27. Frei, E., 3rd; Karon, M.; Levin, R. H.; Freireich, E. J.; Taylor, R. J.; Hananian, J.; Selawry, O.; Holland, J. F.; Hoogstraten, B.; Wolman, I. J.; Abir, E.; Sawitsky, A.; Lee, S.; Mills, S. D.; Burgert, E. O., Jr.; Spurr, C. L.; Patterson, R. B.; Ebaugh, F. G.; James, G. W., 3rd; Moon, J. H., The effectiveness of combinations of antileukemic agents in inducing and maintaining remission in children with acute leukemia. *Blood* **1965,** *26* (5), 642-656.

28. Decker, S.; Sausville, E. A., Preclinical modeling of combination treatments: fantasy or requirement? *Annals of the New York Academy of Sciences* **2005,** *1059*, 61-69.

29. Hu, C. M.; Aryal, S.; Zhang, L., Nanoparticle-assisted combination therapies for effective cancer treatment. *Ther. Delivery* **2010,** *1* (2), 323-334.

30. Shin, H. C.; Alani, A. W.; Cho, H.; Bae, Y.; Kolesar, J. M.; Kwon, G. S., A 3-in-1 polymeric micelle nanocontainer for poorly water-soluble drugs. *Mol. Pharm.* **2011,** *8* (4), 1257-1265.

31. Hasenstein, J. R.; Shin, H. C.; Kasmerchak, K.; Buehler, D.; Kwon, G. S.; Kozak, K. R., Antitumor activity of Triolimus: a novel multidrug-loaded micelle containing Paclitaxel, Rapamycin, and 17-AAG. *Mol. Cancer Ther.* **2012,** *11* (10), 2233-2242.

32. Shin, H. C.; Cho, H.; Lai, T. C.; Kozak, K. R.; Kolesar, J. M.; Kwon, G. S., Pharmacokinetic study of 3-in-1 poly(ethylene glycol)-*block*-poly(D, L-lactic acid) micelles carrying paclitaxel, 17-allylamino-17-demethoxygeldanamycin, and rapamycin. *J. Control Release* **2012,** *163* (1), 93-99.

33. Frangioni, J. V., New technologies for human cancer imaging. *J. Clin. Oncol.* **2008,** *26* (24), 4012-4021.

34. Weissleder, R.; Pittet, M. J., Imaging in the era of molecular oncology. *Nature* **2008,** *452* (7187), 580-589.

35. Koo, O. M.; Rubinstein, I.; Onyuksel, H., Role of nanotechnology in targeted drug delivery and imaging: a concise review. *Nanomedicine* **2005,** *1* (3), 193-212.

36. Gunasekera, U. A.; Pankhurst, Q. A.; Douek, M., Imaging applications of nanotechnology in cancer. *Target Oncol.* **2009,** *4* (3), 169-181.

37. Keereweer, S.; Van Driel, P. B. A. A.; Snoeks, T. J. A.; Kerrebijn, J. D. F.; de Jong, R. J. B.; Vahrmeijer, A. L.; Sterenborg, H. J. C. M.; Lowik, C. W. G. M., Optical Image-

Guided Cancer Surgery: Challenges and Limitations. *Clin. Cancer Res.* **2013,** *19* (14), 3745-3754.

38. Vahrmeijer, A. L.; Hutteman, M.; van der Vorst, J. R.; van de Velde, C. J.; Frangioni, J. V., Image-guided cancer surgery using near-infrared fluorescence. *Nat. Rev. Cli.n Oncol.* **2013,** *10* (9), 507-518.

39. Keereweer, S.; Kerrebijn, J. D. F.; van Driel, P. B. A. A.; Xie, B. W.; Kaijzel, E. L.; Snoeks, T. J. A.; Que, I.; Hutteman, M.; van der Vorst, J. R.; Mieog, J. S. D.; Vahrmeijer, A. L.; van de Velde, C. J. H.; de Jong, R. J. B.; Lowik, C. W. G. M., Optical Image-guided Surgery-Where Do We Stand? *Mol. Imaging Biol.* **2011,** *13* (2), 199-207.

40. Zhang, H.; Uselman, R. R.; Yee, D., Exogenous near-infrared fluorophores and their applications in cancer diagnosis: biological and clinical perspectives. *Expert Opin. Med Diagn.* **2011,** *5* (3), 241-251.

41. Bremer, C.; Bredow, S.; Mahmood, U.; Weissleder, R.; Tung, C. H., Optical imaging of matrix metalloproteinase-2 activity in tumors: feasibility study in a mouse model. *Radiology* **2001,** *221* (2), 523-529.

42. Jiang, S.; Gnanasammandhan, M. K.; Zhang, Y., Optical imaging-guided cancer therapy with fluorescent nanoparticles. *J. R. Soc. Interface* **2010,** *7* (42), 3-18.

43. Kumar, R.; Kulkarni, A.; Nagesha, D. K.; Sridhar, S., *In vitro* evaluation of theranostic polymeric micelles for imaging and drug delivery in cancer. *Theranostics* **2012,** *2* (7), 714-722.

44. Kim, K.; Lee, M.; Park, H.; Kim, J. H.; Kim, S.; Chung, H.; Choi, K.; Kim, I. S.; Seong, B. L.; Kwon, I. C., Cell-permeable and biocompatible polymeric nanoparticles for apoptosis imaging. *J. Am. Chem. Soc.* **2006,** *128* (11), 3490-3491.

45. Tanaka, E.; Choi, H. S.; Fujii, H.; Bawendi, M. G.; Frangioni, J. V., Image-guided oncologic surgery using invisible light: completed pre-clinical development for sentinel lymph node mapping. *Ann. Surg. Oncol.* **2006,** *13* (12), 1671-1681.

46. Troyan, S. L.; Kianzad, V.; Gibbs-Strauss, S. L.; Gioux, S.; Matsui, A.; Oketokoun, R.; Ngo, L.; Khamene, A.; Azar, F.; Frangioni, J. V., The FLARE intraoperative near-infrared fluorescence imaging system: a first-in-human clinical trial in breast cancer sentinel lymph node mapping. *Ann. Surg. Oncol.* **2009,** *16* (10), 2943-2952.

47. Ntziachristos, V.; Yoo, J. S.; van Dam, G. M., Current concepts and future perspectives on surgical optical imaging in cancer. *J. Biomed. Opt.* **2010,** *15* (6), 066024.

48. van Dam, G. M.; Themelis, G.; Crane, L. M.; Harlaar, N. J.; Pleijhuis, R. G.; Kelder, W.; Sarantopoulos, A.; de Jong, J. S.; Arts, H. J.; van der Zee, A. G.; Bart, J.; Low, P. S.; Ntziachristos, V., Intraoperative tumor-specific fluorescence imaging in ovarian cancer by folate receptor-alpha targeting: first in-human results. *Nat. Med.* **2011,** *17* (10), 1315-1319.

49. Thurber, G. M.; Figueiredo, J. L.; Weissleder, R., Detection limits of intraoperative near infrared imaging for tumor resection. *J. Surg. Oncol.* **2010,** *102* (7), 758-764.

50. Mery, E.; Jouve, E.; Guillermet, S.; Bourgognon, M.; Castells, M.; Golzio, M.; Rizo, P.; Delord, J. P.; Querleu, D.; Couderc, B., Intraoperative fluorescence imaging of peritoneal dissemination of ovarian carcinomas. A preclinical study. *Gynecol. Oncol.* **2011,** *122* (1), 155-162.

51. Altinoglu, E. I.; Russin, T. J.; Kaiser, J. M.; Barth, B. M.; Eklund, P. C.; Kester, M.; Adair, J. H., Near-infrared emitting fluorophore-doped calcium phosphate nanoparticles for *in vivo* imaging of human breast cancer. *Acs Nano* **2008,** *2* (10), 2075-2084.

52. Frangioni, J. V., *In vivo* near-infrared fluorescence imaging. *Curr. Opin. Chem. Biol.* **2003,** *7* (5), 626-634.

53. Keramidas, M.; Josserand, V.; Righini, C. A.; Wenk, C.; Faure, C.; Coll, J. L., Intraoperative near-infrared image-guided surgery for peritoneal carcinomatosis in a preclinical experimental model. *Brit. J. Surg.* **2010,** *97* (5), 737-743.

54. Kumar, R.; Ohulchanskyy, T. Y.; Roy, I.; Gupta, S. K.; Borek, C.; Thompson, M. E.; Prasad, P. N., Near-infrared phosphorescent polymeric nanomicelles: efficient optical probes for tumor imaging and detection. *Acs Appl. Mater. Inter.* **2009,** *1* (7), 1474-1481.

55. Kwon, G.; Suwa, S.; Yokoyama, M.; Okano, T.; Sakurai, Y.; Kataoka, K., Enhanced tumor accumulation and prolonged circulation times of micelle-forming poly(ethylene oxide-aspartate) block copolymer-adriamycin conjugates. *J. Control Release* **1994,** *29* (1-2), 17-23.

56. Leblond, F.; Davis, S. C.; Valdes, P. A.; Pogue, B. W., Pre-clinical whole-body fluorescence imaging: Review of instruments, methods and applications. *J. Photoch. Photobio. B* **2010,** *98* (1), 77-94.

57. Luo, L. B.; Tam, J.; Maysinger, D.; Eisenberg, A., Cellular internalization of poly(ethylene oxide)-*b*-poly(epsilon-caprolactone) diblock copolymer micelles. *Bioconjugate Chem.* **2002,** *13* (6), 1259-1265.

58. Maeda, H., Tumor-selective delivery of macromolecular drugs *via* the EPR effect: background and future prospects. *Bioconjugate Chem.* **2010,** *21* (5), 797-802.

59. Park, K.; Lee, S.; Kang, E.; Kim, K.; Choi, K.; Kwon, I. C., New generation of multifunctional nanoparticles for cancer imaging and therapy. *Adv. Funct. Mater.* **2009,** *19* (10), 1553-1566.

60. Soltesz, E. G.; Kim, S.; Laurence, R. G.; DeGrand, A. M.; Parungo, C. P.; Dor, D. M.; Cohn, L. H.; Bawendi, M. G.; Frangioni, J. V.; Mihaljevic, T., Intraoperative sentinel lymph node mapping of the lung using near-infrared fluorescent quantum dots. *Ann. Thorac. Surg.* **2005,** *79* (1), 269-277.

61. Yang, Z.; Zheng, S. Y.; Harrison, W. J.; Harder, J.; Wen, X. X.; Gelovani, J. G.; Qiao, A.; Li, C., Long-circulating near-infrared fluorescence core-cross-linked polymeric micelles: synthesis, characterization, and dual nuclear/optical imaging. *Biomacromolecules* **2007,** *8* (11), 3422-3428.

62. Nguyen, Q. T.; Olson, E. S.; Aguilera, T. A.; Jiang, T.; Scadeng, M.; Ellies, L. G.; Tsien, R. Y., Surgery with molecular fluorescence imaging using activatable cell-penetrating peptides decreases residual cancer and improves survival. *P. Natl. Acad. Sci. USA* **2010,** *107* (9), 4317-4322.

63. Trotter, M. J.; Chaplin, D. J.; Olive, P. L., Use of a carbocyanine dye as a marker of functional vasculature in murine tumors. *Brit. J. Cancer* **1989,** *59* (5), 706-709.

64. Texier, I.; Goutayer, M.; Da Silva, A.; Guyon, L.; Djaker, N.; Josserand, V.; Neumann, E.; Bibette, J.; Vinet, F., Cyanine-loaded lipid nanoparticles for improved *in vivo* fluorescence imaging. *J. Biomed Opt.* **2009,** *14* (5).

65. Forrest, M. L.; Won, C. Y.; Malick, A. W.; Kwon, G. S., *In vitro* release of the mTOR inhibitor rapamycin from poly(ethylene glycol)-*b*-poly(epsilon-caprolactone) micelles. *J. Control Release* **2006,** *110* (2), 370-377.

66. Forrest, M. L.; Yanez, J. A.; Remsberg, C. M.; Ohgami, Y.; Kwon, G. S.; Davies, N. M., Paclitaxel prodrugs with sustained release and high solubility in poly(ethylene glycol)-*b*-poly(epsilon-caprolactone) micelle nanocarriers: pharmacokinetic disposition, tolerability, and cytotoxicity. *Pharm. Res.* **2008,** *25* (1), 194-206.

67. Forrest, M. L.; Zhao, A.; Won, C. Y.; Malick, A. W.; Kwon, G. S., Lipophilic prodrugs of Hsp90 inhibitor geldanamycin for nanoencapsulation in poly(ethylene glycol)-*b*-poly(epsilon-caprolactone) micelles. *J. Control Release* **2006,** *116* (2), 139-149.

68. Kumar, V.; Prud'Homme, R. K., Thermodynamic limits on drug loading in nanoparticle cores. *J. Pharm. Sci.* **2008,** *97* (11), 4904-4914.

69. Liu, J. B.; Zeng, F. Q.; Allen, C., In vivo fate of unimers and micelles of a poly(ethylene glycol)-*block*-poly(caprolactone) copolymer in mice following intravenous administration. *Eur. J. Pharm. Biopharm.* **2007,** *65* (3), 309-319.

70. Tian, Y. Q.; Wu, W. C.; Chen, C. Y.; Jang, S. H.; Zhang, M.; Strovas, T.; Anderson, J.; Cookson, B.; Li, Y. Z.; Meldrum, D.; Chen, W. C.; Jeni, A. K. Y., Utilization of micelles formed from poly(ethylene glycol)-*block*-poly(epsilon-caprolactone) block copolymers as nanocarriers to enable hydrophobic red two-photon absorbing emitters for cells imaging. *J. Biomed. Mater. Res. A* **2010,** *93A* (3), 1068-1079.

71. Mikhail, A. S.; Allen, C., Block copolymer micelles for delivery of cancer therapy: transport at the whole body, tissue and cellular levels. *J Control Release* **2009,** *138* (3), 214-223.

72. Khairutdinov, R. F.; Serpone, N., Photophysics of cyanine dyes: subnanosecond relaxation dynamics in monomers, dimers, and H- and J-aggregates in solution. *J. Phys. Chem. B* **1997,** *101* (14), 2602-2610.

73. Lee, S.; Ryu, J. H.; Park, K.; Lee, A.; Lee, S. Y.; Youn, I. C.; Ahn, C. H.; Yoon, S. M.; Myung, S. J.; Moon, D. H.; Chen, X.; Choi, K.; Kwon, I. C.; Kim, K., Polymeric nanoparticle-based activatable near-infrared nanosensor for protease determination *in vivo*. *Nano Lett* **2009,** *9* (12), 4412-4416.

74. Maiti, N. C.; Mazumdar, S.; Periasamy, N., J- and H-aggregates of porphyrin-surfactant complexes: Time-resolved fluorescence and other spectroscopic studies. *J. Phys. Chem. B* **1998,** *102* (9), 1528-1538.

75. Tummino, P. J.; Gafni, A., Determination of the aggregation number of detergent micelles using steady-state fluorescence quenching. *Biophys. J.* **1993,** *64* (5), 1580-1587.

76. Zeisser-Labouebe, M.; Mattiuzzo, M.; Lange, N.; Gurny, R.; Delie, F., Quenching-induced deactivation of photosensitizer by nano encapsulation to improve phototherapy of cancer. *J. Drug Target* **2009,** *17* (8), 619-626.

77. Peng, X. X.; Chen, H. X.; Draney, D. R.; Volcheck, W.; Schutz-Geschwender, A.; Olive, D. M., A nonfluorescent, broad-range quencher dye for Forster resonance energy transfer assays. *Anal. Biochem.* **2009,** *388* (2), 220-228.

78. Miao, Z.; Ren, G.; Liu, H. G.; Jiang, L.; Cheng, Z., Cy5.5-labeled Affibody molecule for near-infrared fluorescent optical imaging of epidermal growth factor receptor positive tumors. *J. Biomed Opt.* **2010,** *15* (3).

79. Olson, E. S.; Jiang, T.; Aguilera, T. A.; Nguyen, Q. T.; Ellies, L. G.; Scadeng, M.; Tsien, R. Y., Activatable cell penetrating peptides linked to nanoparticles as dual probes for *in*

vivo fluorescence and MR imaging of proteases. *P. Natl. Acad. Sci. USA* **2010,** *107* (9), 4311-4316.

80. Farokhzad, O. C.; Langer, R., Impact of Nanotechnology on Drug Delivery. *Acs Nano* **2009,** *3* (1), 16-20.

81. Hammond, P. T., Virtual Issue on Nanomaterials for Drug Delivery. *Acs Nano* **2011,** *5* (2), 681-684.

82. Hori, K.; Nishihara, M.; Yokoyama, M., Vital mcroscopic analysis of polymeric micelle extravasation from tumor vessels: macromolecular delivery according to tumor vascular growth stage. *J. Pharm. Sci.* **2010,** *99* (1), 549-562.

83. Rao, J. H., Shedding light on tumors using nanoparticles. *Acs Nano* **2008,** *2* (10), 1984-1986.

84. He, X. X.; Wang, K. M.; Cheng, Z., *In vivo* near-infrared fluorescence imaging of cancer with nanoparticle-based probes. *Wires. Nanomed. Nanobi.* **2010,** *2* (4), 349-366.

85. Kim, T. H.; Chen, Y. P.; Mount, C. W.; Gombotz, W. R.; Li, X. D.; Pun, S. H., Evaluation of temperature-sensitive, indocyanine green-encapsulating micelles for noninvasive near-infrared tumor imaging. *Pharm. Res.* **2010,** *27* (9), 1900-1913.

86. Singhal, S.; Nie, S. M.; Wang, M. D., Nanotechnology applications in surgical oncology. *Annu. Rev. Med.* **2010,** *61*, 359-373.

87. Mieog, J. S. D.; Hutteman, M.; van der Vorst, J. R.; Kuppen, P. J. K.; Que, I.; Dijkstra, J.; Kaijzel, E. L.; Prins, F.; Lowik, C. W. G. M.; Smit, V. T. H. B. M.; van de Velde, C. J. H.; Vahrmeijer, A. L., Image-guided tumor resection using real-time near-infrared fluorescence in a syngeneic rat model of primary breast cancer. *Breast Cancer Res. Treat.* **2011,** *128* (3), 679-689.

88. Lee, H.; Fonge, H.; Hoang, B.; Reilly, R. M.; Allen, C., The effects of particle size and molecular targeting on the intratumoral and subcellular distribution of polymeric nanoparticles. *Mol. Pharm.* **2010,** *7* (4), 1195-1208.

89. Lee, H.; Hoang, B.; Fonge, H.; Reilly, R. M.; Allen, C., *In vivo* distribution of polymeric nanoparticles at the whole-body, tumor, and cellular levels. *Pharm. Res.* **2010,** *27* (11), 2343-2355.

90. Kalchenko, V.; Shivtiel, S.; Malina, V.; Lapid, K.; Haramati, S.; Lapidot, T.; Brill, A.; Harmelin, A., Use of lipophilic near-infrared dye in whole-body optical imaging of hematopoietic cell homing. *J. Biomed. Opt.* **2006,** *11* (5).

91. Au, J. L. S.; Jang, S. H.; Zheng, J.; Chen, C. T.; Song, S.; Hu, L.; Wientjes, M. G., Determinants of drug delivery and transport to solid tumors. *J. Control Release* **2001,** *74* (1-3), 31-46.

92. Stohrer, M.; Boucher, Y.; Stangassinger, M.; Jain, R. K., Oncotic pressure in solid tumors is elevated. *Cancer Res.* **2000,** *60* (15), 4251-4255.

93. Tredan, O.; Galmarini, C. M.; Patel, K.; Tannock, I. F., Drug resistance and the solid tumor microenvironment. *J. Natl. Cancer I.* **2007,** *99* (19), 1441-1454.

94. Matsumura, Y., Polymeric micellar delivery systems in oncology. *Jpn. J. Clin. Oncol.* **2008,** *38* (12), 793-802.

95. Shin, H. C.; Alani, A. W. G.; Rao, D. A.; Rockich, N. C.; Kwon, G. S., Multi-drug loaded polymeric micelles for simultaneous delivery of poorly soluble anticancer drugs. *J. Control Release* **2009,** *140* (3), 294-300.

96. Kim, D. W.; Kim, S. Y.; Kim, H. K.; Kim, S. W.; Shin, S. W.; Kim, J. S.; Park, K.; Lee, M. Y.; Heo, D. S., Multicenter phase II trial of Genexol-PM, a novel Cremophor-free, polymeric micelle formulation of paclitaxel, with cisplatin in patients with advanced non-small-cell lung cancer. *Annal.s of Oncology* **2007,** *18* (12), 2009-2014.

97. Kim, S. C.; Kim, D. W.; Shim, Y. H.; Bang, J. S.; Oh, H. S.; Kim, S. W.; Seo, M. H., In vivo evaluation of polymeric micellar paclitaxel formulation: toxicity and efficacy. *J. Control Release* **2001,** *72* (1-3), 191-202.

98. Hoang, B.; Lee, H.; Reilly, R. M.; Allen, C., Noninvasive Monitoring of the Fate of In-111-labeled block copolymer micelles by high resolution and high sensitivity microSPECT/CT imaging. *Mol Pharm.* **2009,** *6* (2), 581-592.

99. Cho, H.; Indig, G. L.; Weichert, J.; Shin, H. C.; Kwon, G. S., *In vivo* cancer imaging by poly(ethylene glycol)-*b*-poly(epsilon-caprolactone) micelles containing a near-infrared probe. *Nanomedicine* **2012,** *8* (2), 228-236.

100. Siegel, R.; Ward, E.; Brawley, O.; Jemal, A., Cancer statistics, 2011: the impact of eliminating socioeconomic and racial disparities on premature cancer deaths. *CA: Cancer J. Clin.* **2011,** *61* (4), 212-236.

101. Harries, M.; Gore, M., Part II: chemotherapy for epithelial ovarian cancer-treatment of recurrent disease. *Lancet. Oncol.* **2002,** *3* (9), 537-545.

102. Ray, A.; Meng, E.; Reed, E.; Shevde, L. A.; Rocconi, R. P., Hedgehog signaling pathway regulates the growth of ovarian cancer spheroid forming cells. *Int. J. Oncol.* **2011,** *39* (4), 797-804.

103. Steg, A. D.; Katre, A. A.; Bevis, K. S.; Ziebarth, A.; Dobbin, Z. C.; Shah, M. M.; Alvarez, R. D.; Landen, C. N., Smoothened antagonists reverse taxane resistance in ovarian cancer. *Mol Cancer Ther.* **2012,** *11* (7), 1587-1597.

104. Wang, J.; Zhou, J. Y.; Zhang, L.; Wu, G. S., Involvement of MKP-1 and Bcl-2 in acquired cisplatin resistance in ovarian cancer cells. *Cell Cycle* **2009,** *8* (19), 3191-3198.

105. Bajaj, G.; Yeo, Y., Drug delivery systems for intraperitoneal therapy. *Pharm. Res.* **2010,** *27* (5), 735-738.

106. Barbolina, M. V.; Moss, N. M.; Westfall, S. D.; Liu, Y.; Burkhalter, R. J.; Marga, F.; Forgacs, G.; Hudson, L. G.; Stack, M. S., Microenvironmental regulation of ovarian cancer metastasis. *Cancer Treat. Res.* **2009,** *149*, 319-334.

107. De Souza, R.; Zahedi, P.; Badame, R. M.; Allen, C.; Piquette-Miller, M., Chemotherapy dosing schedule influences drug resistance development in ovarian cancer. *Mol. Cancer Ther.* **2011,** *10* (7), 1289-1299.

108. Lu, Z.; Wang, J.; Wientjes, M. G.; Au, J. L., Intraperitoneal therapy for peritoneal cancer. *Future Oncol.* **2010,** *6* (10), 1625-1641.

109. Chen, J. K.; Taipale, J.; Cooper, M. K.; Beachy, P. A., Inhibition of Hedgehog signaling by direct binding of cyclopamine to Smoothened. *Genes Dev.* **2002,** *16* (21), 2743-2748.

110. Huang, Y. W.; Wang, L. S.; Chang, H. L.; Ye, W.; Dowd, M. K.; Wan, P. J.; Lin, Y. C., Molecular mechanisms of (-)-gossypol-induced apoptosis in human prostate cancer cells. *Anticancer Res.* **2006,** *26* (3A), 1925-1933.

111. Jia, L.; Coward, L. C.; Kerstner-Wood, C. D.; Cork, R. L.; Gorman, G. S.; Noker, P. E.; Kitada, S.; Pellecchia, M.; Reed, J. C., Comparison of pharmacokinetic and metabolic profiling among gossypol, apogossypol and apogossypol hexaacetate. *Cancer Chemoth. Pharm.* **2008,** *61* (1), 63-73.

112. Cho, H.; Kwon, G. S., Polymeric micelles for neoadjuvant cancer therapy and tumor-primed optical imaging. *ACS nano* **2011,** *5* (11), 8721-8729.

113. Friedrich, J.; Seidel, C.; Ebner, R.; Kunz-Schughart, L. A., Spheroid-based drug screen: considerations and practical approach. *Nat. Protoc.* **2009,** *4* (3), 309-324.

114. Zinn, K. R.; Chaudhuri, T. R.; Szafran, A. A.; O'Quinn, D.; Weaver, C.; Dugger, K.; Lamar, D.; Kesterson, R. A.; Wang, X.; Frank, S. J., Noninvasive bioluminescence imaging in small animals. *ILAR J.* **2008,** *49* (1), 103-115.

115. Dufort, S.; Sancey, L.; Wenk, C.; Josserand, V.; Coll, J. L., Optical small animal imaging in the drug discovery process. *Biochim. biophys. Acta* **2010,** *1798* (12), 2266-2273.

116. Lee, H. J.; Tantawy, M. N.; Nam, K. T.; Choi, I.; Peterson, T. E.; Price, R. R., Evaluation of an intraperitoneal ovarian cancer syngeneic mouse model using 18F-FDG MicroPET imaging. *Int. J. Gynecol. Cancer* **2011,** *21* (1), 22-27.

117. Jensen, M. M.; Erichsen, K. D.; Bjorkling, F.; Madsen, J.; Jensen, P. B.; Hojgaard, L.; Sehested, M.; Kjaer, A., Early detection of response to experimental chemotherapeutic Top216 with [18F]FLT and [18F]FDG PET in human ovary cancer xenografts in mice. *PLoS One* **2010,** *5* (9), e12965.

118. Aide, N.; Kinross, K.; Cullinane, C.; Roselt, P.; Waldeck, K.; Neels, O.; Dorow, D.; McArthur, G.; Hicks, R. J., 18F-FLT PET as a surrogate marker of drug efficacy during mTOR inhibition by everolimus in a preclinical cisplatin-resistant ovarian tumor model. *J. Nucl. Med.* **2010,** *51* (10), 1559-1564.

119. Zavaleta, C. L.; Phillips, W. T.; Bradley, Y. C.; McManus, L. M.; Jerabek, P. A.; Goins, B. A., Characterization of an intraperitoneal ovarian cancer xenograft model in nude rats using noninvasive microPET imaging. *Int. J. Gynecol. Cancer* **2007,** *17* (2), 407-417.

120. Vassileva, V.; Moriyama, E. H.; De Souza, R.; Grant, J.; Allen, C. J.; Wilson, B. C.; Piquette-Miller, M., Efficacy assessment of sustained intraperitoneal paclitaxel therapy in a murine model of ovarian cancer using bioluminescent imaging. *Br. J. Cancer* **2008,** *99* (12), 2037-2043.

121. Devalapally, H.; Duan, Z.; Seiden, M. V.; Amiji, M. M., Modulation of drug resistance in ovarian adenocarcinoma by enhancing intracellular ceramide using tamoxifen-loaded biodegradable polymeric nanoparticles. *Clin. Cancer Res.* **2008,** *14* (10), 3193-3203.

122. Devalapally, H.; Duan, Z.; Seiden, M. V.; Amiji, M. M., Paclitaxel and ceramide co-administration in biodegradable polymeric nanoparticulate delivery system to overcome drug resistance in ovarian cancer. *Int. J. Cancer* **2007,** *121* (8), 1830-1838.

123. Vassileva, V.; Grant, J.; De Souza, R.; Allen, C.; Piquette-Miller, M., Novel biocompatible intraperitoneal drug delivery system increases tolerability and therapeutic efficacy of paclitaxel in a human ovarian cancer xenograft model. *Cancer Chemother. Pharmacol.* **2007,** *60* (6), 907-914.

124. McCann, C. K.; Growdon, W. B.; Kulkarni-Datar, K.; Curley, M. D.; Friel, A. M.; Proctor, J. L.; Sheikh, H.; Deyneko, I.; Ferguson, J. A.; Vathipadiekal, V.; Birrer, M. J.; Borger, D. R.; Mohapatra, G.; Zukerberg, L. R.; Foster, R.; Macdougall, J. R.; Rueda, B. R., Inhibition of Hedgehog signaling antagonizes serous ovarian cancer growth in a primary xenograft model. *PLoS One* **2011,** *6* (11), e28077.

125. Terwogt, J. M.; Nuijen, B.; Huinink, W. W.; Beijnen, J. H., Alternative formulations of paclitaxel. *Cancer. Treat. Rev.* **1997,** *23* (2), 87-95.

126. Berns, E. M.; Bowtell, D. D., The changing view of high-grade serous ovarian cancer. *Cancer Res.* **2012,** *72* (11), 2701-2704.

127. Lalwani, N.; Prasad, S. R.; Vikram, R.; Shanbhogue, A. K.; Huettner, P. C.; Fasih, N., Histologic, molecular, and cytogenetic features of ovarian cancers: implications for diagnosis and treatment. *Radiographics* **2011,** *31* (3), 625-646.

128. Sodek, K. L.; Ringuette, M. J.; Brown, T. J., Compact spheroid formation by ovarian cancer cells is associated with contractile behavior and an invasive phenotype. *Int. J. Cancer* **2009,** *124* (9), 2060-2070.

129. Shaw, T. J.; Senterman, M. K.; Dawson, K.; Crane, C. A.; Vanderhyden, B. C., Characterization of intraperitoneal, orthotopic, and metastatic xenograft models of human ovarian cancer. *Mol. Ther.* **2004,** *10* (6), 1032-1042.

130. Schorge, J. O.; McCann, C.; Del Carmen, M. G., Surgical debulking of ovarian cancer: what difference does it make? *Rev. Obstet. Gynecol.* **2010,** *3* (3), 111-117.

131. Kim, A.; Ueda, Y.; Naka, T.; Enomoto, T., Therapeutic strategies in epithelial ovarian cancer. *J. Exp. Clin. Cancer Res.* **2012,** *31*, 14.

132. Sugarbaker, P. H., Management of peritoneal-surface malignancy: the surgeon's role. *Langenbeck Arch. Surg.* **1999,** *384* (6), 576-587.

133. Keereweer, S.; Kerrebijn, J. D.; van Driel, P. B.; Xie, B.; Kaijzel, E. L.; Snoeks, T. J.; Que, I.; Hutteman, M.; van der Vorst, J. R.; Mieog, J. S.; Vahrmeijer, A. L.; van de Velde, C. J.; Baatenburg de Jong, R. J.; Lowik, C. W., Optical image-guided surgery--where do we stand? *Mol. Imaging Biol.* **2011,** *13* (2), 199-207.

134. Hirche, C.; Engel, H.; Kolios, L.; Cognie, J.; Hunerbein, M.; Lehnhardt, M.; Kremer, T., An Experimental Study to Evaluate the Fluobeam 800 Imaging System for fluorescence-guided lymphatic imaging and sentinel node biopsy. *Surg. Innov.* **2012**, doi: 10.1177/1553350612468962

135. Janib, S. M.; Moses, A. S.; MacKay, J. A., Imaging and drug delivery using theranostic nanoparticles. *Adv. Drug Deliv. Rev.* **2010,** *62* (11), 1052-1063.

136. Kumar, R.; Roy, I.; Hulchanskyy, T. Y.; Goswami, L. N.; Bonoiu, A. C.; Bergey, E. J.; Tramposch, K. M.; Maitra, A.; Prasad, P. N., Covalently dye-linked, surface-controlled,

and bioconjugated organically modified silica nanoparticles as targeted probes for optical imaging. *Acs Nano* **2008,** *2* (3), 449-456.

137. Yokoyama, M., Polymeric micelles as a new drug carrier system and their required considerations for clinical trials. *Expert Opin. Drug Deliv.* **2010,** *7* (2), 145-158.

138. Lee, S.; Choi, K. Y.; Chung, H.; Ryu, J. H.; Lee, A.; Koo, H.; Youn, I. C.; Park, J. H.; Kim, I. S.; Kim, S. Y.; Chen, X.; Jeong, S. Y.; Kwon, I. C.; Kim, K.; Choi, K., Real time, high resolution video imaging of apoptosis in single cells with a polymeric nanoprobe. *Bioconjugate Chem.* **2011,** *22* (2), 125-131.

139. Bae, Y. H., Apoptosis-targeted drug delivery. *J. Control Release* **2011,** *154* (3), 213.

140. Schutters, K.; Reutelingsperger, C., Phosphatidylserine targeting for diagnosis and treatment of human diseases. *Apoptosis* **2010,** *15* (9), 1072-1082.

141. Cho, H.; Lai, T. C.; Kwon, G. S., Poly(ethylene glycol)-*block*-poly(epsilon-caprolactone) micelles for combination drug delivery: evaluation of paclitaxel, cyclopamine and gossypol in intraperitoneal xenograft models of ovarian cancer. *J. Control Release* **2012,** *166* (1), 1-9.

142. Xiong, X. B.; Mahmud, A.; Uludag, H.; Lavasanifar, A., Conjugation of arginine-glycine-aspartic acid peptides to poly(ethylene oxide)-*b*-poly(epsilon-caprolactone) micelles for enhanced intracellular drug delivery to metastatic tumor cells. *Biomacromolecules* **2007,** *8* (3), 874-884.

143. Kapty, J.; Banman, S.; Goping, I. S.; Mercer, J. R., Evaluation of phosphatidylserine-binding peptides targeting apoptotic cells. *J. Biomol. Screen.* **2012,** *17* (10), 1293-1301.

144. Jin, Z. H.; Josserand, V.; Razkin, J.; Garanger, E.; Boturyn, D.; Favrot, M. C.; Dumy, P.; Coll, J. L., Noninvasive optical imaging of ovarian metastases using Cy5-labeled RAFT-c(-RGDfK-)4. *Mol. Imaging* **2006,** *5* (3), 188-197.

145. Park, K.; Kim, J. H.; Nam, Y. S.; Lee, S.; Nam, H. Y.; Kim, K.; Park, J. H.; Kim, I. S.; Choi, K.; Kim, S. Y.; Kwon, I. C., Effect of polymer molecular weight on the tumor targeting characteristics of self-assembled glycol chitosan nanoparticles. *J. Control Release* **2007,** *122* (3), 305-314.

146. Miyai, K.; Yamamoto, S.; Aida, S.; Shimazaki, H.; Takano, M.; Kudoh, K.; Furuya, K.; Tamai, S.; Matsubara, O., Massive intra-abdominal undifferentiated carcinoma derived from an endometrioid adenocarcinoma in a "normal-sized" ovary. *Int. J. Gynecol. Pathol.* **2010,** *29* (4), 321-327.

147. Zola, P.; Ferrero, A., Is carboplatin-paclitaxel combination the standard treatment of elderly ovarian cancer patients? *Ann. Oncol.* **2007,** *18* (2), 213-214.

148. Vaughan, S.; Coward, J. I.; Bast, R. C.; Berchuck, A.; Berek, J. S.; Brenton, J. D.; Coukos, G.; Crum, C. C.; Drapkin, R.; Etemadmoghadam, D.; Friedlander, M.; Gabra, H.; Kaye, S. B.; Lord, C. J.; Lengyel, E.; Levine, D. A.; McNeish, I. A.; Menon, U.; Mills, G. B.; Nephew, K. P.; Oza, A. M.; Sood, A. K.; Stronach, E. A.; Walczak, H.; Bowtell, D. D.; Balkwill, F. R., Rethinking ovarian cancer: recommendations for improving outcomes. *Nat. Rev. Cancer* **2011,** *11* (10), 719-725.

149. Soslow, R. A., Histologic subtypes of ovarian carcinoma: An overview. *Int. J. Gynecol. Pathol.* **2008,** *27* (2), 161-174.

150. Morrison, J.; Haldar, K.; Kehoe, S.; Lawrie, T. A., Chemotherapy *versus* surgery for initial treatment in advanced ovarian epithelial cancer. *Cochrane. Db. Syst. Rev.* **2012,** *15* (8), CD005343, doi: 10.1002/14651858.CD005343.pub3.

151. Salvesen, H. B.; Werner, H. M.; Krakstad, C., PI3K pathway in gynecologic malignancies. *Am. Soc. Clin. Oncol. Edu. Book* **2013**, 218-221.

152. Trivedi, R.; Kompella, U. B., Nanomicellar formulations for sustained drug delivery: strategies and underlying principles. *Nanomedicine* **2010,** *5* (3), 485-505.

153. Li, Y.; Xiao, K.; Luo, J.; Xiao, W.; Lee, J. S.; Gonik, A. M.; Kato, J.; Dong, T. A.; Lam, K. S., Well-defined, reversible disulfide cross-linked micelles for on-demand paclitaxel delivery. *Biomaterials* **2011,** *32* (27), 6633-6645.

154. Kalli, K. R.; Oberg, A. L.; Keeney, G. L.; Christianson, T. J. H.; Low, P. S.; Knutson, K. L.; Hartmann, L. C., Folate receptor alpha as a tumor target in epithelial ovarian cancer. *Gynecol. Oncol.* **2008,** *108* (3), 619-626.

155. Zeineldin, R.; Muller, C. Y.; Stack, M. S.; Hudson, L. G., Targeting the EGF receptor for ovarian cancer therapy. *J. Oncol.* **2010,** *2010*, 414676.